Computational and Mathematical Methods in Medicine

Mathematical Modeling of Patient Care

Guest Editors: Philip Crooke, John Hotchkiss, Yongwimon Lenbury, and Brett McKinney

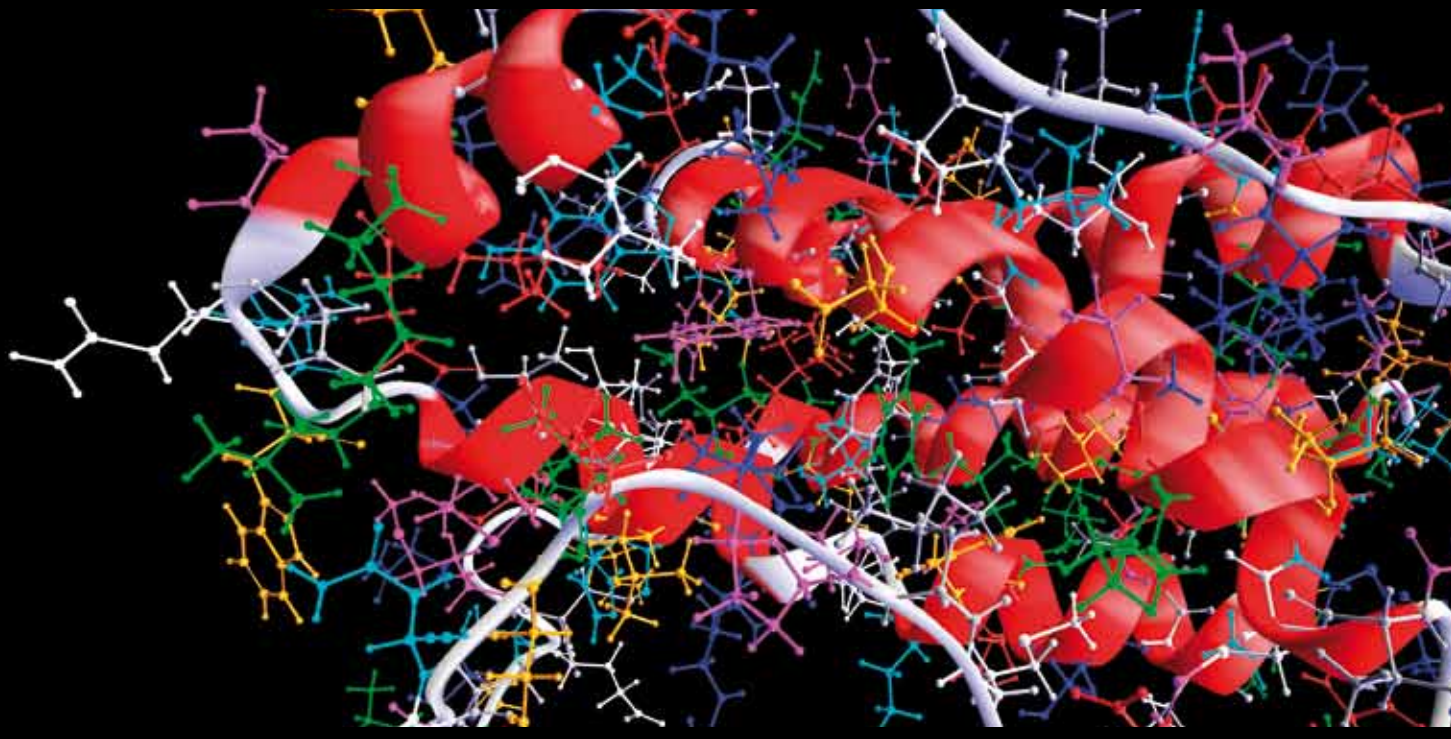

Mathematical Modeling of Patient Care

Computational and Mathematical Methods in Medicine

Mathematical Modeling of Patient Care

Guest Editors: Philip Crooke, John Hotchkiss,
Yongwimon Lenbury, and Brett McKinney

Editorial Board

Contents

Hindawi Publishing Corporation
Computational and Mathematical Methods in Medicine
Volume 2012, Article ID 563287, 2 pages
doi:10.1155/2012/563287

Editorial

Mathematical Modeling of Patient Care

Philip Crooke,[1] John Hotchkiss,[2] Yongwimon Lenbury,[3] and Brett McKinney[4]

[1] *Department of Mathematics, Vanderbilt University, Nashville, TN, USA*
[2] *Department of Critical Care Medicine and Department of Medicine, Pittsburgh Veterans Affairs Healthcare System, University of Pittsburgh Medical Center, Pittsburgh, PA, USA*
[3] *Department of Mathematics, Faculty of Science, Centre of Excellence in Mathematics (CHE), Mahidol University, Bangkok 10400, Thailand*
[4] *Tandy School of Computer Science and Department of Mathematics, Rayzor Hall, University of Tulsa, Tulsa, OK 74104, USA*

Correspondence should be addressed to Philip Crooke, philip.s.crooke@vanderbilt.edu

Received 28 March 2012; Accepted 28 March 2012

In our call for papers for this special issue, we requested topics that ranged from mathematical models of physiological systems to macroeconomic models of the healthcare industry. Although the response to this broad invitation was muted, we did receive a nice cross-section of papers within this spectrum of topics. In the following, we summarize the six papers included in this volume.

D. T. Grima et al. investigated the impact of antibiotics on treating *Clostridium difficile*-associated diseases (CDAD) on the emergence of antibiotic-resistant bacteria using mathematical model describing the impact of in-hospital antibiotic use. The model is a system of nonlinear differential equations arising from a compartment network of uncolonized and colonized patients with and without antibiotic treatment. The model leads to a very important conclusion: there may be a substantial reduction in antibiotic-resistant prevalence when nonantibiotic strategies are employed for CDAD. This is a perfect example of how mathematical modeling can lead to a practical change in treatment and impact on patient health and a reduction in costs.

Advances in mathematical modeling have led to various effective tools for early diagnosis, such as the application of thermometry ultrasonic techniques. Before implementation of the ultrasonic noninvasive estimation of thermal gradients into tissues based on spectral changes, rigorous analyses, over transient echotraces acquired from well-controlled biological and computational phantoms, must be still made in order to improve resolutions and evaluate clinic limitations. I. Bazan et al. applied this technique to computationally modeled echotraces from scattered biological phantoms, attaining high resolution (better than 0.1°C). They also provided computer methods for viability evaluation of thermal estimation from echoes with distinct noise levels, making it difficult to interpret the readings. As a result of their analyses, the technique has been evaluated as a possible effective diagnosis tool for scattered tissues applications. Such research and analyses are of great importance since the ability to detect changes of thermal origin in ultrasonic echo spectra means the achievement of precise noninvasive temperature estimations that could be very useful as an early complementary indicator of infections, inflammations, or cancer.

Obstructive sleep apnea (OSA) is an important health issue and has been subject to different modeling investigations. C. T. Su et al. have applied a Mutliclass Mahalanobis-Taguchi System (MMTS) to the problem of prediagnosing the condition using readily available patient information. Their model results in a better than 84% accuracy. This statistical diagnostic/predictive method comes from pattern information technology and demonstrates an important application of a little used modeling paradigm in biology.

The paper by C. Pagel et al. addresses a problem of growing relevance with an aging population, dwindling resources, and a declining number of healthcare providers: that of optimal scheduling in the context of a stepped care. This topic is of considerable interest, not only in the domain addressed by the authors, but in other populations requiring complex, highly specialized care. The author's model includes stratified levels of intensity of care, and can be used to analyze expected changes in waiting times

and throughput under different allocations of scheduled slots. This quantitative model will be of highly operational interest—particularly to large, integrated healthcare systems confronted with a growing mental healthcare population. Moreover, since the model is sufficiently flexible, it may be adapted to address queuing systems germane to other highly complex medical conditions.

Healthcare providers and networks face more than resource limitations: increased oversight and an emphasis on the quality of care are wending their way toward reimbursement ("pay for performance") as well as public access to quality "report cards." In this context, establishing that the metrics of quality accurately reflect the performance of the hospital, rather than differences in patient populations, is of paramount importance. The paper by D. Shine directly addresses this issue, focusing on the modulation of risk by comorbid conditions. Shine illustrates a spreadsheet-based approach for capturing high impact comorbidities and identifies those having the greatest impact on risk. This general approach could improve the accuracy of expected mortality estimates, thus also the ratio of observed mortality to expected mortality. Such considerations will have a clear impact not only on quality reports but also eventually on equitable reimbursement.

HIV/AIDS is a global pandemic of disastrous proportions, in which the virus can rapidly develop resistance to antiretrovirals, and subsequently, lifelong therapy is required, and many at-risk individuals live in austere environments where compliance with complex treatment regimens may prove problematic. These medications are often toxic, and attenuation of treatment intensity due either to toxicity or to regimen complexity can promote the development of drug resistance. The development of new antiretroviral agents or formulations is both costly and critical in the setting of a virus prone to very rapid mutation. M. L. Branham et al. illustrate the use of artificial neural networks (ANN), primed with drug physicochemical and bioaccumulation characteristics, to predict maximum recommended therapeutic doses of antiretroviral agents. They note particular utility of the ANN approach when the medications evaluated are poorly soluble in water. This type of computational analyses should prove useful as drug developers balance bioavailability and ease of administration against tolerable doses, a balance with implications for compliance and the potential for effective treatment.

We are convinced of the utility of mathematics and other quantitative approaches to provide better healthcare. The six papers in this volume demonstrate that mathematical modeling can play a central role in patient care innovations.

Philip Crooke
John Hotchkiss
Yongwimon Lenbury
Brett McKinney

Hindawi Publishing Corporation
Computational and Mathematical Methods in Medicine
Volume 2012, Article ID 275405, 14 pages
doi:10.1155/2012/275405

Research Article

Possible Patient Early Diagnosis by Ultrasonic Noninvasive Estimation of Thermal Gradients into Tissues Based on Spectral Changes Modeling

I. Bazan,[1] A. Ramos,[2] H. Calas,[2] A. Ramirez,[1] R. Pintle,[1] T. E. Gomez,[2] C. Negreira,[3] F. J. Gallegos,[1] and A. J. Rosales[1]

[1] *ESIME (Sede-Zacatenco) Instituto Politécnico Nacional (IPN), Avenida Instituto Politécnico Nacional s/n, México City, 07738 DF, Mexico*
[2] *Ultrasonic Signals, Systems and Technologies Laboratory, CSIC, Serrano 144, 28006 Madrid, Spain*
[3] *Departamento de Materiales, Facultad de Ciencias, Universidad de la Republica, Montevideo 14200, Uruguay*

Correspondence should be addressed to A. Ramos, aramos@ia.cetef.csic.es

Received 15 December 2011; Accepted 20 February 2012

Academic Editor: Yongwimon Lenbury

To achieve a precise noninvasive temperature estimation, inside patient tissues, would open promising research fields, because its clinic results would provide early-diagnosis tools. In fact, detecting changes of thermal origin in ultrasonic echo spectra could be useful as an early complementary indicator of infections, inflammations, or cancer. But the effective clinic applications to diagnosis of thermometry ultrasonic techniques, proposed previously, require additional research. Before their implementations with ultrasonic probes and real-time electronic and processing systems, rigorous analyses must be still made over transient echotraces acquired from well-controlled biological and computational phantoms, to improve resolutions and evaluate clinic limitations. It must be based on computing improved signal-processing algorithms emulating tissues responses. Some related parameters in echo-traces reflected by semiregular scattering tissues must be carefully quantified to get a precise processing protocols definition. In this paper, approaches for non-invasive spectral ultrasonic detection are analyzed. Extensions of author's innovations for ultrasonic thermometry are shown and applied to computationally modeled echotraces from scattered biological phantoms, attaining high resolution (better than 0.1°C). Computer methods are provided for viability evaluation of thermal estimation from echoes with distinct noise levels, difficult to be interpreted, and its effectiveness is evaluated as possible diagnosis tool in scattered tissues like liver.

1. Introduction

Some broadband ultrasonic technologies are being explored to make possible their utilization as a noninvasive method for diagnosis of certain human diseases [1–12]. These researches are focused in deep analyses based on intelligent processing of bioultrasonic signals acquired from the interrogated medium (a biological phantom, a zone of a superficial muscular tissue, or a located and deep region of an internal organ). Certain advanced signal processing techniques seem to be efficient tools for extraction of useful information about the media under study, in order to (a) support the diagnosis of some viral or degenerative diseases [4–9]; (b) make a noninvasive estimation of thermal distribution maps in patient tissues under hyperthermia treatments [2, 3, 10–13]; (c) or even to obtain advances for detecting, in the future, some types of tumors, based on an extension of the tool mentioned in (b), and improving its spatial resolution.

Parameters to be analyzed, with these purposes, should be some changes that can be detected between normal transient multipulse ultrasonic traces registered by echointerrogation from a healthy tissue, and those acquired from tissues with some pathology. As an example, the variation on ultrasonic arrival times and speed or on amplitude and phase of the echo-traces spectra, due to changes of stiffness or of internal sizes or distances between scatters, in hepatic

tissue, could be a potential indicator of chronic hepatitis. Along many years, deep researches were performed to create and improve specific procedures for extraction of data of interest inside tissues, by detecting morphologic alterations in the returning ultrasonic echo-signals. Such is the case of the spectral analysis applied more recently to study some kinds of multiecho broadband signals [10, 13], in order to extract useful clinic information hidden inside them, by performing an accurate estimation, in frequency domain, and determining its efficiency as potential thermometry technique. And in the general context of the early diagnosis in patient organs, the combination of these thermometric techniques with emergent methods for ultrasonic measure of tissue elastography should be an interesting option.

Typical ultrasonic echo-signals acquired from biological media are broad-band pulses whose nature depends on the internal biological structure and other physical parameters. In fact, the resulting ultrasonic patterns are mainly related to the great quantity of interactions between the emitted ultrasonic pulse and the dispersive structure of many tissues, in particular in liver. For this reason, the complete patterns of the raw ultrasonic echoes are rather complex in both time and frequency domains, and the multifactorial information that they contain is difficult to be directly interpreted. Certain authors have explained the complex nature of these echoes using a mathematical model consisting of structures regularly spaced among them [14, 15], or formed by a group of scatters randomly distributed. Others proposals try to model it as a random scatters distribution with certain statistic regularity, which appears to explain in a more realistic way the nature of real signals acquired from tissues with semiregular structure [16, 17].

A processing tool having to extract useful spectral information from a ultrasonic signal will be in front of, at least, two difficult problems: (i) the analysis of a complex nature signal, with parameters of nondeterminist type and continuously changing with medium conditions and (ii) the discernment among factors providing a useful information and those that just act as undesirable perturbations, masking the information to be extracted. Thus, the computer evaluation in laboratory, of the reliability and robustness of any spectral processing tool for this aim, is a crucial aspect for future uses of such tool in medical diagnosis, before applying it to detect changes in real tissues.

Some laboratory studies [10, 15] show that methods based on frequency domain analyses of echoes acquired from tissues and biological phantoms seem to be a reliable option to extract information about pathologic changes on some relevant anatomical and physiological parameters, like temperature, which usually results in being directly related with location alterations in certain peak values appearing into the echoes spectra.

Preliminary analysis procedures [13] have been already proposed to evaluate with accuracy, in laboratory conditions, the advantages and disadvantages of this type of ultrasonic tools for thermal estimation at the internal parts of biological phantoms designed "ad hoc" with internal embedded scattering structure; the laboratory frame permits to precisely control the main phantom parameters, to properly emulate typical acoustic responses of different patient tissues. So, in those procedures, the performance offered by distinct processing tools (in frequency, time, and phase domains) was compared to assess their applicability and linearity and also to show their limitations in the hyperthermia range [18]. Algorithms robustness, computational charge using a standard numerical tool, and thermal and spatial resolutions, were used in those procedures as useful and convenient evaluation indexes.

In particular, the spectral analysis of ultrasonic echoes was studied to achieve thermal estimation by evaluating the behavior of frequency peaks related with certain spatial regularity and uniformity level of acoustic scatters in determined phantom or tissues structures. A change in the medium physical stage can produce a variation in its ultrasonic characteristics (ultrasound velocity, flight time or echoes concentration), with associated alterations in the frequency spectrum of the whole acquired echo signal, due to advancement, time concentration or expansion proportional to the physical magnitude to be sensed. The spectral changes, mainly in location of some frequency peaks, can be carefully analyzed and related to alterations happened in tissue pathology. Applications of this could be the estimation of specific changes on tissue parameters having a direct clinic signification as temperature, density, blood irrigation, or inflammation.

But there are still pendent some modeling aspects that have to be studied and solved by computer simulation and evaluations in laboratory conditions of the ultrasonic echo-responses, before achieving a reliable application of the spectral analysis and possible extensions to distinct echographic areas, as a support and estimation tool for advanced medical diagnosis. To attain this difficult aim depends on improving aspects of the own spectral ultrasonic estimation procedure and, maybe, that also combines it with other noninvasive ultrasonic measuring techniques [2, 3].

In this paper, a systematic analysis is made on the effectiveness of results achievable by applying classical and new high-resolution spectral ultrasonic techniques, to computed echo-traces (multiechoes with different levels of noise and time variance), for evaluating those as future medical diagnosis tools for thermal estimation, in scattered media like the liver. The occurrence of a convenient quasi-linear dependence between the unitary average increments in the location of some frequency spectra peaks and the temperature rising in the tissue phantoms is first analyzed for computer-simulated A-scan registers, obtained from echo modeling, and whose parameters are under a precise control. A basic average increment (per °C and mm) is identified in this spectral technique: 3 KHz/°C. So, samples of typical ultrasonic multiechoes are generated by computation of signal models, trying to exemplify very diverse characteristics, adverse or not, of the rather variable in time echo-traces acquired from the real tissues.

By applying new ultrasound spectral analysis methods that incorporate resolution improvements, some interaction effects of the ultrasonic echoes with thermally or mechanically modified propagation media are accurately detected. Finally, the validity limits of those methods, under different

signal-to-noise levels and interechoes time variances in the ultrasonic signal traces, are carefully evaluated.

These objectives will be attained in three phases: (i) analyzing current models and spectral techniques for noninvasive thermal estimation inside tissues by detection of frequency changes in ultrasonic echoes, (ii) providing a well-based study of the most important aspects to be considered on the effectiveness of an improved spectral analysis option (proposed here to increase the thermal resolution), as a possible tool for accurate medical diagnosis; aspects like resolutions, accuracy, noise robustness will be studied, (iii) and some circumstances that can be seen as possible functional gaps are identified, and a solid fundament to know how these aspects can be overcome will be provided.

2. Models and Methods

2.1. On Computer Modeling of Thermally Induced Alteration in Multiscattering Echoes from Patient Tissues. To properly apply, for patient diagnosis purposes, the detection and quantification of certain particular changes observed in echographic information, induced by changing temperatures, it becomes necessary to previously make careful analyses of how this really occurs in time and spatial domains, for different tissue structures and ranges.

Ultrasonic echo-signals collected from patient tissues can be considered as a complex superposition of several single echoes, generated by the interaction among an emitted ultrasonic pulse and its multiple acoustic reflections by the typical dispersive structure into the biological tissues under analysis. This internal structure can be associated to blood vessels, cells groups, membrane-type internal structures, or any spatial configuration of the patient organs located in the ultrasonic path, inducing acoustic diffraction or dispersion on the propagating ultrasonic pulses.

Depending on the type of organ, the pattern of the ultrasonic echo-signals changes: some kinds of organs have a quasihomogeneous tissue composition presenting a semiregularly spaced structure of scatters, for example, the liver or the fat; others have an anatomical structure composed by cavities, muscular tissue, or parenchyma, which makes it (from an ultrasonic point of view) a totally irregular reflection structure, as it happens with the heart or, in minor degree, with the lung.

In the laboratory practice devoted to create new designs of diagnostic instruments, the related ultrasonic studies and researches use to be made firstly in distinct biological phantoms with internal artificial reflectors trying to approximate the distinct tissues, in that related to emulate the echographic ultrasonic responses.

But, previously to the construction of an adequate set of biological phantoms with the mentioned tissue emulation purposes, it would be of big interest and usefulness to be capable of making approximated predictions of acoustical responses when an ultrasonic high-frequency pulse is applied over their external surfaces, and also (in the context of this paper) of how these responses, from several tissue points, are being modified for distinct temperatures. This aim needs to create useful and relatively simple echographic mathematical models, and the subsequent simulation algorithms for calculating with certain accuracy the echoes, thermal modification by computational means.

In conjunction with the mentioned tools for echoes calculation, it is also necessary to find some procedure involving a reasonable complexity in order to obtain an easy interpretation and precise analysis of light variations (from the nonpathologic case) on complex echographic patterns, mainly for the case of tissues having a high level of internal scattering into their structure (as those considered in this paper).

A further requirement, in this context, is to provide means for analyzing, in comparative terms, the temperature estimated in several points located very close in a same patient organ, because some pathologies, as certain cancer affections, present their early symptoms precisely with very small thermal differences (tenths of °C) appearing among surrounding tissue places, due to light local alterations on the blood perfusion by neovascularization. For this reason, a precise and noninvasive analysis of small thermal gradients into tissues becomes of a big interest for possible future early detection of certain diseases. And for investigating the potential performance in thermal and spatial resolutions of the HR spectral analysis of ultrasonic scattering echoes, the creations of basic computer modeling tools become very convenient and useful.

2.2. A Deterministic Mathematical Model for Ultrasonic Echoes from a Uniform Scattering Structure. A simple model proposed to emulate an ultrasonic signal from patient organs supposes that some types of its biologic tissues can be considered, from an acoustic point of view, as a semiregular matrix of scatters separated by an average distance "d." When an ultrasonic pulse travels and is being reflected through a path inside a tissue (i.e., from its internal structure), the resulting echo-graphic signal trace, $s(t)$, is a complex sum of the echoes from scatters (reflectors) that the pulse finds in its pathway [19], and each simple pulsed echo has a different time of flight, depending on the distance that this ultrasonic pulsed signal has traveled from a particular reflector:

$$s(t) = \sum_{m=1}^{n} e_m \gamma_m \left(t - \left(\frac{2d_m}{v} \right) \right), \tag{1}$$

where e_m is the echo amplitude due to the mth reflector, $\gamma_m(\cdot)$ is the shape of the unitary individual echo due to the mth reflector, t is time, d_m is the module of the position vector of the mth reflector, and v is the ultrasonic speed.

In general, it is supposed that the analyzed tissue is located at the far-field zone of the emitting ultrasonic face, where diffraction effects (from the aperture) are negligible, and no important dispersion or attenuation effects are considered. Under these conditions, each echo produced by a punctual reflector would preserve the form of the original pulse emitted by the transducer face to the propagation medium. These rather restrictive considerations can be assumed in our analysis, due to our specific objective is here only related to the estimation of changes in the frequency

peaks locations related to physical alterations in an internal tissue parameter with relevant diagnostic significance, as a displacement in those peak locations due to a local temperature rise in a specific tissue zone, and isolating possible interferences originated from other possible aspects being present (dispersion in frequency or other characteristics affecting reflected waveforms).

For the conditions imposed by this approach [17], the emitted unitary pulse can be mathematically modeled as

$$P(t) = -te^{-4\omega^2 t^2} \sin(2\pi f_0 t), \quad t > 0, \tag{2}$$

where ω is the ultrasonic bandwidth and f_0 is the transducer central frequency.

The individual echo waveform, produced by the interaction of the emitted pulse $P(t)$ with one reflector, can be considered under the approximation of our approach, as a replica to the emitted unitary pulse, regarding its time-shape; then $\gamma(t) = P(t)$.

An example of multiecho signal centered in 2,25 MHz with a bandwidth ($\omega = 1$ MHz), generated by a computational algorithm based on this model, is shown in Figure 1(a).

As a more realistic reference, a signal with around 2,25 MHz of central frequency, acquired from an experimental phantom (based on agar and tridistilled water), is shown in Figure 1(b); four layers of glass microspheres were embedded in the central axis of the biologic phantom, to simulate a quasiregular scatters distribution. Here, the interarrival time between echoes is not constant and some echoes appear to be superimposed.

2.3. Mathematical Modeling of Statistical Type for a Nonuniform Multiecho Trace. The model explained above is considered in the literature as a basic bioultrasonic signal pattern for numerical simulation of the echotraces resulting from ultrasound interaction with biological tissue. Nevertheless, there are more complex approaches to mathematically describe the nature of the bioultrasonic signals, more properly.

In real patient tissues, in spite of the semiuniform distribution of scatters in some kind of organs, the irregular behavior still increases a little respect to the last figure, as can be seen in Figure 2(a), for an ultrasonic trace acquired from a sample of pig liver, by using ultrasonic irradiation with a 2 MHz broadband transducer.

And, in Figure 2(b), a 5 MHz echo-trace from a computational phantom is shown.

A model describing this type of traces from biological tissues uses a random distribution of scatters with a certain degree of statistical regularity [16]. The same acoustic conditions for the interaction with each single reflector, as those considered in Section 2.2, are maintained in this model: no important dispersion or diffraction, punctual reflectors, and far field conditions. Thus, individual echo, $\gamma(t)$, preserves the form of the original emitted pulse, $P(t)$. But, now, the internal scatters distribution is modeled with a statistical model that approximates the echo-nature produced by a specific kind of tissue. In this case, the resulting multiecho signal, $s(t)$, can be expressed as

$$s(t) = \sum_{m=1}^{n} A_m \gamma_m (t - t_m), \tag{3}$$

where t_m is the random receiving time delay of the mth echo that, in this case, does not depend on a regular distance d; the amplitude Am of $\gamma(\cdot)$ is considered as a random variable, and $s(t)$ is the random model that depends on the random variables Am and $\tau_m = t_m - t_{m-1}$ (the inter-arrival time between echoes from consecutive scatters).

And we obtain the mathematical expectation over $s(t)$

$$E[s(t)] = \sum_{m=1}^{n} E\left[A_m \gamma_m (t - t_m)\right] = \overline{\gamma}(t) \otimes \sum_{m=1}^{n} A_m \delta(t - t_m), \tag{4}$$

where $E[\cdot]$ is the expected value over waveforms $[s_m(t)]$, $\overline{\gamma}(t)$ is the common pattern assumed for all the unitary individual echo functions, and $\otimes$ represents the time convolution operator.

In consequence, the multiecho signals acquired from biological tissues, could be modeled as a convolution between the individual echo function $\overline{\gamma}(t)$ and the sum of the impulse sampling functions $\delta(t - t_m)$ governed by a random time variable (τ_m).

When the tissue has a regular structure, then the interarrival time standard deviation is small compared with the mean value, whereas if the tissue has an irregular composition, then the standard division will attain a high value.

In the following sections of this work, a gamma distribution is used to approximate the statistical behavior of the interaction of the tissue structure with the ultrasonic travelling pulses. All the models considered here were applied in computational simulation, considering a monodimensional path. See waveform of Figure 3 as an example.

2.4. Modeling the Behavior of Scattered Ultrasonic Echoes under Temperature Variations, and Detection Method of Their Effects on the Frequency Spectra. The presence of a number of pulsed ultrasonic echo-signals created by scattering in inspected biological media, which have certain uniformity in the spatial distribution of their scatters, offers the opportunity to exploit spectral analysis advantages, allowing the detection of well-defined frequency peaks associated with the spatial repetition rate of the tissue internal structures. Spectral analysis techniques can be applied to semiregular composition tissues and some relatively heterogeneous structures, to find peaks shifts related to clinical parameters, for example: temperature increments, inflammation, or edema.

In the following, a classical technique for spectral analysis on biological media is resumed, and an improved procedure, proposed by the paper's authors, is described. This resolves the current problem arising in some applications where high resolution is required for frequency peak shift detection (for instance, when it is necessary to achieve a thermal resolution of 0,1°C in several inner parts of a tissue).

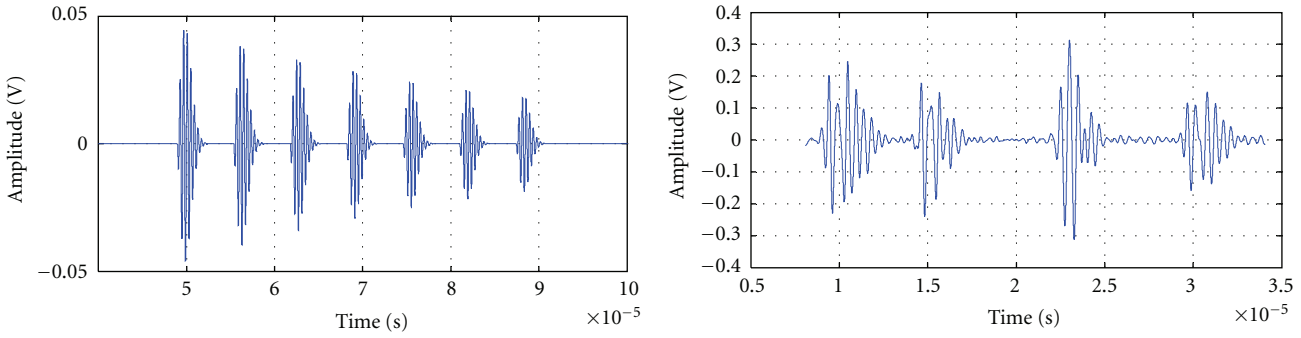

Figure 1: (a) Simple simulated multiecho signal based on the mathematical model of regularly spaced scatters, for the case of clearly separated echoes. (b) Acquired echosignal from an experimental phantom with 4 layers of glass microspheres. An ultrasonic transducer with frequency $f_0 = 2,25$ MHz was used.

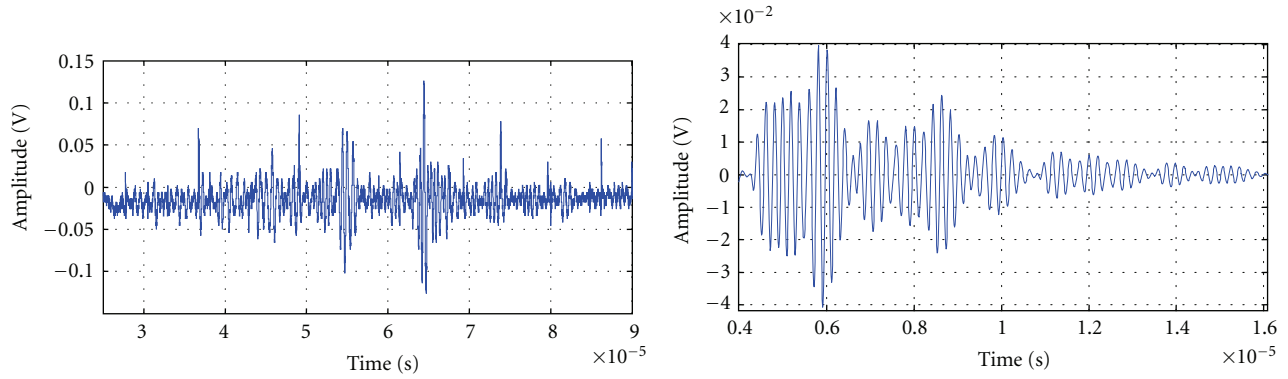

Figure 2: (a) Ultrasonic trace acquired from liver of pig using a 2 MHz transducer. (b) A quite realistic 5 MHz echo-trace from a computational phantom.

2.4.1. Classical Thermal Estimation Techniques for Precise Spectral Analysis of Echoes. Spectral analysis techniques have been applied to ultrasonic signals in order to know frequency peaks changes in the echoes and to relate them with the thermal changes originating those. The more precise of them [10] was carried out using the power spectrum density (PSD) obtained by an autoregressive (AR) model [20–22], to find, in a noninvasive manner, temperature changes in biological phantoms or tissues. And, after it, some optimizations were proposed to improve the thermal resolution and application protocols [18]; in addition, specific quality indexes were established to comparatively evaluate the distinct ultrasonic methods proposed for thermal estimation [13].

In this subsection, it is mathematically shown the linear relation existent between the changes thermally induced on the fundamental frequency related to a semiregular scattering structure into biological tissues and the related temperature variations.

The theoretical fundamentals on which this analysis is based on are as follows.

(a) The tissue, from an ultrasonic point of view, can be seen as a lattice of scatters semiregularly spaced among them by an average distance "d".

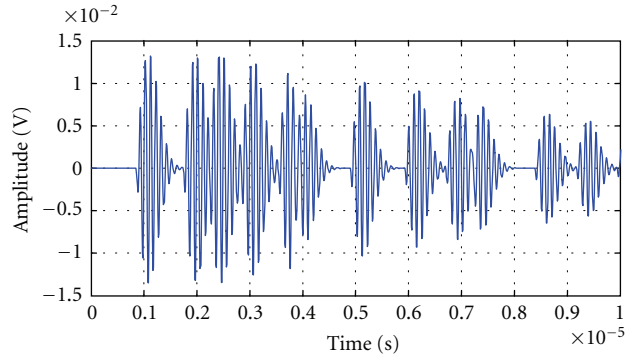

Figure 3: Multiecho signal simulated from a model for a random scatters distribution.

(b) "d" varies proportionally with the temperature changes, and its increments are determined by the coefficient of thermal expansion:

$$d(T) = d_0(1 + \alpha\Delta T), \tag{5}$$

where d_0 is the initial average distance between scatters, α is the linear coefficient of thermal expansion, and ΔT is the temperature variation.

(c) The speed of sound proportionally changes with the temperature.

In these conditions, the average inter-arrival time between the echoes received, by an ultrasonic transducer with proper bandwidth, is associated to a fundamental resonance frequency (and its harmonics) depending on d and speed of sound, v, in this way:

$$f_x = \frac{xv(T)}{2d(T)}, \tag{6}$$

where f_x is the xth harmonic frequency, $x = 1$ represents the fundamental frequency, and T is the temperature. Therefore, changes in f_1 and its harmonics (overtones) are proportional to thermal changes, as is detailed in the following expression:

$$\Delta f_x(T) = \frac{x}{2d_0}\left[\frac{dv(T)}{(dT)}\bigg|_{T=T_0} - \alpha v_0\right]\Delta T. \tag{7}$$

In (7), Δf is the frequency shift, x the harmonic number, $dv(T)/d(T)$ the relative change in the sound speed with temperature, and v_0 the sound speed in the tissue at the base temperature T_0 [10].

In order to obtain a reasonable frequency resolution in the PSD distribution, a calculation using a parametric method is performed, which supposes that the analyzed signal (data sequence $s(n)$) is the result of filtering a white noise of average power similar to the unit [20–22]. Suppose the well-known filter function ¥(z):

$$¥(z) = \frac{B(z)}{A(z)} = \frac{\sum_{i=0}^{q} z^{-i} b_i}{1 + \sum_{i=1}^{p} z^{-i} a_i}, \tag{8}$$

then, a good resolution PSD of the signal is given by

$$§_{xx}(f) = |¥(f)|^2 §_{ww}(f) = \sigma_w^2 \frac{|B(f)|^2}{|A(f)|^2}, \tag{9}$$

where $§_{xx}(f)$ is the high resolution PSD of the signal, $§_{ww}(f)$ the PSD of the input sequence, ¥(f) the frequency response of the model, and σ_w^2 the white noise variance.

The random process $s(n)$ is the ultrasonic signal under analysis, generated by a model of poles and zeros called Autoregressive Moving Average when $q = 0$ and $b_0 = 1$:

$$¥(z) = \frac{1}{A(z)} \tag{10}$$

and its output, $s(n)$, is known as autoregressive (AR) process with order p.

In consequence, the PSD for an autoregressive process model is given by

$$§_{xx}(f)_{\mathrm{AR}} = \frac{\sigma_w^2}{|A(f)|^2}. \tag{11}$$

To obtain the model parameters, a_i, there are several algorithms that have been developed, one of the most known is the Yule Walker method based on the data autocorrelation estimation. A relation between the signal autocorrelation, £$_{xx}$, and these parameters can be calculated by means of the following equations [21]:

$$£_{xx}(n\mu) = \begin{cases} -\sum_{i=1}^{p} a_i £_{xx}(\mu m - i), & m > 0, \\ -\sum_{i=1}^{p} a_i £_{xx}(\mu m - k) + \sigma_w^2, & m = 0, \\ £_{xx}^*(-m\mu), & m < 0. \end{cases} \tag{12}$$

2.4.2. Improved Procedure Proposed for HR Spectral Estimation of Small Thermal Changes. The main limitation of the above-described temperature estimation technique, based on advanced spectral analysis of ultrasonic echoes, is related to its maximum resolution achievable in the measure of the frequency peaks shifts, subsequently reducing the final resolution in the diagnosis parameter (i.e., in the resolution for thermal estimation, or evaluation of small tissue inflammations for early detection of infection pathologies); this limitation appears even for the more favorable parametric cases of the technique described in the last paragraph.

In order to overcome this limitative aspect for precise diagnosis by noninvasive thermal estimation [18], a new signal processing step is proposed by authors to be added to the analytical procedure, looking for the consecution of a higher frequency resolution, that with the basic spectral approach detailed in the previous subsection. Initial results from our improved procedure for processing the multiple power spectra involved in multipoint measures provide a better resolution than using previous ultrasonic estimation options. In addition, the Burg method is applied here as an alternative option to the classical approach for power spectrum estimation, giving a better final frequency resolution. In our estimation of the AR parameters by Burg method, a minimization of the direct and inverse errors of the linear predictors is made, with the restriction that AR parameters should satisfy the Levinson-Durbin recursion.

The estimations of the direct and inverse linear prediction are defined as

$$\begin{aligned} \hat{x}(n) &= -\sum_{k=1}^{m} a_m(k) x(n-k), \\ \hat{x}(n-m) &= -\sum_{k=1}^{m} a_m^*(k) x(n+k-m), \end{aligned} \tag{13}$$

where $a_m(k)$, $0 \le k \le m-1$, $m = 1, 2, \ldots, p$, are the prediction coefficients. And the corresponding direct and inverse errors, $f_m(n)$ and $g_m(n)$, are defined as

$$\begin{aligned} f_m(n) &= x(n) - \hat{x}(n), \\ g_m(n) &= x(n-m) - \hat{x}(n-m). \end{aligned} \tag{14}$$

The minimum square error is given by

$$\varepsilon_m = \sum_{n=m}^{N-1} \left[|f_m(n)|^2 + |g_m(n)|^2 \right]. \tag{15}$$

This error is minimized selecting the prediction coefficient according to the restriction to satisfy the Levinson-Durvin recursion given by

$$a_m(k) = a_{m-1}(k) + K_m a^*_{m-1}(m-k), \quad 1 \le k \le m-1,\ 1 \le m \le p, \tag{16}$$

where $K_m = a_m$ is the m reflection coefficient of the predictor lattice filter and can be expressed as

$$\hat{K}_m = \frac{-\sum_{n=m}^{N-1} f_{m-1}(n) g^*_{m-1}(n-1)}{(1/2)\left[\hat{E}^f_{m-1} + \hat{E}^b_{m-1}\right]}, \quad m = 1, 2, \ldots p. \tag{17}$$

$\hat{E}^f_{m-1}$ and $\hat{E}^b_{m-1}$ are an estimation of the total square error E_m.

The Burg algorithm computes reflection coefficients of the equivalent lattice structure and Levinson-Durvin algorithm is used to obtain AR model parameters. Based on estimation of AR parameters, the Power Spectrum can be estimated as

$$P^{\mathrm{BU}}_{xx}(f) = \frac{\hat{E}_p}{\left|1 + \sum_{k=1}^{p} \hat{a}_p(k) e^{-j2\pi f k}\right|^2}. \tag{18}$$

The main advantages of the Burg method to estimate AR model parameters are (a) higher frequency resolution, (b) stable AR model, and (c) better computation efficiency [21]. So, for the cases considered here with multiple short-data registers (needed when thermal gradients must be analysed, to obtain certain spatial discrimination in ultrasonic estimation), our improved method could achieve an excellent temperature resolution for distinct points separated a few millimetres; thermal resolutions even better than a tenth of °C can be obtained, if a high enough overtone order is selected for the shift analysis.

The high resolution (HR) thermal detection is completed by properly applying and adapting, to our estimation problem involving rather short-time windows, a procedure in certain way parallel to some techniques applied in other digital signal processing areas, by properly decomposing the echotraces in many sufficiently small fractional time-windows and artificially extending their digital lengths in all of them, before to be parametrically analyzed in the power spectrum domain with an improved frequency resolution. Each resulting time fringe is previously extended, before and after of the occurrence of each original acquired short echo-segment, with many null-value new samples in number enough to attain a total of Nf digital samples. So, the needed high resolution in the frequency domain can be attained for the subsequent power spectra calculated with Burg method from the extended digital registers associated to the successive time subtraces, instead the original registers with N_i samples, $Nf = xNi$.

The new processing proposed multiplies the frequency resolution of the PSD algorithm.

For implementing it, a number of new register vectors (FRV_j) are arranged by properly extending the original m registers generated by segmentation of the whole echo-trace acquired in the computational phantom or in the biological tissue, $s_j(n)$:

$$\mathrm{FRV}_j = \Big\{ 0_1, 0_2, \ldots, 0_{(x-1)Ni/2}; s_j(1),\ s_j(2),\ \ldots, s_j(Ni);\ 0'_1, 0'_2, \ldots, 0'_{(x-1)Ni/2} \Big\}, \quad (j = 1, 2, \ldots, m). \tag{19}$$

Preliminary results obtained with an improvement respect to other AR parametric method (but based on Yule-Walker equations), and focused to get a higher thermal resolution, are presented in [13], using the tenth harmonic of the fundamental resonance frequency associated to the medium scattering. This already represented an excellent resolution in temperature (0.12°C), for instance for the hyperthermia purposes intended in that work. These promising first results, for measuring tissue temperature into patient organs, were probed to have a convenient near-to-linear dependence with the frequency shifts observed in the acquired ultrasonic echo-signals.

In the current paper, these already good results are even further improved, by doing the above-described technique extension, introducing the Burg calculation in this context and getting smaller frequency sampling steps in the power spectrum density, making so possible to detect temperature changes with resolution as low as 0.08°C, for a number of distinct organ points located at neighboring places.

And in relation to the capability of this option related with the spatial resolution in thermal estimation purposes, a favorable first indication was obtained using this type of echo-trace processing, and properly choosing the length of the elemental fractional times of the multiple windows in which the whole echo-trace must be discomposed.

So, in Figures 4(a) and 4(b), it can be clearly seen that a reasonably good correlation, between the thermal relative increments in a number of points of the propagation media and certain frequency displacements observed, can be obtained, by analyzing (in this case) the shifts in the tenth harmonic of the resonance frequency related to the average separation among internal scatters into a tissue phantom. It confirms that it is possible to make an ultrasonic estimation of positive (a) and negative (b) arbitrary temperature gradients in biological media. Thermal gradients, shown as red curves in Figure 4, correspond to distributions along the central axis of a phantom during a laboratory heating procedure with a therapy ultrasound transducer and following the experimental protocol explained in [23].

These temperature gradients were introduced as input data for simulation of received echo-traces from two phantom zones of 12 mm each one, and then, a frequency analysis was performed over 20 time-windows of each echo-trace; so, frequency shifts of the tenth harmonic were evaluated in each window. The values of these shifts, with regard to

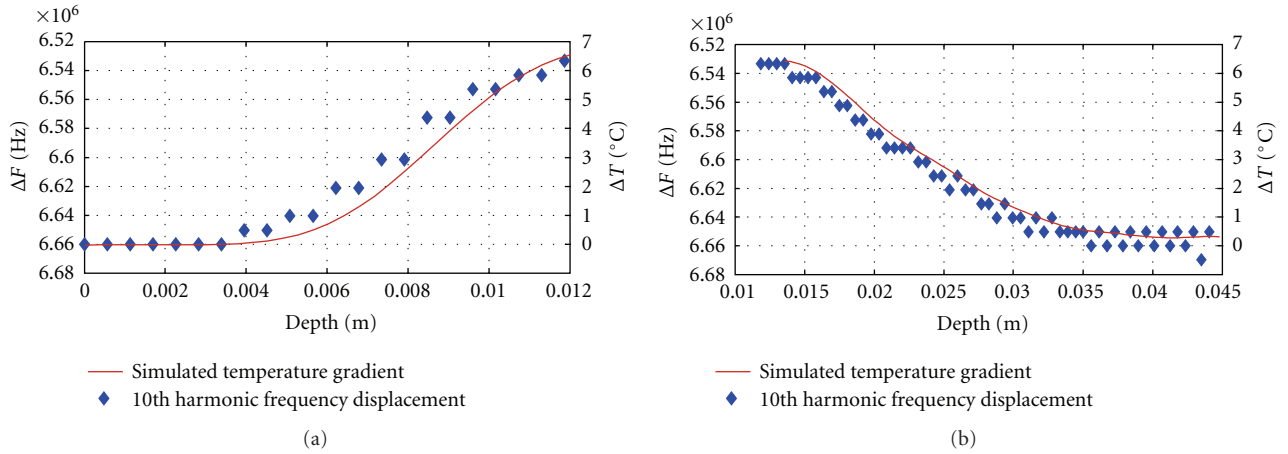

Figure 4: Some calculated results for spectral estimation of positive (a) and negative (b) thermal gradients (red curves) induced into a biological phantom.

temperature for distinct depths, are shown in Figure 4. It can be appreciated a good correlation with temperature changes for all the depths.

3. Results and Discussion

3.1. Evaluation of the New HR Spectral Technique for Thermal Estimation. Three specific computational methods were performed for this evaluation, applying them to inspect potential capacities of our improved spectral analysis technique to comply with the main aspects, around changes detection in the echo-signals behavior, which could be related to physical variations on tissue with diagnostic significance.

(i) The first evaluation method is oriented to an accurate assessment of the thermal resolution that potentially this tool is capable of providing, in the detection of the small changes (≈0.1°C) required in early detection of initial infections or tumors on real tissues (e.g., hepatitis).

(ii) The second evaluation method analyses affectations of noisy signals on high-resolution PSD results. The noise immunity, reached by the spectral technique itself, is a crucial factor due to the complex nature of real echo-signals; in fact, they contain noisy components that must be ignored, and, therefore, it is important to know the sensibility, of the main spectral processing stages, to the noise induced in the echo-traces, in order to design an efficient filtering preprocessing.

(iii) The third evaluation method is for studying the HR spectral results for random reflectors distributions, describing scattering in real biological tissues. Multiecho-signals with different standard deviations were processed to obtain their PSD, with the objective of providing a qualitative study considering the potential application of the theoretic HR spectral technique proposed here for possible future early diagnosis on different tissue compositions: from uniform and regular tissue structures to complex and heterogeneous internal organs in patients.

3.1.1. Limits on Resolution for Noninvasive Thermometry Using HR Spectral Analysis. In order to find the theoretic limits of the HR spectral analysis for thermometry in a favorable case (supposing a rather ideal frame), an extension of this technique was tested with well-controlled echographic ultrasonic signals, by numerically emulating typical echo-traces acquired from ideal regular biological media, and trying to detect very small changes in the frequency values related to very-light temperature variations, even of the order of 0.05°C. To ensure repetitive and comparable conditions for echoes generation, it was decided to simulate a set of pulsed multiecho signals in a specific temperature range (30-31°C) for three small thermal increments of 0.05°C, 0.08°C, and 0.1°C. The regular model in which the computational simulation was based on is described by (1) and (2). Previously to apply our HR spectral technique finding the resonance frequencies and associated harmonics, a mathematical calculation (based on theoretical fundaments) was performed to establish the expected values for the harmonics, and then selecting the most convenient for shift analysis.

A speed of sound of 1540 m/s and an average distance between scatters of 1.1 mm were supposed for an ideal tissue similar to liver. Looking only for becoming possible a numerical indication of the achieving of very-high thermal resolutions, searching their theoretic limits, the central frequency of the simulated transducer was ideally fixed for our simulation at 30 MHz, and an initial temperature equal to 30°C was considered. This elevated ultrasonic frequency only should be applicable in the medical practice for a particular thin biological tissue or sample (of only a few centimeters in depth), due to its extreme acoustical attenuation.

The fundamental resonance frequency f_1 in the scattered propagation media, for these parameters, was computed

with (6), and a value of 700 KHz was obtained. Later, the harmonic of f_1, nearest to the transducer central frequency value, was properly chosen, in order to avoid that the selected harmonic was cut away due to filtering effects of the own testing ultrasonic transducer. So, the 43rd harmonic was selected with a frequency value of 30.1 MHz. For completing the spectral analysis, the expected frequency shifts of this 43rd harmonic, due to three defined temperature rises, were determined by means of the expression (7). In the Table 1, the calculated frequency displacements for the three studied basic steps in temperature increments are listed.

Graphical and numerical results were obtained, calculating the power spectral density of the simulated multiecho signals, by means of a computational algorithm developed for this objective. In Section 3.2, the results of each analysis stage are discussed.

3.1.2. Evaluation of the Sensibility to Noise for the HR Spectral Estimation Technique. An extended analysis of the sensibility to noise intends to raise an evaluation process to our improved spectral technique, when it is applied to ultrasonic echoes contaminated with increasing relative levels of noise, in order to establish the sensibility threshold level (in SNR terms) of this procedure and investigate which factors are mainly affected by the induced noise (when this happens). The initial ultrasonic multiecho signals, to be used for it, were computationally simulated in base to the simplest mathematical model described in Section 2.2 for regular texture tissues, equal as for the further analysis, considering a speed of sound of 1540 m/s and an average distance among scatters of 5 mm in this case, which produce a fundamental resonance frequency of 154 KHz.

Then, thermally altered signals were generated in a temperature range (30°C–50°C), in 2°C steps. And the SNR levels were calculated by an algorithm that generates white Gaussian noise amplitudes based on the signal power. The generated noises had average powers with values ensuring that the SNR was in a range between 3 dB and 120 dB. Finally, these SNR levels were added to multiecho signals, and the noise sensibility was analyzed from the power spectral density of each signal, with SNR: 1, 3, 6, 12, 30, 60, and 120 dB. The observed behaviors on the PSD's are discussed in Section 3.2.

3.1.3. Spectral Analysis Applied to Echoes from Statistical Randomly Distributed Scatters. Several nonuniform distributed multiecho traces were generated, varying standard deviation of the inter-arrival time between consecutive scattering echoes. Signals with a quasi-uniform echo distribution, and also with great variation in scatter distance, were obtained for an initial temperature of 30°C. A sound velocity of 1540 m/s and an average inter-arrival time of 800 ns were considered. This corresponds to an average distance between scatters of 0.6 mm and an average fundamental medium resonance of 1.2 MHz. The transducer central frequency is 10 MHz with a bandwidth of 1.5 MHz.

The high resolution power spectral density was obtained in each signal, for analyzing frequency peaks behaviors and their changes with echoes inter-arrival time variations.

Table 1: Expected displacements due to basic temperature rises for the 43rd harmonic.

Temperature rise (°C)	Harmonic displacement (Hz)
0.1	871.66
0.08	697.03
0.05	435.83

3.2. Discussion of Results in the Three Evaluations of the HR Spectral Technique. The results obtained in each specific evaluation case, planned in Section 3.1, are presented and discussed in following subsections, each one corresponding with results of each case.

3.2.1. Analysis of Limits in the Basic Thermal Resolution. A specific signals processing was carried out for three signals sets, considering constant temperature raises ΔT of 0.05°C, 0.08°C, and 0.1°C. The functional parameters for computing the PSD's were settled to ensure the achieving of the required frequency resolution. For the signals set that simulates the effects of a temperature rise from 30 to 31°C, in steps of 0.05°C, it was not possible to obtain an adequate and coherent PSD's result, due to "sampling" limitations in a typical portable computing context; in fact, for getting a good frequency resolution, giving a step around 400 Hz, the PSD calculation requires a very large number of samples (in the order of 16×10^6), and the available portable hardware (Laptop HP, AMD Turion 64 x 2 processor, 2 GB of memory) for signal processing did not fulfill the memory requirements for the algorithm computation. As a future work, in order to solve this hardware limitation, an increment in memory capacity should be considered, that in terms of a clinical application, it represents just a higher cost tool with not technological limitations associated in this aspect.

In the other evaluations cases planed, the PSD computation could be performed without mayor problems. A zoom of the 43rd harmonic peak shifts obtained by PSD display, for increments of 0.08°C and 0.1°C, is shown in Figures 5(a) and 6(a), where the displacement of the selected frequency peak can be clearly appreciated in each case.

In Figure 5(b), the 43rd harmonic shift values, versus a thermal rise from 30 to 30,6°C, are shown, in steps of 0.08°C. A quasilinear relation can be appreciated in the behavior of this harmonic with temperature changes.

The average frequency shifts, obtained per each 0.08°C of rising, were jumps of 733.59 Hz. Nevertheless, it must be noted that an anomalous jump of 1.1921 KHz (i.e., a light increment of 458 Hz) was produced every 0.32°C interval. It can be produced, perhaps, due to accumulative percentage errors related to PSD frequency resolution. This is a significant factor to be taken into account to avoid light measurement errors, which could be smoothed by some averaging technique, for instance, after performing several times the PSD calculation for echo-signals obtained in the same temperature range but setting lightly different initial temperatures in each time.

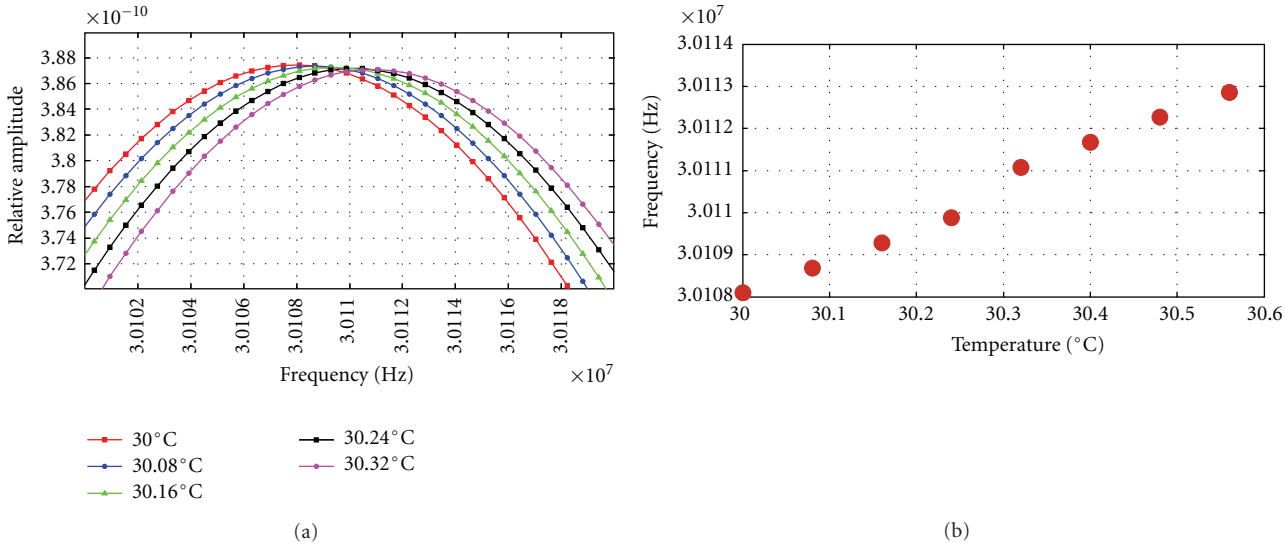

Figure 5: (a) Zoom of 43rd harmonic peak displacement obtained from PSD calculations of multiecho signals simulated for increments of 0.08°C. (b) 43rd harmonic peak values versus temperature elevation (from 30°C to 30.6°C) for a given constant increment of 0.08°C.

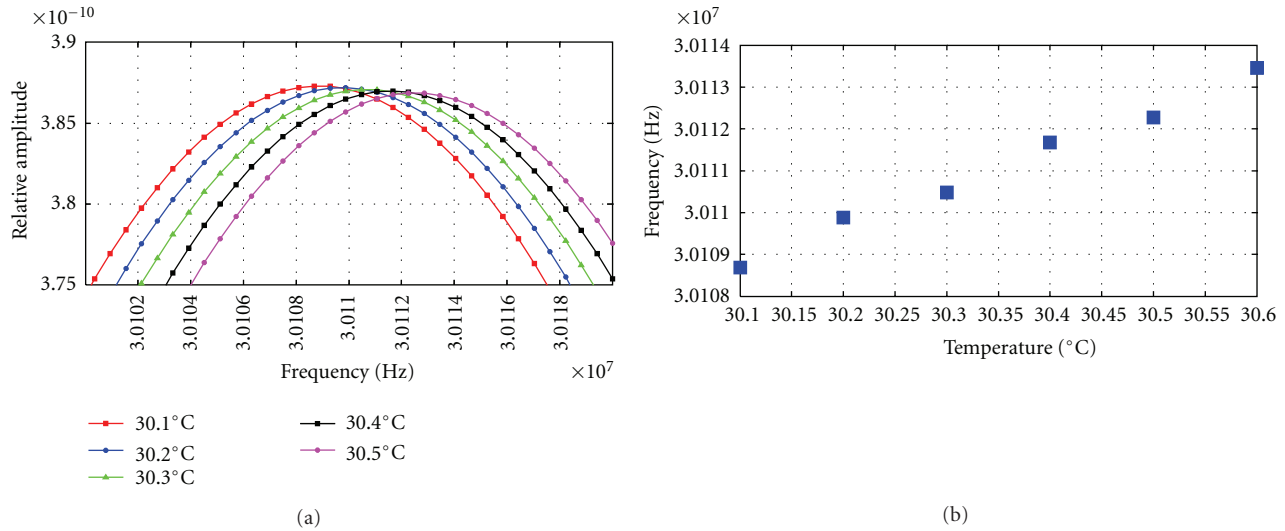

Figure 6: (a) Zoom of 43rd harmonic peak displacement obtained from PSD calculations of multiecho signals simulated in increments of 0.1°C. (b) 43rd harmonic peak values versus temperature elevation (from 30,1 to 30.6°C) for a given constant increment of 0.1°C.

And in Figure 6(b), the 43rd harmonic shifts versus a thermal rise from 30,1 to 30,6°C, in steps of 0.10°C, are shown. In this case, a linear relation can be also appreciated in the behavior of this harmonic with the temperature changes. The average displacement, obtained in this harmonic, from a temperature increment of 0.1°C was 927.18 Hz.

3.2.2. Noise Sensibility Analysis. Frequency peak values alterations related to the corresponding overtones from the calculated PSD distributions were obtained, for the simulated echo-signals with distinct added noises described above, and the following interesting phenomena were observed.

(a) All the PSD plots obtained for a certain noise level present a shift from the nominal overtone value (frequency peak corresponding to signal without noise). In order to evaluate the noise sensibility of the spectral estimation, several SNR levels were generated and processed; in this paper the most representative SNR levels are presented to show the performance of technique under low and high level SNR conditions. Taking a particular case, in the 13 harmonic of the signals (with SNR = 1, 3, 6 and 120 dB) at 30°C, the greatest error detected corresponds to the signal with a SNR = 3 dB; the expected theoretical value of this harmonic was 2.0020 MHz, but the real value (from a nonnoisy signal) was 2.0276 MHz, and a value of 2.0244 MHz was obtained for a noisy signal with an SNR = 3 dB, which means a difference

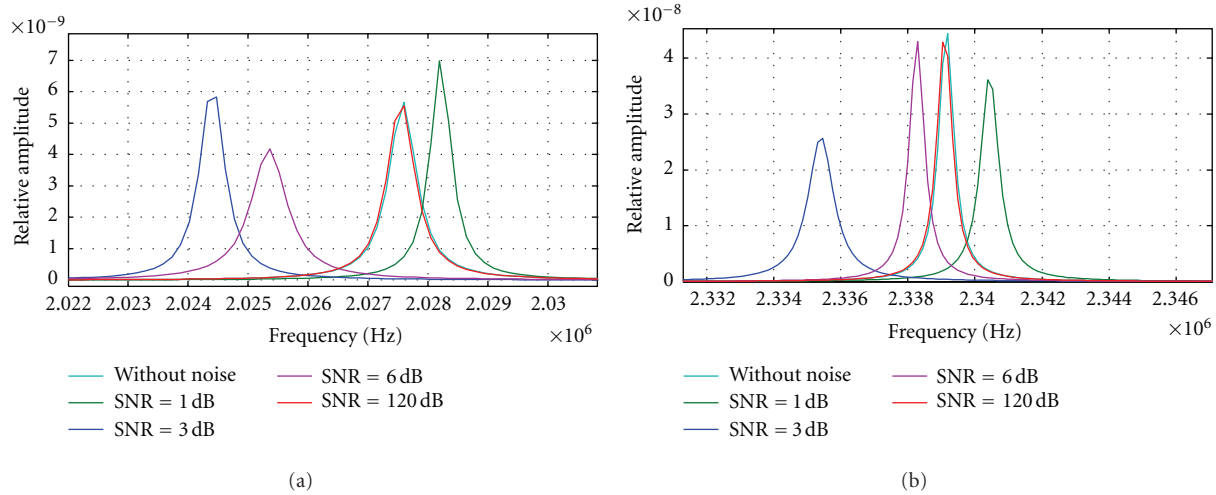

Figure 7: (a) 13 harmonic peak value changes for signals numerically simulated at 30°C and with different levels of SNR. (b) 15 harmonic peak value changes for signals simulated at 30°C and with different levels of SNR.

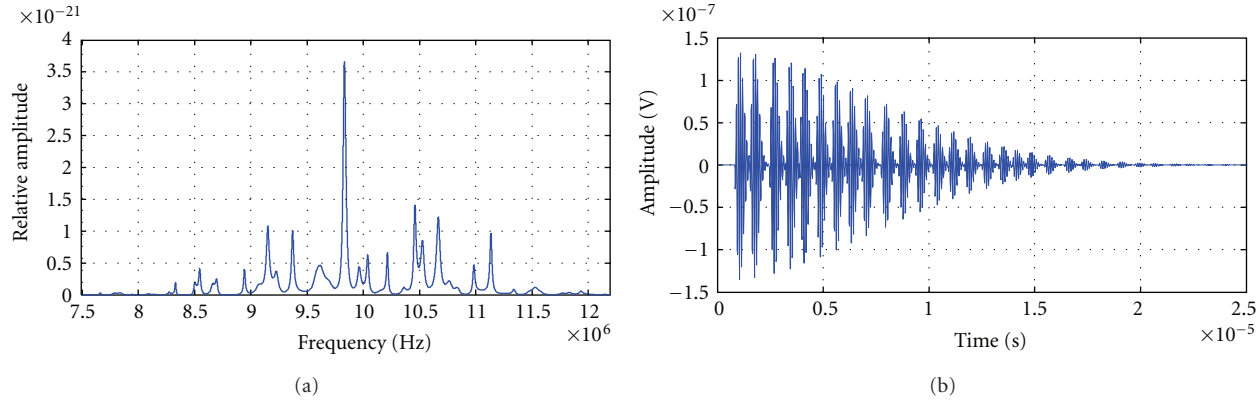

Figure 8: (a) Power spectral density of a simulated signal with an average interarrival time equal to 800 ns and a variance equal to 0.0064 ps^2(S.D. = 80 ns). (b) Simulated signal in time domain with an average interarrival time equal to 800 ns and a variance equal to 0.0064 ps (S.D. = 80 ns).

of −1.2143°C from the case without noise. This represents a rather significant error, for instance, on applications of thermal monitoring during treatments of hyperthermia.

(b) Amplitudes of frequency peaks corresponding to overtones of the fundamental resonance also were modified with the noise level increments, in some cases,

(c) Signal with a little added noise giving a high SNR = 30, 60 and 120 dB did not present a detectable displacement in their harmonic resonance values in respect to the signal without noise. This could be interpreted as a preliminary indication of SNR threshold for signal immunity in the spectral analysis to be applied to noisy signals.

In Figures 7(a) and 7(b), the 13 and 15 harmonic curves for signals, taken at 30°C, but with different SNR levels, are shown for five distinct SNR values, selected as the more significant among all the curves calculated; for intermediate values below 120 dB, the frequency alteration in overtones by these noise levels can be considered not relevant.

3.2.3. Results of Spectral Analysis with Nonregular Scattering Echo-Signals. Figures 8 to 10 show simulated signals, in MHz range, with an average inter-arrival time equal to 800 ns and a variance of 0.0064 ps^2, 0.64 ps^2 and 6.4 ps^2 (corresponding to a standard deviation SD of 80 ns, 0.8 μs and 2.52 μs), respectively, and theirs power spectral densities. The quasiregular signal, which corresponds to the smallest variance signal (shown in Figure 8), presents a very well-defined frequency peak value of 9.8345 MHz and several peaks of smaller amplitude located in greater and smaller values. This PSD behavior is related to the quasiuniform distribution of scatters (Figure 8(b)), which produce the resonant peak nearest to the "ideal 8th harmonic value" of 10 MHz, which would be obtained in the case that no deviations exist.

The following cases correspond to signals with higher variance, 0.64 ps^2 and 6.4 ps^2, in inter-arrival time between echoes (Figures 9(b) and 10(b) resp.). In the PSD's obtained for the cases shown on Figures 9(a) and 10(a), new

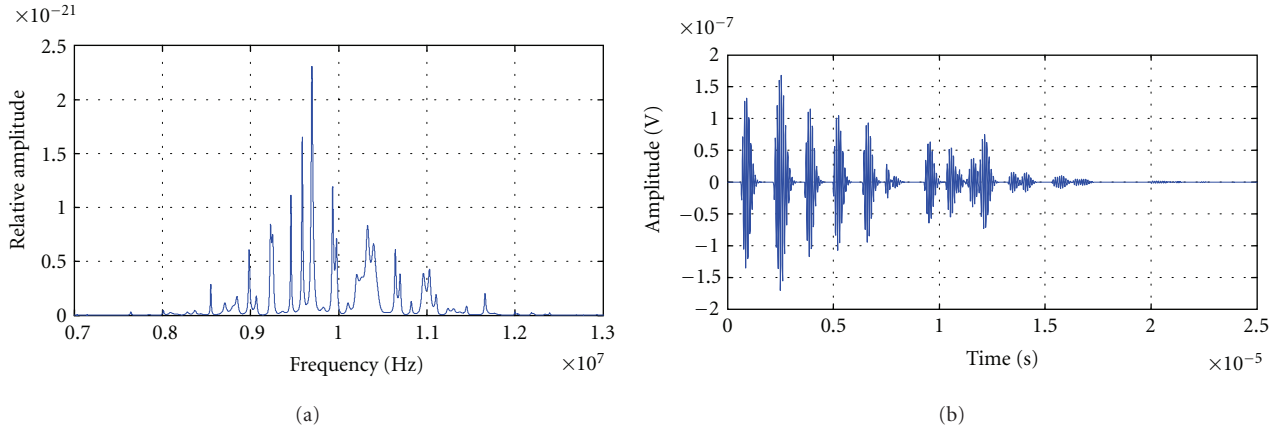

(a) (b)

Figure 9: (a) Power spectral density of a simulated signal with an average interarrival time equal to 800 ns and a variance equal to 0.64 ps^2 (S.D. = 0.8 μs). (b) Simulated signal with an average inter-arrival time equal to 800 ns and a variance equal to 0.64 ps^2 (S.D. = 0.8 μs).

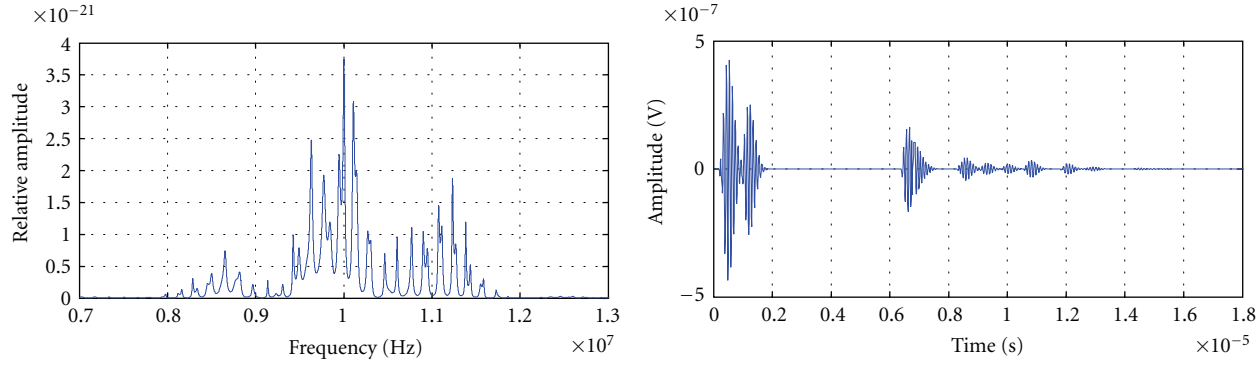

(a) (b)

Figure 10: (a) Power spectral density of a simulated signal with an average interarrival time of 800 ns and a variance equal to 6.4 ps^2 (S.D. = 2.52 μs). (b) Simulated signal with an average interarrival time of 800 ns and a variance of 6.4 ps^2 (S.D. = 2.52 μs).

frequency peaks can be distinguished, and their amplitudes tend to grow proportionally, increasing with variance, and diminishing the relevance of just one peak related to scatters distribution.

4. Conclusions and Future Perspectives

The ultrasonic estimation of little internal thermal gradients into patient tissues could be an effective method as a complementary tool for future noninvasive early diagnosis. The use of techniques based on spectral changes detection in ultrasonic echo-traces seems to be a promising option in this context, but associated spatial resolutions must be improved, in order to detect thermal differences among very close tissue points, as required for instance in initial phases with very small tumors.

Limitations of current research proposals to achieve a noninvasive ultrasonic thermal estimation inside tissues by overtones spectral analysis were analyzed with controllable and repetitive biological and numerical phantoms, giving some ways to overcome them.

By a mathematical modeling of thermal echo alterations, the possibility of achieving good temperature resolutions has been investigated. So, the applicability of an improved approach (for thermal estimation processes from the outer of scattered biological phantoms) generated by the authors, to achieve high-resolution in temperature (up to 0,08°C) has been shown by performing computer simulation of realistic models for multiple-echo ultrasonic traces coming from scattered media, like liver.

An accurate evaluation of performance was performed, for raw bioultrasonic signals patterns (deterministic echo-pulses from regular structure phantoms, and also more complex echo-traces from randomly distributed scattered media). The potential effectiveness of our approach, as a possible reliable diagnosis tool, was demonstrated. It is based on an implementation of the Burg algorithm and adding a new processing step to obtain a higher resolution in the frequency peaks measure of the spectrum overtones. Other advantage of this approach, in respect to possible alternatives based on complex imaging systems, is that only one transducer and signal acquisition channel are needed.

The sensibility of the new spectral measurement technique, with regard to different levels of time variance and noise in the echoes, has been evaluated, using realistic bioultrasonic signals contaminated with noise, for SNR ranging between 1 and 120 dB. The technique shows a reasonable robust response to echo variance and for SNR above of 3–6 dB, which is fulfilled by the most of ultrasonic echo-signals acquired from biological tissues. Nevertheless, looking forward a practical low-cost ultrasonic implementation (e.g., based on a commercial PC-compatible card), it is recommended to consider at less a simple general purpose analog preprocessing hardware for band-pass filtering of the echo-signals, before being sent for software spectral analysis for instance in a portable computer. In this way, possible undesirable frequency peaks shifts, due to the presence of some noise in the echoes, could be avoided.

But, there are still some aspects that have to be investigated and improved to achieve a whole robust application of the HR echoes spectral estimation technique, as usable ultrasonic signal processing tool, clinically available as dedicated instrumental units for practical and accurate diagnosis on distinct tissues. The improvements to be made in the estimation procedure would be related with the development of a number of software options for the detection algorithm to match it to different tissues (liver, muscle, breast, fat presence, etc.), and also for trying to combine this HR spectral technique with other possible measurement ultrasonic techniques, developed in the time and phase domains. In particular, it seems of quite interest, for some noninvasive diagnostic applications, the combination of the HR spectral analysis with advanced ultrasonic elastography.

Acknowledgments

This work was developed in the frame of the Project CONACYT-FOMIX (Estado de Veracruz) N. 128572, Mexico (*Modeling and Computational Analysis of HF Ultrasonic Pulses for the Proposal of Low-Cost Effective Diagnosis Methods of Infectious Diseases in Patients*), and in part was sponsored by the National Plan of Spanish Ministry of Science and Innovation" (Projects DPI2008-05213 and DPI2011-22438). And our acknowledgment to the R&D institutions: IPN (México), CSIC (Spain) and URU (Uruguay).

References

[1] T. C. Robinson and P. P. Lele, "An analysis of lesion development in the brain and in plastics by high-intensity focused ultrasound at low-megahertz frequencies," *Journal of the Acoustical Society of America*, vol. 51, no. 4, pp. 1333–1351, 1972.

[2] R. Maass-Moreno and C. A. Damianou, "Noninvasive temperature estimation in tissue via ultrasound echo-shifts. Part I. Analytical model," *Journal of the Acoustical Society of America*, vol. 100, no. 4, pp. 2514–2521, 1996.

[3] R. Maass-Moreno, C. A. Damianou, and N. T. Sanghvi, "Noninvasive temperature estimation in tissue via ultrasound echo-shifts. Part II. In vitro study," *Journal of the Acoustical Society of America*, vol. 100, no. 4, pp. 2522–2530, 1996.

[4] L. Castéra, B. L. Bail, F. Roudot-Thoraval et al., "Early detection in routine clinical practice of cirrhosis and oesophageal varices in chronic hepatitis C: comparison of transient elastography (FibroScan) with standard laboratory tests and non-invasive scores," *Journal of Hepatology*, vol. 50, no. 1, pp. 59–68, 2009.

[5] L. G. Cui, J. H. Shao, J. R. Wang, J. Bai, and Y. Z. Zhang, "Ultrasound elastography of ethanol-induced hepatic lesions: in vitro study," *Chinese Medical Sciences Journal*, vol. 24, no. 2, pp. 81–85, 2009.

[6] S. Dasarathy, J. Dasarathy, A. Khiyami, R. Joseph, R. Lopez, and A. J. McCullough, "Validity of real time ultrasound in the diagnosis of hepatic steatosis: a prospective study," *Journal of Hepatology*, vol. 51, no. 6, pp. 1061–1067, 2009.

[7] N. Goyala, N. Jaina, V. Rachapallia, D. L. Cochlina, and M. Robinsonb, "Non-invasive evaluation of liver cirrhosis using ultrasound," *Clinical Radiology*, vol. 64, no. 11, pp. 1056–1066, 2009.

[8] N. F. Schwenzer, F. Springer, C. Schraml, N. Stefan, J. Machann, and F. Schick, "Non-invasive assessment and quantification of liver steatosis by ultrasound, computed tomography and magnetic resonance," *Journal of Hepatology*, vol. 51, no. 3, pp. 433–445, 2009.

[9] B. Boozari, A. Potthoff, I. Mederacke et al., "Evaluation of a novel ultrasound method for the detection of liver fibrosis—prospective comparison with transient dynamic elastography and histology," *Journal of Hepatology*, vol. 52, p. S404, 2010.

[10] R. Seip and E. S. Ebbini, "Noninvasive estimation of tissue temperature response to heating fields using diagnostic ultrasound," *IEEE Transactions on Biomedical Engineering*, vol. 42, no. 8, pp. 828–839, 1995.

[11] R. Seip, "Noninvasive real-time multipoint temperature control for ultrasound phased array treatments," *IEEE Transactions on Ultrasonics, Ferroelectrics, and Frequency Control*, vol. 43, no. 6, pp. 1063–1073, 1996.

[12] D. Liu and E. S. Ebbini, "Real-time 2-D temperature imaging using ultrasound," *IEEE Transactions on Biomedical Engineering*, vol. 57, no. 1, Article ID 5306150, pp. 12–16, 2010.

[13] I. Bazán, M. Vazquez, A. Ramos, A. Vera, and L. Leija, "A performance analysis of echographic ultrasonic techniques for non-invasive temperature estimation in hyperthermia range using phantoms with scatterers," *Ultrasonics*, vol. 49, no. 3, pp. 358–376, 2009.

[14] R. F. Wagner, M. F. Insana, and D. G. Brown, "Statistical properties of radio-frequency and envelope-detected signals with applications to medical ultrasound," *Journal of the Optical Society of America A*, vol. 4, no. 5, pp. 910–922, 1987.

[15] K. A. Wear, R. F. Wagner, F. M. Insana, and T. J. Hall, "Application of autoregressive spectral analysis to cepstral estimation of mean scatterer spacing," *IEEE Transactions on Ultrasonics, Ferroelectrics and Frequency Control*, vol. 40, no. 1, pp. 50–58, 1993.

[16] L. Landini and L. Verrazzani, "Spectral characterization of tissues microstructure by ultrasounds: a stochastic approach," *IEEE Transactions on Ultrasonics, Ferroelectrics, and Frequency Control*, vol. 37, no. 5, pp. 448–456, 1990.

[17] P. M. Shankar, "A model for ultrasonic scattering from tissues based on the K distribution," *Physics in Medicine and Biology*, vol. 40, no. 10, pp. 1633–1649, 1995.

[18] I. Bazán, *Evaluation and Improvement of Ultrasonic Techniques for Non Invasive Estimation of Internal Thermal Distributions on Biologic Phantoms with Scatters*, Doctorate Thesis, Department of Electrical Engineering, Cinvestav-IPN, Mexico City, Mexico, 2009.

[19] L. Weng, J. M. Reid, P. M. Shankar, K. Soetano, and X. M. Lu, "Nonuniform phase distribution in ultrasound speckle analysis—II: parametric expression and a frequency sweeping technique to measure mean scatterer spacing," *IEEE Transactions on Ultrasonics, Ferroelectrics, and Frequency Control*, vol. 39, no. 3, pp. 360–365, 1992.

[20] S. L. Marple Jr., Ed., *Digital Spectral Analysis with Applications*, Prentice Hall, New York, NY, USA, 1987.

[21] J. G. Proakis and D. G. Manolakis, Eds., *Digital Signal Processing: Principles, Algorithms and Applications*, Prentice Hall, New York, NY, USA, 3rd edition, 1996.

[22] E. N. Bruce, *Biomedical Signal Processing and Signal Modeling*, John Wiley and Sons, New York, NY, USA, 2001.

[23] I. Bazán, A. Ramos, A. Vera, R. Posada, and L. Leija, "Non-invasive estimation of a non-linear temperature gradient using spectral analysis of multi-echo ultrasonic signals," in *Proceedings of the 6th International Conference on Electrical Engineering, Computing Science and Automatic Control (CCE '09). IEEE Cat. number CFP09827*, pp. 372–376, Toluca, Mexico, January 19, 2010.

Hindawi Publishing Corporation
Computational and Mathematical Methods in Medicine
Volume 2012, Article ID 290360, 6 pages
doi:10.1155/2012/290360

Research Article

A Mathematical Modelling Approach for Systems Where the Servers Are Almost Always Busy

Christina Pagel,[1] David A. Richards,[2] and Martin Utley[1]

[1] *Clinical Operational Research Unit, University College London, 4 Taviton Street, London WC1H 0BT, UK*
[2] *Psychology, College of Life and Environmental Sciences, University of Exeter, Perry Road, Exeter EX4 4QG, UK*

Correspondence should be addressed to Christina Pagel, c.pagel@ucl.ac.uk

Received 15 November 2011; Accepted 23 January 2012

Academic Editor: John Hotchkiss

The design and implementation of new configurations of mental health services to meet local needs is a challenging problem. In the UK, services for common mental health disorders such as anxiety and depression are an example of a system running near or at capacity, in that it is extremely rare for the queue size for any given mode of treatment to fall to zero. In this paper we describe a mathematical model that can be applied in such circumstances. The model provides a simple way of estimating the mean and variance of the number of patients that would be treated within a given period of time given a particular configuration of services as defined by the number of appointments allocated to different modes of treatment and the referral patterns to and between different modes of treatment. The model has been used by service planners to explore the impact of different options on throughput, clinical outcomes, queue sizes, and waiting times. We also discuss the potential for using the model in conjunction with optimisation techniques to inform service design and its applicability to other contexts.

1. Introduction

Health treatment activities where arriving patients might have to wait for treatment and where duration of treatment follows a certain probability distribution have often been modelled using queueing theory. A classic example is the study of accident and emergency departments in acute hospitals [1, 2]. However in situations where "treatment" consists of a set of distinct treatment types, with the possibility of queues at each treatment stage, and the possibility of receiving a given type of treatment more than once, the use of queueing theory becomes very complex [3, 4].

The provision of mental health care for depression and anxiety in the primary care system is one such complex system. A configuration for mental health care delivery called "stepped care" is advocated for patients with common mental health problems [5, 6] to replace traditional systems (see Figure 1). Stepped care [7] is based on two principles: (a) "least burden," so that an intervention received by a patient should be effective and appropriate whilst burdening the patient and the health care system as little as possible [8] and (b) "self-correction," the provision of a system in place to detect lack of improvement, which in turn leads to alternative more intensive treatments being offered [9]. Thus, in a stepped care system, patients are typically first considered for low-intensity interventions such as guided self-help, group work, or a short course of individual therapy. High-intensity interventions typically involve many sessions with a highly trained professional, such as a cognitive behavioural therapist. There are many different types of both low-intensity and high-intensity interventions, and an individual patient can step both "up" to, or between, high intensity treatments and "down" to, or between, low-intensity treatments.

The introduction of stepped care within an existing mental health care framework is challenging. Planning the delivery of stepped care requires decisions concerning the treatments to be offered, the number and type of staff, the protocol for how patients transfer between treatments, and the balance of provision between low and high intensity treatments. The other key feature of mental health care systems other than their complexity is that they are often

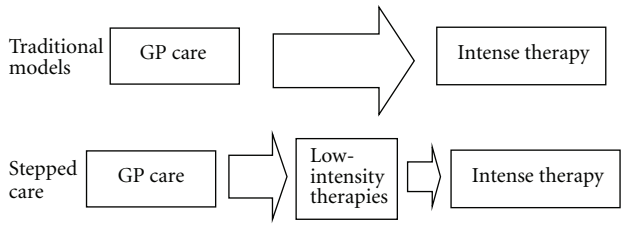

Figure 1: A diagram highlighting the difference between a traditional care model and the stepped care model. GP: General Practitioner.

operating at capacity. This is more feasible than in acute hospital environments since patients in the queue effectively wait "at home" using little resource.

In this paper we describe a mathematical model we have developed to help planners design a stepped care mental health system [10, 11], by providing rapid estimates of throughput and changes in waiting times for different potential configurations. This model was implemented within a software tool that was distributed to pilot primary mental health care providers [11]. We note that the mathematics presented here, although discussed in the specific context of mental health care delivery, is intended to be generic and is suitable for many other systems that meet certain assumptions.

2. Methods: Mathematical Model

The approach used is complementary to traditional queueing theory and is most suited to systems where traffic intensities are greater than or equal to one or to a system where the starting states have large queues. It complements recent work on queueing systems where some of the servers are always busy [12]. Additionally, this analysis is not dependent on the distributions of arrivals or duration of treatment. We note that where the traffic intensity is greater than one, there is no mathematical steady state to the system (since queues will increase indefinitely). However, the features of the system can still be explored within a specified time frame to understand better the distribution of demand between servers and the potential impact of increased or redistributed capacity.

2.1. A Single Treatment Slot

2.1.1. Assumptions. The unit of capacity we consider in this analysis is a time slot in a diary (e.g., a therapy session) and we assume that patients are treated in discrete sessions. A given time slot in a diary is assumed to be devoted to one, and only one, distinct treatment type. We further assume that a patient takes at least one session to be treated, and that at the start of the modeled period there is no patient currently undergoing treatment (i.e., at $t = 0$ the time slot is either empty or a patient has just started their treatment). We assume that durations of treatment of different patients are independent of one another.

2.1.2. Notation. For $x \geq 1$, let p_x denote the probability that a patient's treatment time is exactly x time units. Define $p_0 = 0$.

For $x \geq 1$, let s_x denote the probability that a patient's treatment time is strictly longer than x time units. Define $s_0 = 1$.

For $i \geq 1$, $t \geq 1$ let $r_{i,t}$ be the probability that exactly i patients have completed their treatment and that no other patient has started their treatment by time t. Define $r_{i,0} = 0$ for $i \geq 1$.

For $i \geq 1$, $T \geq 1$, let $f_{i,T}$ be the probability that at time T exactly i people have completed their treatment. Note that another patient may have started. Define $f_{i,0} = 0$ for $i \geq 1$.

2.1.3. The Distribution for the Number of People Who Have Completed Treatment by Time T. We begin by considering $r_{1,t}$, the probability that by time $t \geq 1$ exactly one person has arrived and left and no one else has yet started

$$r_{1,t} = p_t. \tag{1}$$

We can then define $r_{i,t}$ iteratively:

$$r_{i,t} = \sum_{k=1}^{t} r_{i-1,k} r_{1,t-k} = \sum_{k=1}^{t} r_{i-1,k} p_{t-k}. \tag{2}$$

Thus we have derived an expression for the probability that at some time t, i people have been treated and no one else has yet started. To relax this latter condition, we now consider $f_{i,T}$, the probability that at some time T, exactly i people have completed their treatment. We use $r_{i,k}$ to calculate this and for a given time T:

$$f_{i,T} = \sum_{k=1}^{T} r_{i,k} s_{T-k}. \tag{3}$$

2.2. A Network of Treatment Slots. We now extend the concept of a single treatment slot to a network of treatment slots that can be thought of as representing a given system.

2.2.1. Notation. Consider a treatment slot of type i, for $i = 1 \cdots L$ and absorbing exit states of type i, for $i = L+1 \cdots M$. There are a constant number, N_i, of each type of treatment slot or exit state for $i = 1 \cdots M$ where $N_i = 1$ for $i = L + 1 \cdots M$.

Let α_{ij} be the probability that a person leaving a slot of type i, for $i = 1 \cdots M$ goes to a treatment slot or exit state of type j for $j = 1 \cdots M$. Define $\alpha_{ij} = 0$, for all $i = L+1 \cdots M$ and $j = 1 \cdots M$ (i.e., no one leaves an exit state).

Define the random variable X_i as the number of people who have left a single treatment slot of type i, in a given time period for $i = 1 \cdots L$. The expectation and variance of X_i are denoted $E(X_i)$ and $\mathrm{Var}(X_i)$, and we assume that these quantities are well defined.

Let λ_i be the Poisson arrival rate from outside the system to a slot of type i. Define $\lambda_i = 0$, for all $i = L + 1 \cdots M$ (i.e., no arrivals to exit states from outside the system).

Define the random variable W_{ij} as the number of people who have arrived at the queue for any slot of type j from

a single treatment slot i, in a given time period for $j = 1 \cdots M$ and $i = 1 \cdots L$.

Define the random variable Y_{ij} as the number of people who have arrived at the queue for any slot of type j from all N_i treatment slots i, in a given time period for $j = 1 \cdots M$ and $i = 1 \cdots L$.

Define the random variable Y_j as the number of people who have arrived at the queue for any slot of type j in a given time period for $j = 1 \cdots M$.

Define $B(p)$ as the Bernouilli distribution with parameter p, where $0 \le p \le 1$.

Define $G_Y(s)$ as the generating function associated with any given probability distribution Y.

2.2.2. General Results from Probability Theory. For a constant number N_i of independent random variables X_i,

$$E\left(\sum_{k=1}^{N_i} X_i\right) = \sum_{k=1}^{N_i} E(X_i) = N_i E(X_i),$$
$$\mathrm{Var}\left(\sum_{k=1}^{N_i} X_i\right) = \sum_{k=1}^{N_i} \mathrm{Var}(X_i) = N_i \,\mathrm{Var}(X_i). \tag{4}$$

If a positive integer-valued distribution Z has generating function $G_Z(s)$ and a probability distribution Y has generating function $G_Y(s)$ then the distribution $W = \sum_{k=1}^{Z} Y$ has generating function:

$$G_W(s) = G_Z(G_Y(s)). \tag{5}$$

Additionally the expectation and variance of Y are given by

$$E(Y) = G_Y'(1),$$
$$\mathrm{Var}(Y) = G_Y''(1) + E(Y) - E^2(Y). \tag{6}$$

Proof of these results can be found in Grimmett and Stirzaker [13].

2.3. Flows through a Treatment in a General Network. Consider a treatment in a general network as shown in Figure 2. Here we consider flows in and out of a constant number, N_j, of units of capacity of type j. In this "always full" system, people arriving at a treatment slot of type j will first enter a queue of unlimited size. The number of people in a queue waiting to enter any treatment slot of type j is denoted Q_j. In what follows, we assume that there is no balking, but balking could be added to the system by specifying a maximum queue size.

As shown in Figure 2, flows into the queue for any slot of type j can come from either other units of capacity of type $i \neq j$ or from outside the system for $j = 1 \cdots L$. In the special case of an exit state, there are no external arrivals and only one state of each type.

2.3.1. Inputs from a Treatment Slot of Type i. For each person leaving a particular treatment slot of type i, for $i = 1 \cdots L$,

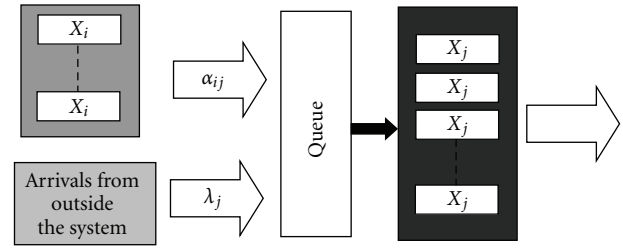

Figure 2: Flows in and out of treatment slots of type j.

we can consider their destination as a Bernouilli trial, where they will enter the queue for a slot of type j with probability α_{ij}. Over a given time period, we thus have a random number X_i of Bernouilli trials. Then

$$W_{ij} = \sum_{k=1}^{X_i} B_k\left(\alpha_{ij}\right). \tag{7}$$

From (5) and (6) we obtain the following (a more detailed derivation is given in the appendix):

$$E\left(W_{ij}\right) = \alpha_{ij} E(X_i),$$
$$\mathrm{Var}\left(W_{ij}\right) = {\alpha_{ij}}^2 \,\mathrm{Var}(X_i) + \alpha_{ij}\left(1 - \alpha_{ij}\right)E(X_i). \tag{8}$$

Equation (8) give the expectation and variance for the total number of people who have arrived at the queue for a treatment slot of type j from a particular treatment slot of type i over the given time period. However, we have a block of N_i units of capacity of type i so we use (4) to derive the total number of people, Y_{ij}, who arrive at the queue for any treatment slot of type j from the block of units of capacity of type i over the given time period:

$$E\left(Y_{ij}\right) = N_i \alpha_{ij} E(X_i),$$
$$\mathrm{Var}\left(Y_{ij}\right) = N_i\left({\alpha_{ij}}^2 \,\mathrm{Var}(X_i) + \alpha_{ij}\left(1 - \alpha_{ij}\right)E(X_i)\right). \tag{9}$$

Thus

$$E\left(Y_j\right) = \lambda_j + \sum_{i \neq j} \alpha_{ij} N_i E(X_i),$$
$$\mathrm{Var}\left(Y_j\right) = \lambda_j + \sum_{i \neq j}\left({\alpha_{ij}}^2 N_i \,\mathrm{Var}(X_i) + \alpha_{ij}\left(1 - \alpha_{ij}\right)N_i E(X_i)\right), \tag{10}$$

where the sum is over all different types of treatment slot $i, i = 1 \cdots L$. Note that α_{ij} and λ_j can equal zero.

In circumstances where the network is always full, the output from units of capacity of type j for $j = 1 \cdots L$ is not dependent on the input into the queue. Thus the expected output from units of capacity of type j for $j = 1 \cdots L$ is

$$E(\mathrm{out}) = N_j E\left(X_j\right),$$
$$\mathrm{Var}(\mathrm{out}) = N_j \,\mathrm{Var}\left(X_j\right). \tag{11}$$

Table 1: Flows of patients between different types of appointment and two endpoints of the stepped care system.

From\To	Assessment	Low intensity	High intensity	Completed treatment	Dropped out of treatment
Assessment	0%	40%	20%	10%	30%
Low intensity	0%	0%	20%	50%	30%
High intensity	0%	0%	0%	80%	20%

We are now in a position to consider the expectation and variance of the change in the queue size Q_j:

$$E\left(\Delta Q_j\right) = \sum_{i \neq j} \alpha_{ij} N_i E(X_i) + \lambda_j - N_j E\left(X_j\right),$$

$$\mathrm{Var}\left(\Delta Q_j\right) = \sum_{i \neq j} \left(\alpha_{ij}{}^2 N_i \,\mathrm{Var}(X_i) + \alpha_{ij}\left(1 - \alpha_{ij}\right) N_i E(X_i)\right) + \lambda_j + N_j \,\mathrm{Var}\left(X_j\right). \tag{12}$$

Note that the variance of the change in queue size can be very large if there are a large number of potential inputs for that particular type.

For a patient waiting to receive treatment for a mental health problem, waiting time in a queue is more likely to be of concern than the actual number of people waiting. Let $1/\mu_j$ represent the mean number of sessions required to treat a patient in a unit of capacity of type j for $j = 1 \cdots L$. We can estimate the change in waiting time, ΔP_j for an individual arriving in the queue Q_j as

$$\Delta P_j = \frac{E\left(\Delta Q_j\right)}{\mu_j N_j}, \quad j = 1 \cdots L. \tag{13}$$

2.4. Potential for Optimisation. The linear nature of the equations above in terms of N_j suggests the possibility that linear programming techniques might be used to optimise the configuration of the stepped care system according to some relevant criteria. An illustrative optimisation is given below where there are a set of treatment types j and a desired outcome k (for instance successful discharge) and the intention is to find the allocation of sessions to types of treatments that maximises the number of people achieving the desired outcome. We note that different objective functions can be defined and that optimisation functionality was not included in the software tool [11] produced as part of this project.

2.4.1. Objective Function. Maximise:

$$Z = \sum_{j \neq k} \alpha_{jk} N_j E\left(X_j\right), \quad j = 1 \cdots L,\ L < k \leq M. \tag{14}$$

2.4.2. Constraints.

(1) N_j are positive integers, $j = 1 \cdots L$

(2) Total number of therapy sessions per week: $\sum_{j=1}^{L} N_j \leq S$ for some integer S.

Table 2: Arrivals to the system and allocation of resources within the system.

Appointment type	Average number of new, external arrivals every week	Weekly appointment slots allocated
Assessment	20	30
Low intensity	10	40
High intensity	0	30

(3) Total number of sessions for a treatment of type j is dependent on number of therapists qualified to deliver that type of treatment and thus there are capacity constraints for each treatment type: $N_j \leq S_j$, where S_j are positive integers, $j = 1 \cdots L$.

(4) Specify a maximum increase in waiting time of W weeks at each step:

$$E\left(\Delta Q_j\right) \leq W N_j \mu_j,\ j = 1 \cdots L. \tag{15}$$

3. Results: Illustrative Example

This mathematical model has been implemented as part of a project examining the implementation of stepped care systems [11]. Here we give an illustrative example of its use on a hypothetical mental health care system and the subsequent potential for optimisation.

In this system there are three types of appointments available: an initial screening appointment, a low-intensity therapy appointment, and a high-intensity therapy appointment. People are either referred by their GP (General Practitioner) into the system in which case they begin with an assessment appointment or they can self-refer directly to low-intensity therapy treatment.

The proportion of patients moving between different types of appointment is shown in Table 1.

The health system managers have 100 weekly appointments available to cover all types of appointment. For the purposes of this example, we assume that the number of weekly booked sessions a patient uses for each type of treatment is exponential with means of 1, 3, and 6 for assessments, low-intensity and high-intensity sessions respectively. The arrivals and capacity allocation for the current system are given in Table 2.

Although the waiting times for screening and high-intensity treatments are acceptable, the increase in waiting time for a low-intensity appointment over 6 months is unacceptably long (12 weeks) (see columns 2 and 3 of Table 3). The manager wishes to optimise the allocation of

Table 3: Example use of optimisation to allocate available treatment slots to treatment types.

Appointment type/End point	Current weekly appointment slots allocated	Average increase in waiting time (weeks)	Suggested weekly appointment slots allocated	Average increase in waiting time (weeks)
Assessment	30	1.3	26	4
Low intensity	40	11.7	45	6
High intensity	30	7	29	7
Dropped out	*257*	—	*248*	—
Completed	**292**	—	**301**	—

appointment slots to appointment types to maximise the number of patients who successfully complete treatment in a 26-week period, according to the following constraints.

(1) There can be a maximum of 100 total allocated appointments.

(2) The maximum increase in average waiting time for an assessment is 4 weeks.

(3) The maximum increase in average waiting time for either low or high intensity treatment is 8 weeks.

(4) There must be at least 20 assessment sessions, 30 low-intensity, and 20 high-intensity sessions every week.

We ran this optimisation problem using Microsoft Excel Solver (version 2003). We note that Microsoft Solver is a standard add-in to Microsoft Excel and there exist several resources on its use within Excel (e.g., [14]). The new allocation and the output parameters calculated using the model are given in columns 4 and 5 of Table 3.

The suggested appointment schedule has resulted in a more even distribution of the expected waits for each type of treatment and increased the expected total number of people completing treatment over the 6-month time frame.

4. Limitations

A clear limitation is the assumption that the system is always busy. However, application of the model to any given system would still provide the maximum possible throughput of the system over a given period of time. In the context of a mental health system, other limitations apply. Firstly, all patients are considered to be homogeneous and no allowance is made for patients with different characteristics (for instance presenting problem) having different duration of stay distributions or different pathways through the system. Secondly, in this analysis, time is considered to be defined by the number of treatment slots and thus application to a system where sessions are not regularly spaced in time is more complicated. Finally, "holding" or "blocking back" behaviour is not accounted for in the model, in that both the duration of treatment and the destination of patients from each treatment are assumed independent of the state of the system.

5. Discussion

This mathematical model was developed in response to a specific problem within the configuration of mental health care services [10]. As part of that project, the model (without the optimisation aspect) has been implemented within a software tool developed to help planners explore the consequences of different configurations for a given mental health service. Details of the software tool and its use in designing stepped care systems can be found in the project final report [11].

We have described a simple way of analysing throughput and flows for a networked system in the situation where a system is always busy or where this is a reasonable approximation. We note that this is not a steady-state model and instead considers changes in mean output, queue sizes and waiting times over a relatively short (6 months) time period. We have also shown how optimisation techniques might be applied to the subsequent design of a network in the context of a mental health system.

This approach could be useful in other health systems where "servers" (whether beds, clinicians or other resources are always busy) but a key assumption that needs to be met is that there will always be a queue. In practice this assumption is less likely to be valid for systems where queues involve people waiting in a physical allocated space (for instance, in an emergency department) than where people can "virtually" wait at home. Nonetheless, considering such busy systems over a short amount of time using these sorts of models can provide insight into the allocation of resources and management of arrivals to complement standard steady state queuing theory.

Appendix

Remember that the random variable W_{ij} is defined as the number of people who have arrived at the queue for any slot of type j from a single treatment slot i, in a given time period for $j = 1 \cdots M$ and $i = 1 \cdots L$.

For each person leaving a particular treatment slot of type i, for $i = 1 \cdots L$, we can consider their destination as a Bernouilli trial, where they will enter the queue for a slot of type j with probability α_{ij}. Over a given time period, we thus have a random number X_i of Bernouilli trials. Then

$$W_{ij} = \sum_{k=1}^{X_i} B_k\left(\alpha_{ij}\right). \tag{A.1}$$

From (5) we know that

$$G_{X_{ij}}(s) = G_{X_i}(G_B(s)). \tag{A.2}$$

and thus

$$\begin{aligned} G'_{X_{ij}}(s) &= G'_{X_i}(G_B(s))G'_B(s), \\ G''_{X_{ij}}(s) &= G''_{X_{ij}}(G_B(s))\left(G'_B(s)\right)^2 + G'_{X_i}(G_B(s))G''_B(s). \end{aligned} \tag{A.3}$$

It is a standard result that $G_B(s) = (1 - \alpha_{ij}) + \alpha_{ij}s$, and so using this and (6) we obtain the following:

$$\begin{aligned} E\left(W_{ij}\right) &= \alpha_{ij}E(X_i), \\ \mathrm{Var}\left(W_{ij}\right) &= {\alpha_{ij}}^2\,\mathrm{Var}(X_i) + \alpha_{ij}\left(1 - \alpha_{ij}\right)E(X_i). \end{aligned} \tag{A.4}$$

Acknowledgments

This project was funded by the National Institute for Health Research Service Delivery and Organisation programme (Project no. 08/1504/109). The views expressed in this publication/presentation are those of the authors and not necessarily those of the NHS, the NIHR, or the Department of Health. The NIHR SDO programme is funded by the Department of Health.

References

[1] M. L. McManus, M. C. Long, A. Cooper, and E. Litvak, "Queuing theory accurately models the need for critical care resources," *Anesthesiology*, vol. 100, no. 5, pp. 1271–1276, 2004.

[2] J. K. Cochran and K. T. Roche, "A multi-class queuing network analysis methodology for improving hospital emergency department performance," *Computers and Operations Research*, vol. 36, no. 5, pp. 1497–1512, 2009.

[3] X. Song and M. Mehmet Ali, "A performance analysis of discrete-time tandem queues with Markovian sources," *Performance Evaluation*, vol. 66, no. 9-10, pp. 524–543, 2009.

[4] H. Daduna and R. Szekli, "On the correlation of sojourn times in open networks of exponential multiserver queues," *Queueing Systems*, vol. 34, no. 1-4, pp. 169–181, 2000.

[5] National Institute for Health and Clinical Excellence, "Depression. management of depression in primary and secondary care," National Clinical Practice Guideline number 23, NICE, London, UK, 2004.

[6] National Institute for Health and Clinical Excellence, "Anxiety: management of anxiety (panic disorder, with or without agoraphobia, and generalised anxiety disorder) in adults in primary, secondary and community care," National Clinical Practice Guideline number 22, NICE, London, UK, 2004.

[7] D. A. Richards, P. Bower, and S. M. Gilbody, "Improving access to psychological therapies," in *Handbook of Primary Care Mental Health*, L. Gask, H. Lester, R. Peveler, and A. Kendrick, Eds., Gaskell, London, UK, 2009.

[8] M. B. Sobell and L. C. Sobell, "Stepped care as a heuristic approach to the treatment of alcohol problems," *Journal of Consulting and Clinical Psychology*, vol. 68, no. 4, pp. 573–579, 2000.

[9] M. G. Newman, "Recommendations for a cost-offset model of psychotherapy allocation using generalized anxiety disorder as an example," *Journal of Consulting and Clinical Psychology*, vol. 68, no. 4, pp. 549–555, 2000.

[10] S. Gallivan, M. Utley, C. Pagel, and D. Richards, "Applying operational research techniques to the reorganisation of mental health care in the UK," in *Operational Research Applied to Health Services in Action*, M. Lubicz, Ed., pp. 155–162, 2009.

[11] D. A. Richards, A. Weaver, M. Utley et al., "Developing evidence-based and acceptable stepped care systems in mental health care: an operational research project," Final Report, NIHR Service Delivery and Organisation Programme, 2010, http://www.sdo.nihr.ac.uk/projdetails.php?ref=08-1504-109.

[12] G. Weiss, "Jackson networks with unlimited supply of work," *Journal of Applied Probability*, vol. 42, no. 3, pp. 879–882, 2005.

[13] G. R. Grimmett and D. R., Stirzaker, *Probability and Random Processes*, Clarendon Press, Oxford, UK, 1992.

[14] "Microsoft webpage," http://office.microsoft.com/en-us/excel-help/introduction-to-optimization-with-the-excel-solver-tool-HA001124595.aspx.

Hindawi Publishing Corporation
Computational and Mathematical Methods in Medicine
Volume 2012, Article ID 212498, 8 pages
doi:10.1155/2012/212498

Research Article

Prediagnosis of Obstructive Sleep Apnea via Multiclass MTS

Chao-Ton Su,[1] Kun-Huang Chen,[1] Li-Fei Chen,[2] Pa-Chun Wang,[3,4,5] and Yu-Hsiang Hsiao[6]

[1] *Department of Industrial Engineering and Engineering Management, National Tsing Hua University, Hsinchu 30013, Taiwan*
[2] *MBA Program in International Management, Department of Business Administration, Fu Jen Catholic University, New Taipei City 24205, Taiwan*
[3] *Department of Otolaryngology, Cathay General Hospital, Taipei 10630, Taiwan*
[4] *Quality Management Center, Cathay General Hospital, Taipei 10630, Taiwan*
[5] *Fu Jen Catholic University, School of medicine, New Taipei City 24205, Taiwan*
[6] *Information and Communications Research Laboratories, Industrial Technology Research Institute, Hsinchu 31040, Taiwan*

Correspondence should be addressed to Chao-Ton Su, ctsu@mx.nthu.edu.tw

Received 6 September 2011; Revised 9 January 2012; Accepted 16 January 2012

Academic Editor: Philip Crooke

Obstructive sleep apnea (OSA) has become an important public health concern. Polysomnography (PSG) is traditionally considered an established and effective diagnostic tool providing information on the severity of OSA and the degree of sleep fragmentation. However, the numerous steps in the PSG test to diagnose OSA are costly and time consuming. This study aimed to apply the multiclass Mahalanobis-Taguchi system (MMTS) based on anthropometric information and questionnaire data to predict OSA. Implementation results showed that MMTS had an accuracy of 84.38% on the OSA prediction and achieved better performance compared to other approaches such as logistic regression, neural networks, support vector machine, C4.5 decision tree, and rough set. Therefore, MMTS can assist doctors in prediagnosis of OSA before running the PSG test, thereby enabling the more effective use of medical resources.

1. Introduction

According to the National Institutes of Health, 50–70 million Americans are affected by chronic sleep disorders and intermittent sleep problems that can significantly diminish health, alertness, and safety. Untreated sleep disorders have been linked to hypertension, heart disease, stroke, depression, diabetes, and other chronic diseases. Recently, the Institute of Medicine in its report estimated that sleep disorders and sleep deprivation constitute an inadequately addressed public health problem, and "hundreds of billions of dollars a year are spent on direct medical costs related to sleep disorders, such as doctor visits, hospital services, prescriptions, and over-the-counter medications." According to the National Highway Traffic Safety Administration, drowsy driving claims more than 1,500 lives and causes at least 100,000 motor vehicle crashes each year [1].

Polysomnography (PSG) is traditionally considered an established and effective diagnostic tool providing information on the severity of obstructive sleep apnea (OSA) and the degree of sleep fragmentation. However, the PSG method is time consuming and labor intensive [2, 3], requiring overnight evaluation in a sleep laboratory, dedicated systems, and attending personnel. Accurate identification of an apnea event requires the direct measurement of upper airway airflows and respiratory efforts. Therefore, the development of a simple and effective predictive method for OSA diagnosis is important.

There are many inspections for OSA methods, including the O_2 Pulse Oximeter, the body mass index (BMI), and the two-stage method (BMI-attached O_2 Pulse Oximeter and questionnaire-attached O_2 Pulse Oximeter). However, patients are still required to wear the O_2 Pulse Oximeter overnight, which is very inconvenient for them [4–6].

Mahalanobis-Taguchi System (MTS) is a collection of methods that was proposed as a forecasting and classification technique using multivariate data developed by Dr. Taguchi [7, 8]. MTS integrates Mahalanobis distance and Taguchi's robust engineering. Mahalanobis distance is used to construct a multidimensional measurement scale and to define

Table 1: The OSA attributes.

No.	Item.	Description
A	Gender	Gender (1, 2)[1]
B	Age	Years (0–100)
C	BW	Weight (Body weight, in kg)
D	BH	Height (body height, in cm)
E	BMI	Body Mass Index (body mass index, in kg/m^2)
F	SBP	Systolic blood pressure (mm Hg)
G	DBP	Diastolic blood pressure (mm Hg)
H	ESS	Daytime sleepiness survey scale (0–24, 24=worst daytime sleepiness situation)
I	SOS	Snoring survey score (0–100, 0=Worst snoring score)
J	DI3	Frequency of desaturation (saturation index <3% in an hour)
K	DI4	Frequency of desaturation (saturation index <4% in an hour)
L	PLM	Frequency of paroxysmal leg movement in an hour

[1] 1: Male, 2: Female.

a reference point of the scale with a set of observations from a reference group. Taguchi's robust engineering is applied to determine the important features and then optimize the system. Thus far, MTS has been successfully used in various applications [9–13].

Multiclass Mahalanobis-Taguchi system (MMTS) breaks the limitation of MTS, in which only one Mahalanobis space is constructed for one problem and establishes an individual Mahalanobis space for each class to accomplish multiclass classification and feature selection tasks simultaneously. MMTS also inherits the robustness of classification from MTS [13]. The classification capability and feature selection stability of MMTS were both confirmed [14].

Therefore, this study used MMTS for OSA prediction to provide a convenient and fast prediction method. A comparison was also made between MMTS and other methods, including logistic regression (LR), back propagation neural network (BPN), learning vector quantization (LVQ), support vector machine (SVM), C4.5 decision tree, and rough set (RS).

2. Materials and Methods

Following the approval from the Cathay General Hospital, Taipei, Taiwan, this study gathered 124 subjects (90 men and 34 women) who were referred for clinical suspicions of OSA from October 2007 to July 2008. The patients were consecutively recruited from the outpatient clinic and taken through data preprocessing to prepare for the training and the testing data sets. Inconsistent data were deleted, and missing values in the analysis were ignored, leaving 86 subjects (62 diseased and 24 nondiseased) for our analysis.

The collected OSA data had 12 attributes, including anthropomorphic measurements (i.e., age, gender, height, weight, body mass index (BMI)), systolic blood pressure (SBP), diastolic blood pressure (DBP), frequency of desaturation (DI3, DI4), frequency of paroxysmal leg movements per hour (PLM), and questionnaire measurements (ESS, SOS). The explanations for each attribute are presented in Table 1.

MMTS, which was developed by Su and Hsiao as a diagnostic and forecasting technique, uses multivariate data developed according to the MTS framework. It is used for simultaneous multiclass classification and feature selection. MMTS comprises four main implementation stages: construction of a full-model measurement scale with Mahalanobis space of each class as the reference; validation of the full-model measurement scale; feature selection; future prediction with important features.

2.1. Stage 1: Construction of a Full-Model Measurement Scale with Mahalanobis Space of Each Class as Reference. In this stage, the problem and all related features are defined, representative examples are collected to construct the individual Mahalanobis space for each class, and a full-model measurement scale is established. To enhance accuracy in constructing the measurement scale, the Gram-Schmidt orthogonalization process is applied to eliminate multicollinearity from among the features, making the covariance matrix almost singular and the inverse matrix invalid.

Assume that there are k classes in a d-dimensional space. For each class $C_i (i = 1, 2, \ldots, k)$, the examples sampled from its population are defined as "normal" while the examples coming from other $k - 1$ classes are defined as "abnormal." The Mahalanobis space MS_i is formed by the n_i normal examples sampled from C_i. $A^{(p)}_{1(i)}, A^{(p)}_{2(i)}, \ldots, A^{(p)}_{d(i)}$ denote the standardized feature vectors of MS_i standardized by the feature means and standard deviations of MS_p. The Gram-Schmidt feature vectors of MS_i orthogonalized on the basis of MS_p, that is, $U^{(p)}_{l(i)}$, are sequentially constructed from $l = 1$ to $l = d$ by the following Gram-Schmidt setting:

$$U^{(p)}_{l(i)} = A^{(p)}_{l(i)} - \sum_{q=1}^{l-1} t_{lq^{(p)}} \times U^{(p)}_{q^{(i)}}, \quad (1)$$

where $A_{l(i)}^{(p)}$ is the lth feature vector of MS_i standardized by MS_p, $U_{q^{(i)}}^{(p)}$ is the Gram-Schmidt vector of the qth feature of MS_i orthogonalized on the basis of MS_p, and $t_{lq^{(p)}}$ is the Gram-Schmidt coefficient of MS_p and is set as follows for $l = 1, 2, \ldots, d, q = 1, 2, \ldots, l-1$:

$$t_{lq^{(p)}} = \frac{A_{l^{(p)}}^{(p)^T} U_{q^{(p)}}^{(p)}}{U_{q^{(p)}}^{(p)^T} U_{q^{(p)}}^{(p)}}, \tag{2}$$

where $A_{l^{(p)}}^{(p)}$ is the lth standardized feature vector of MS_p and $U_{q^{(p)}}^{(p)}$ is the Gram-Schmidt vector of the qth feature of MS_p.

The Mahalanobis distance from any example r to C_i can be calculated using the Gram-Schmidt orthogonalization process as follows. First, the features in example r are standardized using the feature means and standard deviations of MS_i. Next, the Gram-Schmidt coefficients of MS_i are employed to perform the Gram-Schmidt orthogonalization process on the standardized features of example r. The Mahalanobis distance from example r to C_i, that is, $\mathrm{MD}_r^{(i)}$, using the Gram-Schmidt orthogonalization process is calculated as the following equation:

$$\mathrm{MD}_r^{(i)} = \frac{1}{d} \times \sum_{q=1}^{d} \frac{u_{rq}^{(i)^2}}{\zeta_{q^{(i)}}^2}, \tag{3}$$

where d is the number of features, $u_{rq}^{(i)}$ is the Gram-Schmidt vector of the qth feature in example r processed by MS_i, and $\zeta_{q^{(i)}}$ is the standard deviations of $U_{q^{(i)}}^{(p)}$ for $p = i$.

For the n_i normal examples in MS_i, their Mahalanobis distances are to C_i ($i = 1, 2, \ldots, k$) using the Gram-Schmidt orthogonalization process. With these Mahalanobis distances, the center point and the unit distance for each class can be defined, by which the reference base for the measurement scale is determined.

2.2. Stage 2: Validation of the Full-Model Measurement Scale. In this stage, the effectiveness of discrimination among different classes is validated through the full-model measurement scale. Therefore, the Mahalanobis distance to each Mahalanobis space is calculated for each example. The measurement scale is then validated by examining the reparability of the Mahalanobis distances corresponding to the examples with different classes.

For C_i, $i = 1, 2, \ldots, k$, the corresponding abnormal examples from the other $k-1$ classes are used to validate the measurement scale. To do so, the Mahalanobis distances from the abnormal examples to C_i should be computed using (3). According to the MTS theory, the Mahalanobis distances of abnormal examples will be much larger than those of normal examples if the measurement scale is good. However, for C_i, $i = 1, 2, \ldots, k$, if there is no significant difference between the normal and abnormal Mahalanobis distances, then the constructed Mahalanobis space cannot suitably represent the corresponding real normal condition. Moreover, we should return to the beginning of the whole problem and perform some checks on the completeness of considered features or on the representative of the collected examples used to construct Mahalanobis space.

2.3. Stage 3: Identification of the Important Features. In this stage, orthogonal arrays and signal-to-noise ratio are used to identify the important features for multiclass classification.

Each of the original d features is first set with two experiment levels. Level 1 includes the feature in constructing the Mahalanobis space while Level 2 excludes the feature. Afterward, an appropriate orthogonal array is chosen, and the d features are assigned into different columns of orthogonal array. Inside the orthogonal array, every row (run) presents a different level combination of features. For each run, the features with Level 1 are used to construct the Mahalanobis space for C_i, $i = 1, 2, \ldots, k$. In addition, the $\mathrm{MD}_{j^{(i)}}^{(p)}$ for $j = 1, 2, \ldots, n_i$, $i = 1, 2, \ldots, k$, and $p = 1, 2, \ldots, k$ are calculated according to (3) and are regarded as the output of each run. Thus, in each run, there will be n_i normal Mahalanobis distances and $\sum_{q=1}^{k} n_q$ abnormal Mahalanobis distances produced for C_i, where $q \neq i$. When an example r comes from MS_i, a high ratio $\mathrm{MD}_{r^{(i)}}^{(p\neq i)}/\mathrm{MD}_{r^{(i)}}^{(p=i)}$ is expected. For this reason, the signal-to-noise ratio η corresponding to each run of orthogonal array is computed using the concept of the larger-the-better type and is defined using the following equation:

$$\eta = \sum_{i,p=1}^{k} \left[-10 \times \log_{10} \left(\frac{1}{n_i} \times \sum_{j=1}^{n_i} \left(\frac{\mathrm{MD}_{j^{(i)}}^{(p\neq i)}}{\mathrm{MD}_{j^{(i)}}^{(p=i)}} \right)^{-1} \right) \right] = \sum_{i,j=1}^{k} \eta_{ip}, \tag{4}$$

where n_i is the number of examples in the Mahalanobis space MS_i; $\mathrm{MD}_{j^{(i)}}^{(p=i)}$ is the Mahalanobis distance from the jth example in MS_i to class C_p and $p = i$; and $\mathrm{MD}_{j^{(i)}}^{(p\neq i)}$ is the Mahalanobis distance from the jth example in MS_i to class C_p and $p \neq i$.

For the lth feature, $\overline{\mathrm{SN}_l^+}$ is used to represent the average signal-to-noise ratio of all runs including the feature, whereas $\overline{\mathrm{SN}_l^-}$ represents the average signal-to-noise ratio of all runs excluding the feature. Independently evaluating the effect of each main factor is allowable because orthogonal arrays are used. Thus, the "effect gain" of each feature can be directly calculated using the following equation:

$$\mathrm{Gain}_l = \overline{\mathrm{SN}_l^+} - \overline{\mathrm{SN}_l^-}. \tag{5}$$

If the effect gain corresponding to a feature is positive, the feature may be important and may be considered as worth keeping. However, a feature with negative effect gain should be removed.

2.4. Stage 4: Future Prediction with Important Features. In this final stage, a reduced model measurement scale is constructed using the important features and then validated. A "weighted Mahalanobis distance" is employed to be the

distance metric for classification. By simply classifying examples into the class with the minimum weighted Mahalanobis distance, the classification can be achieved.

The measurement scale is reconstructed using the feature subset R composed of δ important features identified in the third stage. This scale is called the "reduced model measurement scale." Similarly, for MS_i, $i = 1, 2, \ldots, k$, the validations of the scale should be applied using the corresponding abnormal examples to ensure that this reduced model has a good ability to discriminate among different classes. The weighted Mahalanobis distance weighing the different features in the Mahalanobis distance according to the corresponding effect gains obtained in the third stage is used for classification after the reduced model measurement scale is validated. The weighted Mahalanobis distance from any example r to C_i is computed through the following equation:

$$\mathrm{WMD}_r^{(i)} = \frac{1}{\delta} \times \sum_{l \in R} w_l \times \frac{u_{rl}^{(i)^2}}{\zeta_{l(i)}^2}, \tag{6}$$

where δ is the number of features in the reduced model, w_l is the weight of the lth feature in the reduced model, $u_{rl}^{(i)}$ is the Gram-Schmidt vector of the lth feature of example r processed by MS_i in the reduced model, and $\zeta_{l(i)}$ is the standard deviations of $U_{l^{(i)}}^{(p)}$ in the reduced model for $p = i$.

The weight of the lth feature, that is, w_l, in the reduced model can be acquired by normalizing the corresponding effect gain obtained in the third stage as

$$w_l = \frac{\mathrm{Gain}_l}{\sum_{l \in R} \mathrm{Gain}_l}, \tag{7}$$

where Gain_l is the effect gain of the lth feature in the reduced model.

Based on this reduced model, a classification can be achieved by simply classifying examples into the class with minimum weighted Mahalanobis distance, and thus, the classification accuracy can be acquired. Importantly, a test experiment should be implemented using the unknown examples to confirm the classification ability of the reduced model.

Note that the validation stage (Stage 2) plays an important role in MMTS algorithm. Stage 2 aims to check if the measurement scale is constructed well. That is, it is used to ensure that the measurement scale has the basic ability to discriminate the examples used to construct the Mahalanobis space and the examples out of the space. A valid measurement scale also implies that the important features of a problem have been considered and the representative examples have been collected for analysis. A comprehensive feature set and representative examples are prerequisites for establishing a good MMTS model. Moreover, Stage 3 of MMTS, the feature selection stage, is meaningless if valuable features are not considered and included at the beginning of problem analysis. Thus, the validation stage is also a way for checking the completeness of features and the representation of collected examples, and it is needed for ensuring the quality of the established MMTS model (Figure 1).

The four stages of implementing MMTS are shown in Figure 1. For details on MMTS, refer to Su and Hsiao [14].

3. Implementation

PSG, a multiparametric test used in sleep medicine, provides reliable data on OSA through comprehensive recordings of biophysiological changes that occur during sleep. It involves the following data: electroencephalogram (EEG), electrooculogram (EOG), electromyogram (EMG), heartbeat, and oximeter of the lobe. Scoring is accomplished through the Rechtschaffen method, which grades the severity of sleep apnea by the number of events per hour and is reported as a respiratory disturbance index (RDI). Patients were placed into four groups: the group with an RDI value <5 is normal; 5–15 is mild; 15–30 is moderate; >30 events per hour is characterized as having severe sleep apnea. In this study, MMTS was employed in the classification of OSA patterns.

To illustrate the effectiveness of MMTS for OSA prediction, comparisons were made between MMTS and other methods, including LR, BPN, LVQ, SVM, C4.5 decision tree, and RS. LR was first established as an analytical tool in epidemiology. It is used extensively in the medical and social sciences and has become the accepted "standard" in various research areas.

Artificial neural networks (ANNs) are computer programs modeled after the biological nervous system and are capable of recognizing complex patterns in data based on experience. These programs have been demonstrated as promising classification tools because their learning ability allows them to determine optimumn onlinear relationships between classes and to feature patterns from data sets. Both BPN and LVQ are common types of ANNs. On the other hand, SVMs have been successfully applied to classification and regression problems such as character recognition developed by Su and Hsiao [15]. A decision tree is a decision support tool that uses a tree-like graph or model of decisions and their possible consequences, including chance event outcomes, resource costs, and utility. The decision tree is the most efficient approach to addressing classification issues. The RS theory was introduced by Pawlak and is a mathematical tool. This theory provides a tool to mine knowledge as decision rules from a database or web-based information among others [16].

In this comparison, SVM was implemented using LIBSVM, which provides an efficient parameter selection tool using cross-validation through a parallel grid search performed under the kernel of the radial basis function type. Both BPN and LVQ are ANN models constructed for this study using the Professional II PLUS software. The parameters of BPN and LVQ contain the learning rate, momentum, and number of hidden nodes, which were optimized through trial and error to determine the combinations of the minimum root mean square errors. All the results of the C4.5 decision tree in this comparison were operated using the software tool see [17]. Finally, RSES and Weka software were used to implement RS and LR for classification problems, respectively. Statistical analysis was

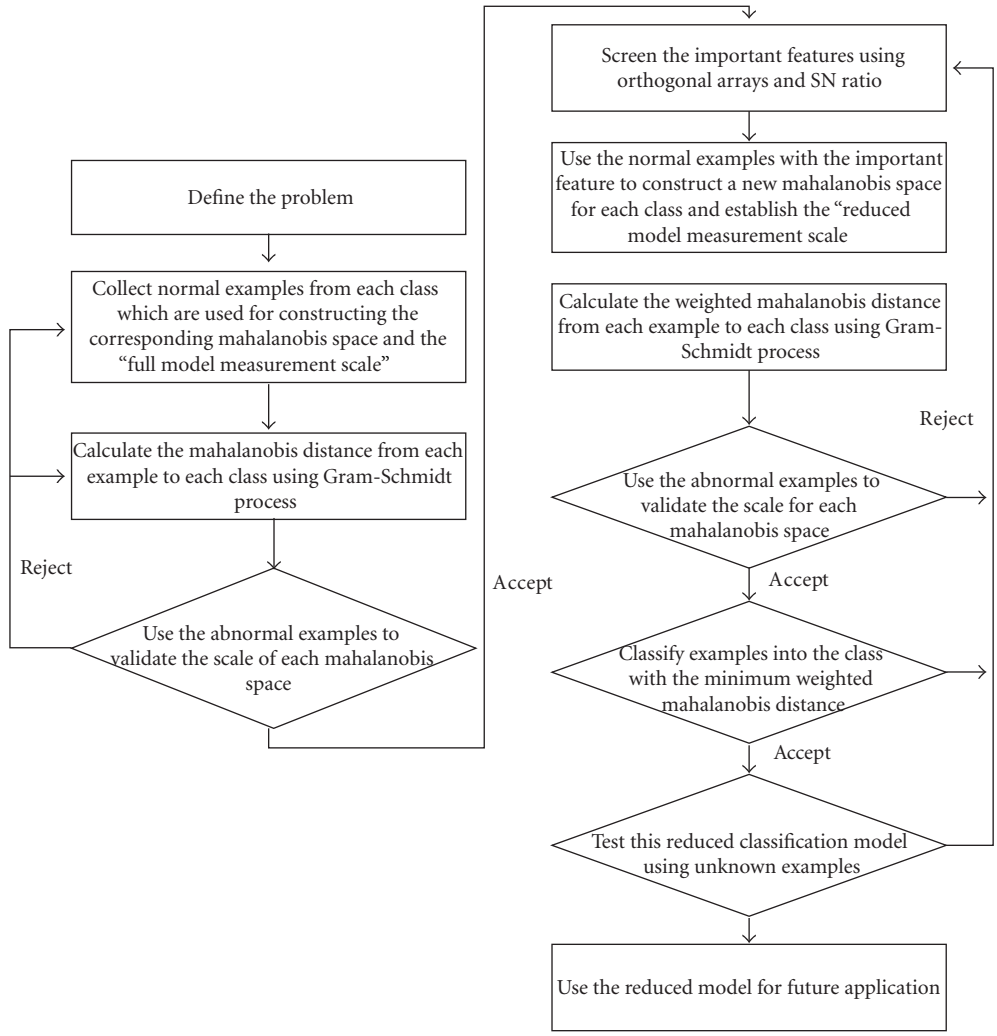

Figure 1: Procedure of implementing MMTS.

performed using SPSS v.14.0 (Statistical Package for Social Science, Chicago, IL).

4. Results

The subjects, including 66 men and 20 women, ranged in age from 11 to 78 years, with a mean age of 48.3 years (±11.87). Mean height was 165.97 (±7.34) mean weight was 69.05 (±11.31); mean BMI was 24.98 kg/m^2 (±3.13); mean SBP was 124.64 (±17.62); mean DBP was 81.23 (±10.46), mean ESS score was 10.07 (±6.38) mean SOS score was 50.23 (±21.20), mean DI3 was 92.76 (±121.66), mean DI4 was 92.47 (±121.70); and mean PLM was 2.72 (±8.68). These results are summarized in Table 2.

This study separated the collected OSA data into two parts: Group I and Group II (Table 3). Group I was used to establish the model, whereas Group II was used to test the developed model. In the classification performance, the average classification rate of OSA obtained by each algorithm of Group II is shown in Table 4.

Table 4 shows the test results of the OSA data set. The obtained average accuracies of MMTS, LR, BPN, LVQ, SVM, C4.5 decision tree, and RS were 84.38%, 55.33%, 34.04%, 47.22%, 53.82%, 63.54%, and 13.20%, respectively. Results showed that MMTS had an accuracy of 84.38% on the OSA prediction, outperforming the other methods. Therefore, MMTS can be applied to assist doctors in foreseeing an OSA diagnosis before running the PSG test, thereby allowing a more effective use of medical resources.

5. Discussion

5.1. OSA. In this study, six important features, including age, weight, SBP, DBP, DI3, and DI4, are identified using MMTS. The other features not selected using MMTS include gender, height, BMI, ESS, SOS, and PLM. The following section briefly discusses these selected features.

Patients were placed into four groups: the group with an RDI value <5 is normal; 5–15 is mild; 15–30 is moderate; and >30 events per hour is characterized as having severe sleep apnea [18]. For the RDI value, higher is worse, lower is better.

Table 2: Demographic data, $N = 86$.

	Mean	Median	SD[1]	Range
Gender	1.23	1	0.42	1-2
Age	48.3	49	11.87	11–78
height	165.98	167	7.34	151–184
weight	69.04	68	11.31	49–116
BMI	24.98	24.78	2.13	18.34–34.26
SBP	124.64	122.5	17.62	83–178
DBP	81.23	81	10.46	53–108
ESS	10.07	11	6.38	0–24
SOS	50.23	46	21.20	18–95
DI3	92.76	37.5	121.66	0–550
DI4	92.47	36	121.70	0–550
PLM	2.72	0	8.68	0–47.1

[1] SD: Standard Deviation.

Table 3: The OSA data.

	Nondisease (normal)	Disease (mild)	Disease (moderate)	Disease (severe)	Total
Group I (training data)	16	23	10	8	57
Group II (testing data)	8	6	9	6	29

In most studies, the age index is often used in the prediction model of OSA disease [19, 20]. OSA has two possible underlying causes: an anatomically vulnerable airway and neurologically unstable breathing control. As people grow older, their ability to control force in their airway weakens, thereby worsening their breathing. Thus, age is influential both neurologically and in the airway. This study found that hemodynamic parameters such as DBP, and SBP were more relevant to the development of OSA. For the Age, DBP and SBP, higher is worse, lower is better.

The ID3 and ID4 indices are the frequencies of desaturation (index <3% in an hour and index <4% in an hour, resp.). These indices can explain why there is more severe desaturation than the one predicted in alveolar hypoventilation, as demonstrated in OSA patients [4, 5]. In other words, oxygen desaturation occurs more often in proportion to the frequency of respiratory disturbances in OSA subjects [21].

Both SOS and ESS are the questionnaires that help decide whether a patient has a sleep problem. ESS measures daytime sleepiness and is often used clinically to screen for manifestations of behavioral morbidity associated with OSA [22]. SOS, in comparison, is another recently described questionnaire for evaluating patients with snoring problems. Although SOS is a subjective instrument, it is valid, reliable, and sensitive to clinical changes [23]. These questionnaires are effective in determining whether a patient has OSA problems; however, they are not helpful in determining the severity of sleep apnea. All patients were administered with the Chinese versions of SOS and ESS as the laboratory test routine. All surveys were validated and considered statistically equivalent to their original English versions [24, 25]. For ESS range 0–24, higher is worse. For SOS 0–100, higher is better.

Gender as a factor has only been recognized recently. Several studies have tried to provide an explanation for the male predominance in OSA, including differences in anatomical size, greater collapsibility of the upper airway, greater increase in upper airway resistance in men, and hormonal changes in women [17, 26]. However, gender is not helpful in determining the severity of sleep apnea.

BMI is a statistical measurement that compares weight and height. It is considered a useful index to estimate the body's level of obesity. Obesity is often seen in OSA patients, yet, in experimental results, BMI is not an important feature. The reason is that BMI is routinely used in PSG lab; therefore we checked this feature. However, our data show there is poor correlation between BMI and OSA severity; as a result, BMI is not included in the MMTS model to predict OSA.

PLM represents the frequency of paroxysmal leg movements per hour during night sleep and indicates the severity of sleep disturbance caused by this particular disease. A higher PLM contributes to worse situation.

5.2. Methods. To illustrate the effectiveness of MMTS for OSA prediction, comparisons were made between MMTS and other methods, including LR, BPN, LVQ, SVM, C4.5 decision tree, and RS. The observation made on the MMTS is significantly better than that of other classifications of algorithms. On the other hand, from the viewpoint of implementation, MMTS does not require any parameters to optimize its execution, whereas other techniques such as BPN and SVM consume much time in fine-tuning the parameters. The performance of these parameter-attached classification or feature selection techniques is always sensitive to the parameter determination. Effectively determining the best combination of parameter settings to optimize algorithm output remains a pending issue.

Table 4: A comparison.

Method	Selected attributes	Pattern	Accuracy (%)	
MMTS	Age, weight, SBP, DBP, DI3 DI4	normal	87.5%	Average
		mild	66.67%	
		moderate	100%	84.38%
		severe	83.33%	
Logistic Regression	Gender, age, height, weight, BMI, SBP, DBP, ESS, SOS, DI3, DI4, PLM	normal	50.00%	55.33%
		mild	50.00%	
		moderate	33.33%	
		severe	100.00%	
BPN	Gender, age, height, weight, BMI, SBP, DBP, ESS, SOS, DI3, DI4, PLM	normal	25.00%	34.04%
		mild	33.33%	
		moderate	11.11%	
		severe	66.70%	
LVQ	Gender, age, height, weight, BMI, SBP, DBP, ESS, SOS, DI3, DI4, PLM	normal	50.00%	47.22%
		mild	16.67%	
		moderate	22.22%	
		severe	100.00%	
SVM	Age, height, weight, BMI, SBP, DBP, ESS, SOS, DI3, DI4, PLM	normal	37.50%	53.82%
		mild	66.67%	
		moderate	11.11%	
		severe	100.00%	
C4.5	Age, weight, BMI, SBP, SOS, DI4	normal	37.50%	63.54%
		mild	50.00%	
		moderate	66.67%	
		severe	100.00%	
RS	Gender, Age, weight, SBP, ESS, SOS	normal	25.00%	13.20%
		mild	16.67%	
		moderate	11.11%	
		severe	0.00%	

6. Conclusions

In recent years, OSA has become an important public health concern. A complete and thorough sleep checkup has to be conducted in a sleep laboratory or medical center, and the patient has to undergo the PSG test in a particular bed for the entire night. Various sensory devices are used on the patient to monitor overnight physical conditions, allowing the complete sleeping structure to be observed and any unusual sleeping condition to be detected. Doctors use the information obtained as the basis for diagnosis. The numerous steps in the PSG test to diagnose OSA are thus costly and time consuming. In this study which applies MMTS, the patient simply needs to wear the monitoring systems (e.g., oximeter) around the wrist like a watch and conduct an at-home overnight test. The monitoring systems are connected to a sensor wire clip placed on a fingertip. The obtained data are used in MMTS to anticipate the OSA diagnosis. Therefore, because it is extremely simple and convenient, this method can be useful for doctors in predicting an OSA diagnosis in advance before running the PSG test, allowing for a more effective use of medical resources.

References

[1] National Sleep Foundation, http://www.sleepfoundation.org/.

[2] S. D. Kirby, W. Danter, C. F. P. George, T. Francovic, R. R. F. Ruby, and K. A. Ferguson, "Neural network prediction of obstructive sleep apnea from clinical criteria," *Chest*, vol. 116, no. 2, pp. 409–415, 1999.

[3] S. K. Sharma, S. Kurian, V. Malik et al., "A stepped approach for prediction of obstructive sleep apnea in overtly asymptomatic obese subjects: a hospital based study," *Sleep Medicine*, vol. 5, no. 4, pp. 351–357, 2004.

[4] I. Gurubhagavatula, G. Maislin, and A. I. Pack, "An algorithm to stratify sleep apnea risk in a sleep disorders clinic population," *American Journal of Respiratory and Critical Care Medicine*, vol. 164, no. 10 I, pp. 1904–1909, 2001.

[5] S. V. Jacob, A. Morielli, M. A. Mograss, F. M. Ducharme, M. D. Schloss, and R. T. Brouillette, "Home testing for pediatric obstructive sleep apnea syndrome secondary to adenotonsillar hypertrophy," *Pediatric pulmonology*, vol. 20, no. 4, pp. 241–252, 1995.

[6] Y. Yamashiro and M. H. Kryger, "Nocturnal oximetry: is it a screening tool for sleep disorders?" *Sleep*, vol. 18, no. 3, pp. 167–171, 1995.

[7] G. Taguchi, S. Chowdhury, and Y. Wu, *The Mahalanobis-Taguchi System*, McGraw-Hill, 2001.
[8] G. Taguchi and R. Jugulum, *The Mahalanobis-Taguchi Strategy*, Wiley, New York, NY, USA, 2002.
[9] J. Srinivasaraghavan and V. Allada, "Application of mahalanobis distance as a lean assessment metric," *International Journal of Advanced Manufacturing Technology*, vol. 29, no. 11-12, pp. 1159–1168, 2006.
[10] T. Riho, A. Suzuki, J. Oro, K. Ohmi, and H. Tanaka, "The yield enhancement methodology for invisible defects using the MTS+ method," *IEEE Transactions on Semiconductor Manufacturing*, vol. 18, no. 4, pp. 561–568, 2005.
[11] P. Das and S. Datta, "Exploring the effects of chemical composition in hot rolled steel product using Mahalanobis distance scale under Mahalanobis-Taguchi system," *Computational Materials Science*, vol. 38, no. 4, pp. 671–677, 2007.
[12] G. Taguchi, S. Chowdhury, and Y. Wu, *Taguchi's Quality Engineering Handbook*, Wiley, 2005.
[13] C. T. Su and Y. H. Hsiao, "An evaluation of the robustness of MTS for imbalanced data," *IEEE Transactions on Knowledge and Data Engineering*, vol. 19, no. 10, pp. 1321–1332, 2007.
[14] C. T. Su and Y. H. Hsiao, "Multiclass MTS for simultaneous feature selection and classification," *IEEE Transactions on Knowledge and Data Engineering*, vol. 21, no. 2, pp. 192–205, 2009.
[15] M. Brown, S. R. Gunn, and H. G. Lewis, "Support vector machines for optimal classification and spectral unmixing," *Ecological Modelling*, vol. 120, no. 2-3, pp. 167–179, 1999.
[16] Y. Matsumoto and J. Watada, "Knowledge acquisition from time series data through rough sets analysis," *International Journal of Innovative Computing, Information and Control*, vol. 5, no. 12, pp. 4885–4897, 2009.
[17] F. Kapsimalis and M. H. Kryger, "Gender and obstructive sleep apnea syndrome—part 2: mechanisms," *Sleep*, vol. 25, no. 5, pp. 499–506, 2002.
[18] M. Hirshkowitz and M. H. Kryger, "Monitoring techniques for evaluating suspected sleep-disordered breathing," in *Principle and Practice of Sleep Medicine*, M. H. Kryger, T. Roth, and W. C. Dement, Eds., pp. 1378–1379, Elsevier, Philadelphia, Pa, USA, 4th edition, 2005.
[19] J. B. Dixon, L. M. Schachter, and P. E. O'Brien, "Predicting sleep apnea and excessive day sleepiness in the severely obese: indicators for polysomnography," *Chest*, vol. 123, no. 4, pp. 1134–1141, 2003.
[20] S. K. Sharma, V. Malik, C. Vasudev et al., "Prediction of obstructive sleep apnea in patients presenting to a tertiary care center," *Sleep and Breathing*, vol. 10, no. 3, pp. 147–154, 2006.
[21] H. Schäfer, S. Ewig, E. Hasper, and B. Lüderitz, "Predictive diagnostic value of clinical assessment and nonlaboratory monitoring system recordings in patients with symptoms suggestive of obstructive sleep apnea syndrome," *Respiration*, vol. 64, no. 3, pp. 194–199, 1997.
[22] L. D. Rosenthal and D. C. Dolan, "The Epworth sleepiness scale in the identification of obstructive sleep apnea," *Journal of Nervous and Mental Disease*, vol. 196, no. 5, pp. 429–431, 2008.
[23] R. E. Gliklich and P. C. Wang, "Validation of the snore outcomes survey for patients with sleep-disordered breathing," *Archives of Otolaryngology*, vol. 128, no. 7, pp. 819–824, 2002.
[24] N. H. Chen, H. Y. Li, R. E. Gliklich, C. C. Chu, S. C. Liang, and P. C. Wang, "Validation assessment of the Chinese version of the Snore Outcomes Survey," *Quality of Life Research*, vol. 11, no. 6, pp. 601–607, 2002.
[25] N. H. Chen, M. W. Johns, H. Y. Li et al., "Validation of a Chinese version of the Epworth sleepiness scale," *Quality of Life Research*, vol. 11, no. 8, pp. 817–821, 2002.
[26] M. R. Shepertycky, K. Banno, and M. H. Kryger, "Differences between men and women in the clinical presentation of patients diagnosed with obstructive sleep apnea syndrome," *Sleep*, vol. 28, no. 3, pp. 309–314, 2005.

Hindawi Publishing Corporation
Computational and Mathematical Methods in Medicine
Volume 2012, Article ID 829465, 5 pages
doi:10.1155/2012/829465

Research Article

Risk-Adjusted Mortality: Problems and Possibilities

Daniel Shine

Department of Medicine, NYU Langone Medical Center, 550 First Avenue, New York, NY 10016, USA

Correspondence should be addressed to Daniel Shine, daniel.shine@nyumc.org

Received 29 July 2011; Revised 24 December 2011; Accepted 3 January 2012

Academic Editor: John Hotchkiss

The ratio of observed-to-expected deaths is considered a measure of hospital quality and for this reason will soon become a basis for payment. However, there are drivers of that metric more potent than quality: most important are medical documentation and patient acuity. If hositals underdocument and therefore do not capture the full "expected mortality" they may be tempted to lower their observed/expected ratio by reducing "observed mortality" through limiting access to the very ill. Underdocumentation occurs because hospitals do not recognize, and therefore cannot seek to confirm, specific comorbidities conferring high mortality risk. To help hospitals identify these comorbidities, this paper describes an easily implemented spread-sheet for evaluating comorbid conditions associated, in any particular hospital, with each discharge. This method identifies comorbidities that increase in frequency as mortality risk increases within each diagnostic grouping. The method is inductive and therefore independent of any particular risk-adjustment technique.

1. Introduction

Risk of death in a hospitalized patient—and therefore the number of deaths expected in a hospital—is usually calculated using demographic and coded diagnostic and procedural information. A variety of private companies, trade organizations, and government agencies have developed mathematical models for calculating expected mortality; most of them employ roughly the same data set and use similar techniques of logistic regression [1–6]. The ratio between actual and expected deaths is widely considered to reflect quality of care, and as hospital performance data circulate ever more widely on the internet, this ratio has become a metric of increasing prominence [7, 8].

Soon risk-adjusted mortality will be of importance also to hospital revenue. Last year, the Center for Medicare and Medicaid Services (CMS) announced plans to withhold from each hospital a percentage of payments derived from diagnosis-related groupings (DRGs). These funds will be kept in a national pool and redistributed using indicators of quality and patient satisfaction chosen by CMS. A hospital may lose all of its withheld payments or receive well over twice the amount withheld. Observed-to-expected mortality in three DRGs is scheduled in 2014 to become one of the factors determining the percentage returned [9].

As hospitals attempt to maximize payment, they will take straightforward steps to increase compliance with those processes identified by CMS as quality related. They will also create initiatives to improve patient satisfaction. However, it is more difficult to conceive what specific measures a hospital might employ to decrease observed-to-expected mortality overall. With an important financial stake but no available strategy to protect that stake, hospitals will approach observed-to-expected mortality with concern.

To patients as well as insurance companies, there is undeniable appeal in a metric that purports to compare life-saving prowess between hospitals. Many will want to choose a hospital based perhaps largely on such a metric. It is therefore important both to make certain that the metric is fairly applied and to understand the limits on our ability to identify institutions that prevent death.

1.1. Observed Deaths. Observed deaths, the numerator, are usually an unavoidable result of end-stage or sudden and overwhelming illness. These deaths, and not the relatively few cases for which quality issues are determinative, mainly populate the numerator of observed/expected mortality. Because marginally preventable deaths are relatively uncommon, numerator variations tend to be more responsive to the acuity of a hospital's patients than to the quality of its

care. Every patient who dies increases numerator more than denominator because expectation of death is never 100%. The inevitable effect of increasing acuity is therefore an unwanted increase in the ratio. On the other hand, surviving low-acuity patients always increase denominator more than numerator because expectation of death is never 0%. The result is a desirable decrease in the ratio.

Enhancing quality of care is of course the intended strategy—improving observed/expected mortality by decreasing the "observed" numerator selectively among those patients whose survival is problematic but within reach. These are a small minority of numerator cases, however, while lowering institutional acuity broadly improves both numerator and denominator. Lower acuity also decreases the number of extremely long-stay patients, perhaps the most important driver of another closely watched hospital parameter, average length of stay.

Avoiding very ill patients or transferring them before they die may be mathematically a more effective way to decrease mortality ratio and practically easier to implement than a quality improvement effort with no very clear focus. The use of observed/expected mortality as a quality marker and a reimbursement multiplier may, therefore, threaten to limit hospital access for the very ill.

1.2. Expected Deaths. Not only institutional acuity but also choice of risk adjustment paradigm influences the denominator ("expected deaths"). Current methods of risk adjustment have been shown to predict death with variable accuracy and to disagree with each other substantially and often [10–12].

Variability in these calculations of mortality risk arises from the intrinsic difficulty in assessing severity of the principal diagnosis itself, particularly using administrative data that lack clinical detail. ICD-9 disease categories underlying all risk adjustment capture subtle differences in etiology but characterize severity less well, mainly by appending comorbidities. Yet severity of the principal diagnosis is of the first importance in predicting death, and mortality is also influenced by demographic and psychosocial factors, such as access to care and treatment setting [13, 14]. Like disease severity, the effect of these factors is not well captured by ICD-9.

Describing interactions among the intrinsic severity of a principal diagnosis, psychosocial factors, and the large number of possible comorbid conditions is the major mathematical problem of risk adjustment. Opportunities are many for excluding important variables and associations, for under- and overfitting, and for model instability due to variable colinearity. Inclusion of late-occurring, virtually death-defining diagnoses (asystole or cardiac arrest, e.g.,) as predictors of death can artificially enhance the apparent predictive power of risk adjustment models.

An important additional reason for poor model precision is that documentation practices vary among hospitals. Those with "sicker" patients have been shown to be often overcoded [15]. Equally problematic is the observation that patients who die tend as a group to be undercoded [16]. Whether extracted during record review or sent to databases automatically after coding, comorbid diagnoses are derived from documentation in the medical record; it is their assigned weights that largely determine expected risk of death in most adjustment methodologies. Both over-and undercoding can lead, therefore, to inaccurate risk assessment. Perhaps the most important kind of overcoding is failure to distinguish between complications and comorbidities [17]. CMS now requires hospitals to designate comorbidities that were present on admission (POA); however, compliance with this requirement is not complete even when a POA determination is easily made. The result can be risk adjustment that "charges" to the patient medical conditions actually caused by the hospital, resulting in overestimation of expected mortality [18, 19].

Undercoding arises from a failure to document or code those few comorbidities within each diagnostic grouping that specify a substantially increased risk of death. Within any risk-adjustment model, each comorbidity has a coefficient relating that comorbidity to the likelihood of death only in a particular DRG (or other grouping) and often only in the company of other particular comorbidities, but that coefficient is rarely large. Clinicians and coders cannot easily pick out these large-coefficient comorbidities because there are too many combinations of risk level, grouping, and comorbidity to keep track of. In addition, the majority of institutions purchase risk adjustment services that are proprietary; the general logic of their method is available, but specific determinants of risk are usually not.

A hospital, therefore, may not easily identify characteristic comorbidities that contribute heavily to risk in that particular hospital's common clinical groupings. It is desirable to find the comorbid conditions most relevant to risk of death for any particular illness and using any risk-adjustment method. Also useful to individual hospitals would be a more general list of those conditions that often contribute to local mortality risk in a range of locally common illnesses.

2. Methods

2.1. Data Sources. We approached this problem using a simple spreadsheet applied to our risk-adjusted data in two different risk adjustment methodologies, 3M (St. Paul, MN) and University Healthcare Consortium (UHC, Chicago IL).

Downloads came from our decision support system (McKesson HBOC, San Francisco, CA) for the 3M method and from UHC. The Institutional Review Board approved this approach and waived the requirement for individual patient consent in analyzing this deidentified patient data.

2.2. Data Manipulations. Risk adjustment data from these sources were downloaded onto separate Excel spreadsheets (Microsoft, Redmond, WA). Spreadsheet manipulation was divided into two phases: first, counting the number of instances of each comorbidity in each clinical grouping (APRDRG for 3M or base MSDRG for UHC) and second, identifying in each clinical grouping those comorbidities whose prevalence increased markedly between contiguous

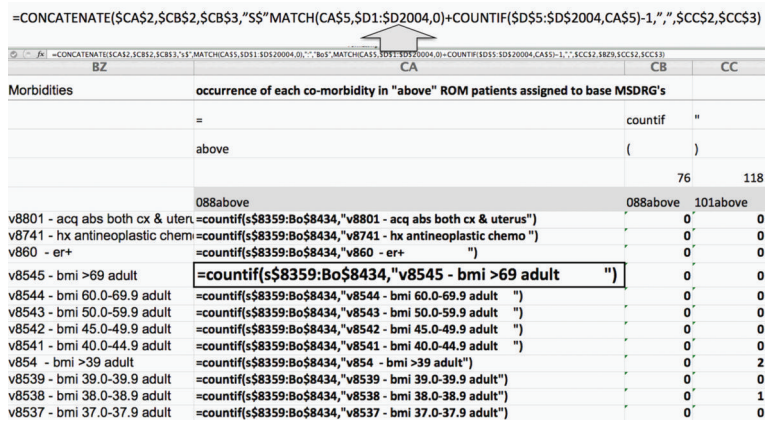

Figure 1: Organization of the right side of the UHC risk level "above" spreadsheet to count occurrences of comorbidities in each of the 100 commonest base MSDRGs.

	M	N	O	P	Q	R	S	T	U	V	W	X
1		1	2	3	4							
2	Co-morbidities	Prevalence of Comorbidity in risk group "well below"	Prevalence of Comorbidity in risk group "below"	Prevalence of Comorbidity in risk group "above"	Prevalence of Comorbidity in risk group "well above"	Slope well below to well above	Slope well below to below	Slope below to above	Slope above to well above	Slope well below to above	Slope below to well above	Co-morbidities in Descending Order
3	v8801 - acq abs both cx & uteri	0.0042224	0.0022148	0.0005959	0	-0.001	-0.002	-0.002	-0.001	-0.002	-0.001	4280 - chf nos
4	v8741 - hx antineoplastic chem	0	0.0001846	0.0005959	0	0.000	0.000	0.000	-0.001	0.000	0.000	5849 - acute kidney failure nos
5	v860 - er+	0	0	0	0	0.000	0.000	0.000	0.000	0.000	0.000	42731 - atrial fibrillation
6	v8545 - bmi >69 adult	0.0007037	0.0003691	0	0	0.000	0.000	0.000	0.000	0.000	0.000	2761 - hyposmolality
7	v8544 - bmi 60.0-69.9 adult	0	0.0007383	0	0	0.000	0.001	-0.001	0.000	0.000	0.000	40390 - htn ckd nos i-iv/nos
8	v8543 - bmi 50.0-59.9 adult	0.0021112	0.0003691	0	0	-0.001	-0.002	0.000	0.000	-0.001	0.000	v667 - palliative care
9	v8542 - bmi 45.0-49.9 adult	0	0.0007383	0.0005959	0.00543478	0.002	0.001	0.000	0.005	0.000	0.002	5119 - pleural effusion nos
10	v8541 - bmi 40.0-44.9 adult	0.0035186	0.0018457	0.0059595	0.01358696	0.003	-0.002	0.004	0.008	0.001	0.006	51881 - ac respiratory failure
11	v854 - bmi >39 adult	0.0154821	0.0107051	0.0047676	0.00815217	-0.003	-0.005	-0.008	0.003	-0.005	-0.001	5990 - urinary tract inf nos
12	v8539 - bmi 39.0-39.9 adult	0.0028149	0.0011074	0.0005959	0	-0.001	-0.002	-0.001	-0.001	-0.001	-0.001	2768 - hypopotassemia
13	v8538 - bmi 38.0-38.9 adult	0	0.0009228	0.0029797	0.00271739	0.001	0.001	0.002	0.000	0.001	0.001	5180 - pulmonary collapse
14	v8537 - bmi 37.0-37.9 adult	0.0014075	0.0007383	0.0005959	0	0.000	-0.001	0.000	-0.001	0.000	0.000	27651 - dehydration
15	v8536 - bmi 36.0-36.9 adult	0.0007037	0.0018457	0.0005959	0.00271739	0.000	0.001	-0.001	0.002	0.000	0.000	486 - pneumonia organism nos
16	v8535 - bmi 35.0-35.9 adult	0.0014075	0.001292	0.0005959	0	0.000	0.000	-0.001	-0.001	0.000	-0.001	2762 - acidosis
17	v8534 - bmi 34.0-34.9 adult	0.0014075	0.0011074	0.0023838	0	0.000	0.000	0.001	-0.002	0.000	-0.001	2767 - hyperpotassemia
18	v8533 - bmi 33.0-33.9 adult	0.0007037	0.0022148	0	0	0.000	0.002	-0.002	0.000	0.000	-0.001	1985 - secondary bone ca
19	v8532 - bmi 32.0-32.9 adult	0.0014075	0.0014766	0	0.01086957	0.003	0.000	-0.001	0.011	-0.001	0.005	2449 - hypothyroidism nos
20	v8531 - bmi 31.0-31.9 adult	0.0021112	0.0009228	0.0023838	0	0.000	-0.001	0.001	-0.002	0.000	0.000	41401 - cor as-native vessel
21	v8530 - bmi 30.0-30.9 adult	0.0007037	0.002584	0.0011919	0	0.000	0.002	-0.001	-0.001	0.000	-0.001	2859 - anemia nos
22	v8525 - bmi 29.0-29.9 adult	0	0.0009228	0.0011919	0.00543478	0.002	0.001	0.000	0.004	0.001	0.002	v850 - bmi <19 adult
23	v8524 - bmi 28.0-28.9 adult	0.0014075	0.0011074	0.0047676	0.00271739	0.001	0.000	0.004	-0.002	0.002	0.001	2875 - thrombocytopenia nos
24	v8523 - bmi 27.0-27.9 adult	0.0021112	0.0020303	0.0071514	0.01358696	0.004	0.000	0.005	0.006	0.003	0.006	5859 - chronic kidney dis nos
25	v8522 - bmi 26.0-26.9 adult	0.0021112	0.0014766	0.0035757	0	0.000	-0.001	0.002	-0.004	0.001	-0.001	e8497 - acc in residential inst
26	v8521 - bmi 25.0-25.9 adult	0.0007037	0.0022148	0.0017878	0.01086957	0.003	0.002	0.000	0.009	0.001	0.004	1977 - secondary liver ca
27	v851 - bmi 19-24 adult	0.0049261	0.0090439	0.0184744	0.0298913	0.008	0.004	0.009	0.011	0.007	0.010	5070 - food/vomit pneumonitis

Figure 2: Slope of comorbidity prevalence among the commonest 100 base MSDRGs in all four levels of risk in the UHC methodology. Comorbidities are shown in descending order of slope magnitude.

(and across all four) risk categories. These changes in prevalence were measured as slopes (Figure 2).

Discharge level data was downloaded onto the left hand side of eight spreadsheets, one for each of the four risk adjustment levels in each risk adjustment methodology. Separate columns contained for each discharge the groupings APRDRG, MSDRG, and base MSDRG (UHC), and up to 50 coded comorbid conditions. Each sheet was sorted by the grouping used in that risk adjustment methodology so that discharges in the same grouping were in contiguous rows.

Counting comorbid conditions was achieved by creating a grid on the right of each spreadsheet defined by the hundred commonest groupings (displayed along a row as column headings) and (to the left of these displayed in a column as row headings) all the comorbidities that occurred once or more often. Cells at the junction of a particular comorbidity row and a particular grouping column were programmed to calculate the number of times this comorbidity occurred in discharges belonging to that grouping (within the level of risk to which the current spreadsheet was assigned). This is shown in Figure 1.

In order to count comorbidities in these cells, a text statement was developed for each cell that would, later, be converted to a calculating formula. The text statement is shown in Figure 1 (above the arrow) as it was written in the formula bar for the highlighted cell. This statement was assembled from concatenated fragments such as "=" and ")" (also shown in Figure 1 below the formula bar), whose spreadsheet location was specified in the formula bar text. As the text statement was entered into each cell, adjusted to reflect the particular row and column of that cell, the cell processed "concatenate" commands and cell references in the text, displaying the simpler statement shown in the highlighted cell in Figure 1. This simplified statement, copied and "pasted as value," was next converted to a formula in all grouping columns by using the Excel command "replace" to change "=" to "=". This apparently purposeless maneuver actually forces each cell to reexamine the text statement and then treat it as a formula.

With the text statement changed to a formula, each cell now directs that occurrences of the comorbidity named in the current row be counted among the spreadsheet's 50 columns devoted to comorbidities. However, this comorbidity count is to be limited to the range of rows containing patients in the grouping named by the current column. For example, suppose in Figure 1 that the current cell in

the "Above" risk level spreadsheet is the one highlighted at the junction of MSDRG 88 (the grouping naming the current column) and "V 8545 BMI > 69 adult" (the comorbidity naming the current row). The highlighted cell is instructing that all instances of "v8545" be counted in the 50 comorbidity columns ("s" through "bo"). However, counting must occur only in the row range that contains discharges in the "Above" risk level of MSDRG 88 (rows 8434 through 8545).

The first of these rows was found in this clinical grouping column (MSDRG in Figure 1) using Excel's "match" function with the grouping name and risk level. Finding the last row was achieved by adding to the "match" result the number of rows containing that name (using the "countif" function).

In this manner, the number of occurrences of each comorbidity among patients belonging to each grouping was calculated in a matrix format. Occurrences in individual groupings or across any number of groupings could then readily be summed at each level of risk. Prevalence was reported as the number of comorbidity occurrences divided by the number of discharges, either in a single grouping or across a range of groupings.

The second step in spreadsheet manipulation was to evaluate changes in the prevalence of each comorbidity, either within a particular grouping or across the commonest groupings, as risk levels increase. This was achieved by transferring the list of calculated comorbidity prevalences for each risk level into a new spreadsheet and determining rate of change in these values (slope) for each comorbid condition between risk levels from minor to extreme (APRDRG) or well below to well above (UHC). Those morbidities with the largest slopes were then identified by sorting (Figure 2).

3. Results

The 100 commonest groupings (accounting for about 90% of discharges) were examined all together in both risk adjustment methods, and the ten commonest (about 30%) were examined from the perspective of individual grouping.

Shown in Table 1 are comorbidities with the largest 25 slopes across all risk levels for the 100 commonest groupings in the two risk adjustment systems. The two methods shared 18 of the 25.

Table 1: Comorbidities with the greatest slopes across all four risk levels in the methods used by UHC and 3M.

Comorbidity	3M	UHC
584.9: acute renal failure NOS	×	×
428.: CHF unspecified	×	×
518.81: acute respiratory failure	×	×
599.: urin tract INFEC/bacteriuria	×	×
V66.7: encounter for palliative care	×	×
486: pneumonia, organism NOS	×	×
57.: food/vomit pneumonitis	×	×
427.31: atrial fibrillation	×	×
414.1: cornry atherosclerosis native	×	×
511.9: pleural effusion NOS	×	×
276.1: Hyposmolality	×	×
518.: pulmonary collapse	×	×
276.2: acidosis	×	×
E849.7: ACCID in resident INSTIT	×	×
43.9: HY KID NOS W CR KID I-IV	×	×
198.5: secondary malig neo bone	×	×
285.9: anemia NOS	×	×
995.92: severe sepsis	×	×
25.: DMII WO COMP NT ST UNCNTR	×	
785.52: septic shock	×	
272.4: hyperlipidemia NEC/NOS	×	
V15.82: history of tobacco use	×	
77.3: decubitus ulcer, low back	×	
41.9: hypertension	×	
38.9: septicemia NOS	×	
276.8: hypopotassemia		×
276.51: dehydration		×
244.9: hypothyroidism NOS		×
276.7: hyperpotassemia		×
585.9: chronic kidney dis NOS		×
287.5: thrombocytopenia NOS		×
197.7: secondary liver Ca		×

4. Discussion

Using this inductive method, we identified comorbid conditions that were associated with increases in morbidity risk category at a particular institution. It appears that the method, applied here to two, could be used for many risk-adjustment paradigms. Hospitals now focus on educating doctors about the importance of documenting comorbid conditions that increase the complexity and reimbursement of common DRGs. Perhaps equally important in maximizing revenue and hospital reputation will be educating doctors to identify and document those conditions that increase risk of death. Risk may be measured by different insurers using different methods, making an inductive approach to assessing the results of any method easier for a hospital than trying to duplicate each method.

An important limitation of this approach is that it cannot distinguish diagnoses *defining* increased risk from those *associated* with increased risk. The first is clearly a subgroup of the second, raising questions not about sensitivity but the specificity of this method. An important topic for future study is whether the likelihood increases with its slope that a particular comorbidity *places* rather than *accompanies* patients into a higher risk category.

Knowledge of comorbidities associated with risk has, of course, the potential both to improve and to undermine precision in risk adjustment. Just as it is likely for a hospital to undercode comorbid conditions that it does not know to be important, so the possibility of overcoding arises when a hospital knows or suspects which diagnoses will increase reported risk of death (and therefore improve its observed/expected mortality). On the other hand, it can be

argued that hospitals, which already suffer regulatory and financial consequences when they are found to overcode, should not also, through ignorance of the basis for risk, be systemically encouraged to underestimate their expected mortality [20, 21]. In assessing the effect of this or other methods that may be developed to deconstruct risk adjustment paradigms, it is important to measure the effect both on recognition and documentation of conditions that would otherwise be missed and on reporting of conditions that are not in fact present. As risk-adjusted mortality grows to be more important a measure, these studies will hopefully be performed.

Finally, it should be noted that widespread use of any technique that accurately increases documentation and coding as a specific and rapid response to the results of risk adjustment may in turn affect the process of risk adjustment itself. For example, a comorbidity more widely reported because it is identified as enhancing risk will enhance risk less. Shared knowledge of risks between adjusters and clinicians may well create a dynamic relationship with unknown effects.

References

[1] W. W. Young, S. Kohler, and J. Kowalski, "PMC patient severity scale: derivation and validation," *Health Services Research*, vol. 29, no. 3, pp. 367–390, 1994.

[2] P. M. Steen, A. C. Brewster, R. C. Bradbury, E. Estabrook, and J. A. Young, "Predicted probabilities of hospital death as a measure of admission severity of illness," *Inquiry*, vol. 30, no. 2, pp. 128–141, 1993.

[3] J. S. Gonnella, M. C. Hornbrook, and D. Z. Louis, "Staging of disease. A case-mix measurement," *JAMA*, vol. 251, no. 5, pp. 637–644, 1984.

[4] S. Meur, Mortality risk adjustment methodology for university health system's clinical data base, 2011, http://www.ahrq.gov/qual/mortality/Meurer.pdf.

[5] J. Daley, S. Jencks, D. Draper, G. Lenhart, N. Thomas, and J. Walker, "Predicting hospital-associated mortality for Medicare patients. A method for patients with stroke, pneumonia, acute myocardial infarction, and congestive heart failure," *JAMA*, vol. 260, no. 24, pp. 3617–3624, 1988.

[6] S. D. Horn, P. D. Sharkey, J. M. Buckle, J. E. Backofen, R. F. Averill, and R. A. Horn, "The relationship between severity of illness and hospital length of stay and mortality," *Medical Care*, vol. 29, no. 4, pp. 305–317, 1991.

[7] M. P. Hurtando, E. R. Swift, and J. M. Corrigan, Eds., *Envisioning the National Health Care Quality Report*, National Academy Press, Washington, DC, USA, 2001.

[8] L. I. Iezzoni, "Assessing quality using administrative data," *Annals of Internal Medicine*, vol. 127, no. 8, pp. 666–673, 1997.

[9] M. H. Park and E. A. Hiller, "Medicare Hospital Value-Based Purchasing: the evolution toward linking Medicare reimbursment to health care quality continues," *Health Care Law Monthly*, vol. 2011, no. 2, pp. 2–9, 2011.

[10] L. I. Iezzoni, "The risks of risk adjustment," *JAMA*, vol. 278, no. 19, pp. 1600–1607, 1997.

[11] J. S. Hughes, L. I. Iezzoni, J. Daley, and L. Greenberg, "How severity measures rate hospitalized patients," *Journal of General Internal Medicine*, vol. 11, no. 5, pp. 303–311, 1996.

[12] L. I. Iezzoni, A. S. Ash, M. Shwartz, J. Daley, J. S. Hughes, and Y. D. Mackieman, "Judging hospitals by severity-adjusted mortality rates: the influence of the severity-adjustment method," *American Journal of Public Health*, vol. 86, no. 10, pp. 1379–1387, 1996.

[13] M. Kamalesh, J. Shen, and W. M. Tierney, "Stroke mortality and race: does access to care influence outcomes?" *American Journal of the Medical Sciences*, vol. 333, no. 6, pp. 327–332, 2007.

[14] S. R. Connor, B. Pyenson, K. Fitch, C. Spence, and K. Iwasaki, "Comparing hospice and nonhospice patient survival among patients who die within a three-year window," *Journal of Pain and Symptom Management*, vol. 33, no. 3, pp. 238–246, 2007.

[15] P. Wilson, S. R. Smoley, and D. Werdegar, "Second report of the California hospital outcomes project. Acute myocardial infarction. Volume Two," Technical Appendix, Office of Statewide health Planning and Development, Sacremento, Calif, USA, 1996.

[16] S. F. Jencks, D. K. Williams, and T. L. Kay, "Assessing hospital-associated deaths from discharge data. The role of length of stay and comorbidities," *JAMA*, vol. 260, no. 15, pp. 2240–2246, 1988.

[17] A. Elixhauser, C. Steiner, D. R. Harris, and R. M. Coffey, "Comorbidity measures for use with administrative data," *Medical Care*, vol. 36, no. 1, pp. 8–27, 1998.

[18] L. G. Glance, T. M. Osler, D. B. Mukamel, and A. W. Dick, "Impact of the present-on-admission indicator on hospital quality measurement: experience with the agency for healthcare research and quality (AHRQ) inpatient quality indicators," *Medical Care*, vol. 46, no. 2, pp. 112–119, 2008.

[19] L. G. Glance, A. W. Dick, T. M. Osler, and D. B. Mukamel, "Accuracy of hospital report cards based on administrative data," *Health Services Research*, vol. 41, no. 4, pp. 1413–1437, 2006.

[20] L. I. Iezzoni, S. M. Foley, J. Daley, J. Hughes, E. S. Fisher, and T. Heeren, "Comorbidities, complications, and coding bias: does the number of diagnosis codes matter in predicting in-hospital mortality?" *JAMA*, vol. 267, no. 16, pp. 2197–2203, 1992.

[21] J. Green and N. Wintfeld, "How accurate are hospital discharge data for evaluating effectiveness of care?" *Medical Care*, vol. 31, no. 8, pp. 719–731, 1993.

Hindawi Publishing Corporation
Computational and Mathematical Methods in Medicine
Volume 2012, Article ID 469769, 9 pages
doi:10.1155/2012/469769

Research Article

Predictive Models for Maximum Recommended Therapeutic Dose of Antiretroviral Drugs

Michael Lee Branham,[1] Edward A. Ross,[2] and Thirumala Govender[1]

[1] *School of Pharmacy and Pharmacology, University of KwaZulu-Natal, Durban 4001, South Africa*
[2] *School of Medicine, University of Florida, Gainesville, FL 32601, USA*

Correspondence should be addressed to Michael Lee Branham, malimahweh@gmail.com

Received 11 September 2011; Revised 4 November 2011; Accepted 18 November 2011

Academic Editor: John Hotchkiss

A novel method for predicting maximum recommended therapeutic dose (MRTD) is presented using quantitative structure property relationships (QSPRs) and artificial neural networks (ANNs). MRTD data of 31 structurally diverse Antiretroviral drugs (ARVs) were collected from FDA MRTD Database or package inserts. Molecular property descriptors of each compound, that is, molecular mass, aqueous solubility, lipophilicity, biotransformation half life, oxidation half life, and biodegradation probability were calculated from their SMILES codes. A training set ($n = 23$) was used to construct multiple linear regression and back propagation neural network models. The models were validated using an external test set ($n = 8$) which demonstrated that MRTD values may be predicted with reasonable accuracy. Model predictability was described by root mean squared errors (RMSEs), Kendall's correlation coefficients (tau), P-values, and Bland Altman plots for method comparisons. MRTD was predicted by a 6-3-1 neural network model (RMSE = 13.67, tau = 0.643, $P = 0.035$) more accurately than by the multiple linear regression (RMSE = 27.27, tau = 0.714, $P = 0.019$) model. Both models illustrated a moderate correlation between aqueous solubility of antiretroviral drugs and maximum therapeutic dose. MRTD prediction may assist in the design of safer, more effective treatments for HIV infection.

1. Introduction

Acquired immunodeficiency syndrome (AIDS) is a degenerative disease of the immune and central nervous systems caused by the human immunodeficiency virus (HIV). There are an estimated 33.2 million people living with HIV/AIDS globally [1–3]. Of this number, 22.5 million are in Sub-Saharan Africa, which represents 67.8% of the global number [3]. Antiretroviral drugs (ARVs) may be classified as nucleoside reverse transcriptase inhibitors (NRTIs), nucleotide reverse transcriptase inhibitors (NtRTI), non-nucleoside reverse transcriptase inhibitors (NNRTIs), protease inhibitors (PI), and more recently as fusion or integrase inhibitors [4, 5]. Since most ARVs have low aqueous solubility and poor bioavailability, several alternative drug delivery strategies have been proposed to optimize systemic concentrations [6, 7]. The important biopharmaceutical properties that need to be considered for effective ARV delivery systems might include solubility, pKa, lipophilicity, permeability, stability in biological fluids, gastrointestinal metabolism, and where possible viral reservoir targeting [6, 8, 9]. To overcome suboptimal biopharmaceutical properties, ARVs are often prescribed at high daily doses which increase the occurrence of adverse side effects and toxicities [10, 11]. Combination therapy, comprising at least three anti-HIV drugs, has become a standard treatment of AIDS [12], but here again the potential for adverse side effects and drug-related noncompliance increases. To address these issues, computational methods have been used to predict dose-limiting toxicities of a few antiretroviral drugs [13, 14] or to optimize ARV formulations [15, 16]. The ability to predict maximum therapeutic dose directly from molecular structure is both clinically and scientifically attractive in terms of treatment management and reducing drug development costs [17]. Unfortunately, such models for drugs used in the treatment of AIDS do not yet exist. Accurate prediction

of the MRTD for antiretroviral type compounds would be particularly useful in formulation studies so that clinically relevant extrapolations on drug dissolution and permeability can be made earlier in the drug development process [17–20]. Several recent studies have been conducted to define a relationship between the dose and physicochemical properties of the drug [20, 21], or to investigate the underlying mechanisms of drug toxicity and bioaccumulation [20, 22]. Still, the prediction of optimal dose continues to challenge pharmaceutical scientists because of its complexity and variability between different organisms. Artificial neural networks (ANNs) have emerged as a powerful tool suitable for processing complex relationships between molecular stimuli and biological system responses [23]. Examples include prediction of warfarin maintenance dose [24], gentamicin steady-state plasma concentrations [25], skin permeability [26], and prediction of HIV drug resistance [27]; supporting data for these and other studies suggest the utility of neural network modeling for predicting maximum therapeutic doses.

We believed that since the MRTD estimates are derived from human data, they would provide a more relevant, accurate, and specific estimate for toxic dose levels compared to risk assessment models based on animal data alone. In this article, we predict the MRTD of antiretroviral drugs from their molecular structures using relevant molecular property descriptors and neural network software as a data mining tool. Predictive performance of the models were evaluated and statistically compared with the results obtained clinically or reported in the literature. The application of predictive models in the design of safe, effective antiretroviral drug delivery systems is discussed.

2. Materials and Methods

2.1. Chemoinformatic Software and Modeling Tools. The physicochemical descriptors, molecular weight (MW), aqueous solubility (ASol), and lipophilicity (AlogP) were determined using ALOGPS 2.1. Virtual Computational Chemistry Laboratory, (http://www.vcclab.org/) [28, 29]. Bioaccumulation descriptors, log biotransformation half life (logBioHL), oxidation half life (OxidHL), and biodegradation probability (P[BD]) were determined using EPI Suite v.410 (http://www.epa.gov/oppt/sf/tools/methods.htm) [30, 31]. All inferential statistics and MRTD data analysis was performed using MedCalc v.12 (MedCalc Software bvba, Belgium). Artificial neural network analysis was performed using Tiberius Data Mining Software v.6.1.9 (Tiberius Data Mining Software Ltd. Pty, UK).

2.2. MRTD Training and Validation Datasets. The MRTD of 31 structurally diverse antiretroviral drugs were taken from the FDA MRTD database or package inserts. This "clinical MRTD" dataset was randomly split into training and validation subsets as shown in Table 1. Subsequently, each of the calculated descriptors and clinical MRTD values were correlated by multiple linear regression analysis and the results used to identify statistically significant property descriptors. An error back propagation algorithm was used for network training, with learning rate set at 0.7. A tangent sigmoid transfer function on the first layer and two neurons with a nonlinear transfer function on the hidden layer were minimalistic structures used to reduce over-fitting. Results of MRTD versus molecular property descriptors with multiple correlation coefficients are listed in Table 2. For the neural network model training, correlation and error statistics are listed in Table 3.

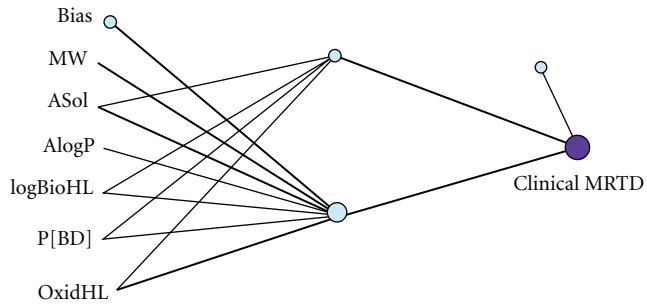

Figure 1: A neural network model was constructed with (2) hidden neuron, (1) output variable that is Clinical MRTD, and (6) input variables that is, OxidHL, P[BD], logBioHL, AlogP, ASol, MW. Total number of patterns (23) were loaded in the data of which 23 were complete and available for training. Two nonlinear neurons were used and the model error minimization was stable for 20 minutes.

2.3. Model Validation and Statistical Comparisons. The predictability of each of the multiple linear regression (MLR) and neural network (TNN) models was evaluated by a cross-validation procedure [32]. Each model was constructed on the basis of the same training dataset and was subsequently used to predict the excluded test data. Statistical comparisons were performed between the clinical MRTD and predicted MRTD values using the root mean squared error (RMSE), Kendall's correlation coefficient (tau), *P*-value, and Bland Altman plots for methods comparisons.

3. Results

3.1. Model Predicted versus Actual MRTD Estimates. In this multivariable system, a quantitative relationship between certain molecular property descriptors and maximum recommended therapeutic dose was characterized using two datasets (i.e., MRTD and TEST). A multiple linear regression (Table 2) and a 6-2-1-neural network model (Figure 1) for the prediction ARVs maximum dose were constructed. Table 1 lists summary statistics for the molecular property descriptors and corresponding MRTD values in each dataset. The ARVs in this study, although few in number, covered a broad range (CV equal to 40% or greater) in terms of the physicochemical (MW, ASol, AlogP) and bioaccumulation properties (logBioHL, OxidHL, P[BD]) included. A significant difference in mean ASol between training set (6.1489 g/L) and TEST set (0.436 g/L) was noted although corresponding changes in lipophilic character were not as great. Multiple linear regression analysis was performed with results listed in Table 2. A statistically significant but modest correlation between two of the six descriptors, that is, P[BD]

Table 1: Clinical MRTD data consisted of 23 training set compounds (italic) and 8 test set compounds (bold). Mean and standard deviation statistics are shown indicating the distribution and central tendency of each molecular property descriptor.

Drug	MRTD (mg/kg/day)	OxidHL (days)	P[BD] (%)	logBioHL (days)	AlogP (:)	ASol (g/L)	MW (Da)
Acyclovir	13.30	0.135	0.5475	−2.2874	−1.45	8.65	225.21
Ancitabine	20.00	0.139	0.2005	−2.418	−2.62	3.20	225.21
Delaviridine	6.67	0.034	0.0014	−2.3428	2.77	0.086	456.57
Didanosine	6.67	0.140	0.5085	−1.9956	−1.26	6.43	236.23
Famciclovir	25.00	0.051	0.991	−3.6235	0.13	1.32	321.38
Foscarnet	120.00	13.37	0.772	−2.4547	−1.63	16.76	126.01
Indinavir	16.70	0.038	0.0501	−4.6478	3.26	0.048	613.81
Lofexidine	0.040	0.123	0.0792	0.9861	3.31	0.15	259.14
Lamivudine	5.00	0.06	0.0719	−3.9261	−1.29	2.76	229.26
Rimantadine	3.33	0.171	0.4624	0.4539	3.28	0.009	179.31
Ribavirin	200.00	0.264	0.8963	−2.8715	−1.92	33.17	244.21
Valacyclovir	50.00	0.044	0.944	−3.3309	−1.03	1.49	326.41
Zalcitibine	0.0375	0.096	0.0909	−3.5083	−1.29	7.05	211.22
Zanamivir	0.333	0.038	0.8247	−4.4141	−2.29	1.49	332.32
Zidovudine	10.00	0.139	0.0432	−3.0445	−0.1	16.35	267.28
Saquinavir	33.330	0.052	0.9780	−3.9394	4.04	0.002	670.84
Darunavir	53.00	0.094	0.0001	−1.8175	1.76	0.067	547.66
Tipranavir	6.670	0.043	0.0000	−0.0265	5.71	0.0002	602.66
Ritonavir	20.00	0.105	0.9488	−4.61	4.24	0.0012	720.94
Maraviroc	20.00	0.129	0.0700	−0.2247	4.3	0.0106	513.66
Tenofovir	10.00	0.048	0.0016	−3.0098	−1.51	1.87	287.21
Nelfinavir	25.00	0.055	0.6868	−1.6709	6.00	0.0002	567.78
Stavudine	1.333	0.088	0.0768	−3.082	−0.8	40.51	224.21
n	23.00	23.00	23.00	23.00	23.00	23.00	23.00
mean	28.54	0.672	0.402	−2.5133	0.939	6.15	362.72
SD	45.53	2.769	0.394	1.5738	2.809	10.90	178.20
CV%	159.52	412.00	97.00	−62.620	299.04	177.25	48.86
Abacavir	10.00	0.040	0.0229	−2.1757	0.61	1.21	286.38
Emtricitabine	4.00	0.08	0.0566	−3.7784	−0.8	2.00	247.28
Raltegravir	30.07	0.094	0.0006	−2.6157	1.7	0.095	444.47
Nevirapine	3.000	0.167	0.0473	−3.7336	1.75	0.10	266.33
Efavirenz	10.10	0.254	0.0001	0.1111	3.88	0.008	315.67
Fosamprenavir	46.70	0.067	0.0007	−2.4135	0.84	0.068	585.68
Atazanavir	5.35	0.109	0.0202	−3.4392	4.37	0.003	704.96
Lopiravir	53.33	0.103	0.9933	−3.3281	4.07	0.002	614.86
n	8.00	8.00	8.00	8.00	8.00	8.00	8.00
mean	20.32	0.114	0.143	−2.672	2.05	0.436	433.20
SD	20.29	0.067	0.344	1.278	1.878	0.753	180.48
CV%	99.86	58.99	241.300	−47.830	91.50	173.000	41.66

(R_z = 0.427, P = 0.035), ASol (R_z = 0.476, P = 0.014) and actual MRTD value is noted. MRTD values appear to increase with P[BD], ASol, and OxidHL; but decrease with increasing logBioHL, AlogP, or MW. The multiple correlation coefficient (MCC = 0.7727), residual error (RSD = 33.89), and ANOVA (P = 0.013) indicate acceptable predictability of the multiple regression model for ARVs maximum dose. A multiple linear regression equation used for the prediction of MRTD is as follows:

$$\begin{aligned} &-34.3303 - 12.20 * (\text{AlogP}) + 2.1249 * (\text{ASol}) \\ &+15.90 * (\text{logBioHL}) + 0.2159 * (\text{MW}) \\ &+5.659 * (\text{OxidHL}) + 46.5133 * (\text{P[BD]}). \end{aligned} \quad (1)$$

Table 2: The results of the multiple linear regression analysis for antiretroviral drugs versus MRTD. In the training, dataset only two of the six molecular descriptors showed a statistically significant correlation with therapeutic dose, that is, P[BD] ($P = 0.0349$) and ASol ($P = 0.0140$). A multiple regression model equation coefficients are listed with there standard errors, coefficient of determination ($R^2 = 0.5970$), multiple correlation coefficient (MCC = 0.7727) and residual standard deviation (RSD = 33.89).

Multiple linear regression	$n = 23$	$R^2 = 0.5970$	RSD = 33.89	MCC = 0.7727
independent variables	Coefficient	SE	P-value	R_z
Constant	−34.3303			
AlogP	−12.1995	6.6976	0.0873	−0.221
ASol	2.1239	0.7697	0.0140	0.476
logBioHL	15.9000	8.0377	0.0654	−0.071
MW	0.2159	0.1015	0.0494	−0.116
OxidHL	5.6589	2.8478	0.0643	0.448
P[BD]	46.5133	20.1746	0.0349	0.427
ANOVA	F-ratio = 3.9507		$P = 0.013$	

Table 3: The results of the neural network analysis for antiretroviral drugs versus MRTDs. All molecular descriptors show weak correlation with MRTD except for ASol, OxidHL, and P[BD]. The 6-2-1 neural network model predicted training set MRTD values with high accuracy ($R^2 = 0.992$, MAX = 13.64, $P < 0.001$). No multicollinearity between independent variables was observed in the training set.

6-2-1 neural network	$n = 23$	$R^2 = 0.992$	MAX = 13.64	RMSE = 5.53
Model versus clinical MRTD	$P < 0.001$		Learning rate = 0.700	
Independent variables	Correlation coefficients		R^2	
AlogP	−0.221		0.049	
ASol	0.476		0.226	
logBioHL	−0.071		0.005	
MW	−0.116		0.013	
OxidHL	0.448		0.201	
P[BD]	0.427		0.182	
ANOVA	F-ratio = 1340.73		$P < 0.001$	

The results of the neural network model for antiretroviral MRTDs is shown in Table 3. All molecular descriptors show weak correlation with MRTD except ASol, OxidHL, and P[BD]. The 6-2-1 neural network predicted training set MRTD values with high accuracy ($R^2 = 0.992$, MAX = 13.64, $P < 0.001$). No multicollinearity between independent variables was observed in the training set. SPSS code for the 6-2-1 neural network may be executed as follows:

```
COMPUTE Var1 = ((OxidHL *
(−0.543086558961242)) +
3.63976611815824)
 + ((Pr_BD_ * (−5.67413921537257)) +
2.81153598121711)
+ ((LogBioHL * (0.40828801067156)) +
0.747514104338025)
+ ((ALogP * (−0.848110602763694)) +
1.43330691867064)
 + ((Sol * (−2.55399028293542E−02)) +
0.517313285798853)
+ ((MW * (1.40343495376914E−02)) −
5.94322423917294)
+ 3.86733992096867.
COMPUTE Var2 = ((OxidHL *
(8.23491975851945E−02)) -
0.551904322215974)
+ ((Pr_BD_ * (3.12529587401663)) -
1.54858410557524)
+ ((LogBioHL * (0.431493610228662)) +
0.790000076287146)
+ ((ALogP * (−0.04107624611641)) +
6.94188559367329E−02)
+ ((Sol * (4.12997852313067E−02)) −
0.836531279838639)
+ ((MW * (1.05078568602304E−03)) −
0.444983569959981)
+ 9.28741349960935E-02.
COMPUTE Var3 = −0.535249116383622.
Execute.
COMPUTE Var1 = 0.108990429907616 * Var1.
COMPUTE Var2 = 1.44376333322051 *
(Exp(Var2) − Exp(-Var2)) / (Exp(Var2) +
Exp(−Var2)).
COMPUTE Var3 = Var3.
```

Table 4: Test dataset Goodness of fit comparisons. Clinical MRTD values from 8 ARVs were using as and external test dataset the validate model predictability. Model performance is characterized here in terms of root means squared error (RMSE), Kendall's correlation coefficient (tau), and Type II error probability (*P*-value).

Drug	MRTD	MLR	SE	TNN	SE
Abacavir	10.00	−10.6738	427.4060	6.4861	12.3474
Emtricitabine	4.00	−23.9239	779.7441	3.3678	0.3996
Raltegravir	30.07	0.0628	900.4320	19.7700	106.0900
Nevirapine	3.00	−54.1862	3270.2614	−16.5700	382.9849
Efavirenz	10.10	−10.2863	415.6012	−5.7782	252.1172
Fosamprenavir	46.70	44.0515	7.0145	50.7500	16.4025
Atazanavir	5.35	11.4360	37.0393	29.8700	601.2304
Lopiravir	53.33	42.6361	114.3594	64.5900	126.7876
Mean	20.32	−0.1105	RMSE = 27.27	19.06	RMSE = 13.67
Kendall's tau		0.714		0.643	
P-value		0.019		0.035	

```
Execute.
COMPUTE Tiberius_MRTD = ((((Var1 +
Var2 + Var3)/2.0) + 0.5) * 199.9625)
+ 0.0375.
Execute.
```

3.2. Model Validation and Statistical Comparisons. Each of the models was then validated using external TEST MRTD dataset and a cross-validation procedure. Model "goodness of fit" and predictability are summarized in Table 4. RMSE of the 6-2-1 neural network (RMSE = 13.67) was substantially less the multiple linear regression model (RMSE = 27.27). Comparison of model predictivity was confirmed with TNN having maximum squared error (SE = 601.23) compared to MLR (SE = 3270.26). Model Figure 3 correlation with the clinical MRTD values using Kendall's correlation coefficient was, however, greater for the MLR (tau = 0.714, $P = 0.019$) than the resultant 6-2-1 neural network model (tau = 0.643, $P = 0.035$). Bland Altman plots for methods comparison further illustrate the predictive value of the neural network (TNN) and multiple linear regression (MLR) models. The upper and lower limits of agreement for the MLR (58.3, −17.4) and TNN (29.8, −27.3) are illustrated in Figure 2. While it can be seen that all of the differences lie between these limits, MLR model limits of agreement were wider than the TNN model, which were more narrow and nearly symmetrical.

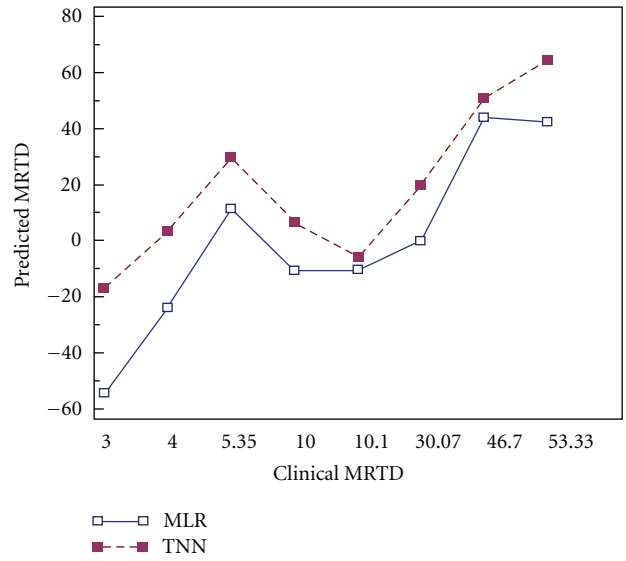

Figure 2: Method comparisons graph. MRTD values predicted by multiple linear regression (hollow squares, □) nearly traced those values predicted by the 6-2-1 neural network (solid squares, ■) as shown. Multiple linear regression estimates for MRTD were consistently lower that those predicted by the neural network model.

4. Discussion

MRTD values and SMILES codes for antiretroviral drugs were collected from the FDA MRTD database which is a highly reliable source pharmacologic activity based on extensive clinical evidence (http://www.fda.gov/cder/). The ALOGPS+ program was used for the calculation of molecular mass (MW), solubility (ASol), and lipophilicity (AlogP) without alteration. The precision and robustness of these tools are well established in the pharmaceutical and modeling community and its predictive power concerning the input parameters in question are published on the company website (http://www.vcclab.com/) and cited in the manuscript [28, 29, 33]. Independent validation of the parameters calculated with ALOGPS has been published [33, 34] and the estimates were found to be appropriately accurate for the use intended. The bioaccumulation input parameters, oxidation half life (oxidHL), log biotransformation half life (logBioHL), and biodegradation probability (P[BD]) were calculated using the EPI Suite software which is publically available and has been validated in hundreds of modeling experiments for the estimated parameters. EPI Suite software is continuously updated and the predictive power of its latest version is always available at the website (http://www.epa.gov/oppt/sf/tools/methods.htm). None of

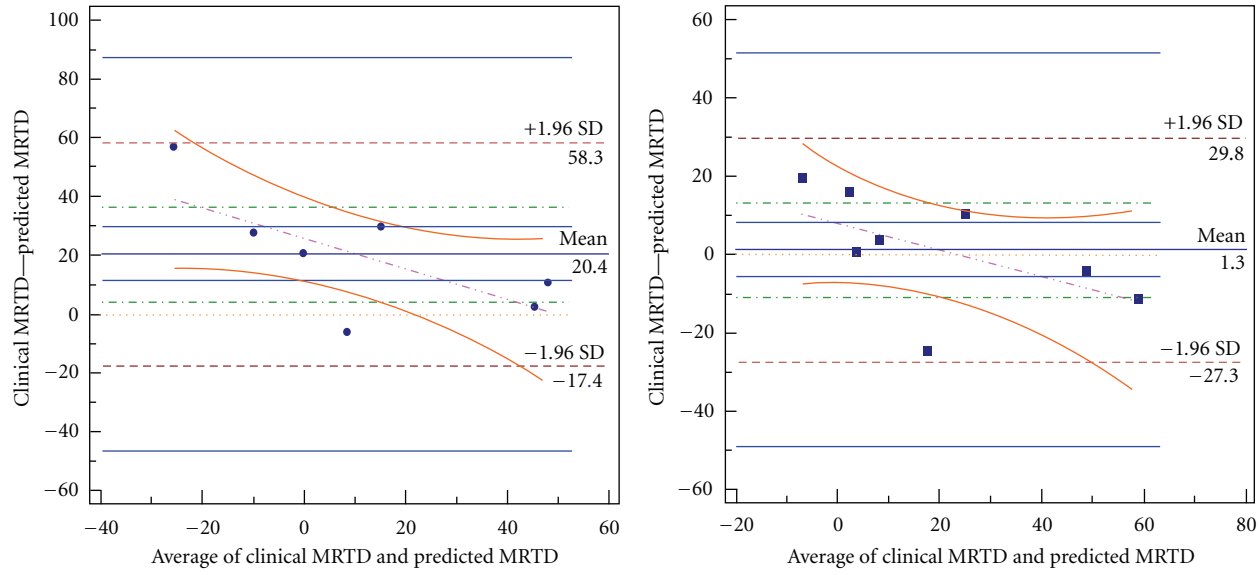

Figure 3: Bland Altman plot for method comparisons. Bland Altman plots are shown for (a) multiple linear regression predicted versus clinical MRTD, and (b) neural network model predicted versus clinical MRTD. Horizontal lines are drawn at the mean difference, and at the limits of agreement. All predicted values were within limits of agreement for both models, althought these limits were more narrow for the neural network model estimates. The plots are useful revealing the relationship between the differences and the averages, the slight deviation from symmetry in the multiple regression indicates some systematic bias but no possible outliers were identified.

the parameters were log-transformations of the software output but instead used as direct input values for the training set. Although some of the predictor values ranged over 3 orders of magnitude, this did not appear to adversely affect comparisons of the MLR or ANN methods. Furthermore, because of the highly diverse nature of antiretroviral compounds in terms of physicochemical descriptors and split-data validation procedure with randomly selected training and test sets instead of cross-validating scheme. It is our intention to adapt the method as new ARV drugs become listed in evolving FDA database.

We began our study looking at dose-related adverse effects of commercial antiretroviral drugs or new ARVs in development. Although the appearance of serious long-term metabolic complications, such as cardiovascular disturbances [35], hyperlipidemia [35, 36], and diabetes, have been extensively reported [35, 37], few reports on computational models to predict these dose-limiting toxicities [38, 39] can be found in the literature. A mathematical model to predict the optimal dosing regimen for AIDS therapy has been reported [40], but in this case, CD4+ cell counts and knowledge of the adherence interval of individual patients is required to adjust the dose. While the model was effective at reducing dose-limiting toxicities in an AIDS patient population, it cannot be applied to nonapproved ARV formulations or to drugs in development. Since the overwhelming majority of anti-HIV drugs demonstrate efficacy over a small range of treatment doses, MRTD predicting models would be beneficial to the drug delivery scientist who needs to design experiments based on the most effective therapeutic dose of the medication [41]. The MRTD is empirically derived from human clinical trials, thus it is a direct measure of the threshold for dose-related adverse effects in humans. Prediction of the MRTD from molecular structure is of importance for both new and existing drugs which may require modifications to improve their aqueous solubility or bioavailability *in vivo*. ARVs fit this description also and are excellent subject molecules for predictive modeling to estimate maximum dose. Unfortunately, the number of antiretroviral drugs with established MRTD is yet small, so the development of models specifically of ARVs is both tedious and rare.

The molecular descriptors used in this study were selected to represent physicochemical (MW, AlogP, ASol) and bioaccumulation (OxidHL, P[BD], logBioHL) property influences therapeutic dose. Although molecular weight does not strongly correlate with toxicity of most compounds, the larger the molecular size of a compound, the smaller its membrane permeability and diffusion coefficient become [34]. Therefore, compounds with higher weights are less likely to be absorbed, which limits their systemic toxicity. Results of this study predict no correlation between molecular weight and maximum ARV dose. In contrast, bioactivity and drug toxicity almost always increase with increasing lipophilicity. This is due in part to the fact that lipophilic molecules tend to cross cellular membranes more readily increasing exposure and residence in the body. In addition, lipophilic drugs are characterized by increased plasma protein binding, thus an assessment of lipophilicity is almost always included in the physicochemical evaluation of a drug because of its close association with pharmacologic, permeability and potential bioaccumulation [42, 43]. Our

results here did not indicate AlogP or lipophilic character as having any influence on ARV dose. The aqueous solubility of a compound significantly affects its absorption and distribution characteristics. Typically, low solubility goes along with a poor absorption and, therefore, its systemic toxicity reduced, however, local irritability may develop and/or reduced elimination rates, both are characteristic of drugs with low aqueous solubility. For highly potent drugs, increasing solubility usually enhances the elimination rate and lowers systemic half life, [44]. This means that for ARVs with low aqueous solubility, some correlation with maximum therapeutic dose (as we has shown) is likely to be observed.

Any chemical (even water) can produce toxic side effects in the body if allowed to accumulate to sufficiently large concentrations. While much of the effort in bioaccumulation modeling [43, 45] has been initiated by scientists estimating the equilibrium distribution of chemicals between organisms and their environments (e.g., fish-water, plants-soil), effective physicochemical property estimation routines (i.e., PERs) have resulted from these studies that may be applied to similar biodistribution problems in pharmaceutical research. For example, oxidation half life (OxidHL) is an estimate of the molecules ability to form stable hydroxyl radicals or to interact with such moiety under ambient conditions. Formation of hydroxyl-radicals is often associated with dose-limiting toxicities. Although in our studies, oxidation half life was not statistically significant in the prediction of MRTD. Another bioaccumulation descriptor, biotransformation half life (logBioHL), is the (linearized) fraction of drug mass in the whole body that has been metabolized per day. Our estimates do not account for the formation of specific metabolites which may be toxic nor do they identify specific pathways in the process (i.e., phase I redox reactions or phase II type conjugation reactions). Consequently, logBioHL was not correlated with MRTD in the present study and was a weaker bioaccumulation property descriptor in comparison to oxidation half life or biodegradation probability P[BD]. The probability of biodegradation attempts to combine both oxidative and biotransformation susceptibility of the structure to give an estimate of overall persistence. P[BD] estimates are based upon molecular fragments [46–48] and in our investigation showed only moderate correlation with MRTD in both multiple linear regression and neural network models. Each of the models was evaluated for predictive accuracy and by statistical comparison. In terms of predictability, root mean squared errors were larger for the multiple linear regression than the neural network model. Some advantages of ANN over MLR models were illustrated in the current study.

Artificial neural networks (ANNs) are biologically inspired data-mining algorithms which work by detecting the patterns and relationships in data. We used the back propagation rule in which the neural network is trained to map a set of input data by iterative adjustment of the weights. A tangent sigmoid transfer function on the first layer and two neurons with a nonlinear transfer function on the hidden layer were minimalistic structures used to reduce overfitting. Our training processes for TNN were allowed to run until no change in RMSE was observed for 20 minutes, at which point the model was saved. This learning method is commonly used for neural network predictive models given dose-response type data. However, ANNs have several limitations, a major theoretical concern is the "black box" nature of the output, that is, conclusions are generated without mechanistic explanations. ANNs also are limited by the quality of their data and may need to be retrained periodically if its performance changes over time. This is not necessarily counterproductive, since it indicates robustness in the model which adapts to changes in the predictive criteria. Real-time monitoring of the training process is also important since overtraining can easily occur, especially when the datasets are small in size. This is may be one of the unique advantages of real-time visualization of the data-mining process allowing the investigator to make "intermediate evaluations" of model predictability and then continue training until the reliability and accuracy required of the predictions are met.

In conclusion, antiretroviral drugs are a chemically diverse class of compounds in terms of both physicochemical properties and bioaccumulation potential. However, commercial ARVs may be categorized for predictive modeling purposes into two groups based on aqueous solubility and lipophilic character, in which hydrophilic compounds may be administered at higher doses (MRTD) and prediction of their MRTD value may be possible using simple multiple linear regression models. In contrast, the prediction of MRTD values for antiretrovirals with poorer aqueous solubility would be the most effective when the neural network approach is used and when both physicochemical and bioaccumulation property descriptors are available for training. With regard to future studies, ANN represents a promising tool for predicting maximum therapeutic dose, especially for antiretroviral drugs with narrow therapeutic index in the treatment of AIDS.

Abbreviations

AlogP:	Calculated octanaol/water partition coefficient
ASol:	Aqueous solubility
logBioHL:	Biotransformation half life
CV:	Coefficient of variation
R^2:	Coefficient of determination
MLR:	Multiple linear regression
MRTD:	Maximum recommended therapeutic dose
MAX:	maximum absolute error
MW:	Molecular weight
MCC:	Multiple correlation coefficient
OxidHL:	Oxidation half life
P[BD]:	Biodegradation probability
TNN:	Tiberius Neural Network
QSPR:	Quantitative Structure Property Relationships
RSD:	Residual standard deviation
RMSE:	Root mean squared error
SMILES:	Simplified molecular input line entry system
SE:	Squared error
SD:	Standard deviation
R_z:	Zero order correlation coefficient.

References

[1] K. A. Pkowitz, "AIDS: the first 20 years," *New England Journal of Medicine*, vol. 344, no. 23, pp. 1764–1772, 2001.

[2] P. Piot, M. Bartos, P. D. Ghys, and N. Walker, "The global impact of HIV/AIDS," *Nature*, vol. 410, no. 6831, pp. 968–973, 2001.

[3] K. H. Mayer and K. K. Venkatesh, "Antiretroviral therapy as HIV prevention: status and prospects," *American Journal of Public Health*, vol. 100, no. 10, pp. 1867–1876, 2010.

[4] E. de Clercq, "Anti-HIV drugs: 25 compounds approved within 25 years after the discovery of HIV," *International Journal of Antimicrobial Agents*, vol. 33, no. 4, pp. 307–320, 2009.

[5] E. de Clercq, "Antiretroviral drugs," *Current Opinion in Pharmacology*, vol. 10, no. 5, pp. 507–515, 2010.

[6] G. C. Williams and P. J. Sinko, "Oral absorption of the HIV protease inhibitors: a current update," *Advanced Drug Delivery Reviews*, vol. 39, no. 1–3, pp. 211–238, 1999.

[7] E. Ojewole, I. Mackraj, P. Naidoo, and T. Govender, "Exploring the use of novel drug delivery systems for antiretroviral drugs," *European Journal of Pharmaceutics and Biopharmaceutics*, vol. 70, no. 3, pp. 697–710, 2008.

[8] C. Y. Wu and L. Z. Benet, "Predicting drug disposition via application of BCS: transport/absorption/ elimination interplay and development of a biopharmaceutics drug disposition classification system," *Pharmaceutical Research*, vol. 22, no. 1, pp. 11–23, 2005.

[9] M. A. Cosenza, M. L. Zhao, and S. C. Lee, "HIV-1 expression protects macrophages and microglia from apoptotic death," *Neuropathology and Applied Neurobiology*, vol. 30, no. 5, pp. 478–490, 2004.

[10] C. M. Bates, "HIV medicine: drug side effects and interactions," *Postgraduate Medical Journal*, vol. 72, no. 843, pp. 30–36, 1996.

[11] D. D. Richman, D. M. Margolis, M. Delaney, W. C. Greene, D. Hazuda, and R. J. Pomerantz, "The challenge of finding a cure for HIV infection," *Science*, vol. 323, no. 5919, pp. 1304–1307, 2009.

[12] C. Flexner, "HIV drug development: the next 25 years," *Nature Reviews Drug Discovery*, vol. 6, no. 12, pp. 959–966, 2007.

[13] R. D. Benz, "Toxicological and clinical computational analysis and the US FDA/CDER," *Expert Opinion on Drug Metabolism and Toxicology*, vol. 3, no. 1, pp. 109–124, 2007.

[14] P. Palumbo, H. Wu, E. Chadwick et al., "Virologic response to potent antiretroviral therapy and modeling of HIV dynamics in early pediatric infection," *Journal of Infectious Diseases*, vol. 196, no. 1, pp. 23–29, 2007.

[15] D. Woolfson, M. L. Umrethia, V. L. Kett, and R. K. Malcolm, "Freeze-dried, mucoadhesive system for vaginal delivery of the HIV microbicide, dapivirine: optimisation by an ANN," *International Journal of Pharmaceutics*, vol. 388, no. 1-2, pp. 136–143, 2010.

[16] N. Subramanian, A. Yajnik, and R. S. Murthy, "Artificial neural network as an alternative to multiple regression analysis in optimizing formulation parameters of cytarabine liposomes," *AAPS PharmSciTech*, vol. 5, no. 1, p. E4, 2004.

[17] J. F. Contrera, E. J. Matthews, N. L. Kruhlak, and R. D. Benz, "Assessment of the health effects of chemicals in humans: I. QSAR estimation of the maximum recommended therapeutic dose (MRTD) and no effect level (NOEL) of organic chemicals based on clinical trial data," *Current Drug Discovery Technologies*, vol. 1, no. 1, pp. 61–76, 2004.

[18] J. Röling, H. Schmid, M. Fischereder, R. Draenert, and F. D. Goebel, "HIV-associated renal diseases and highly active antiretroviral therapy-induced nephropathy," *Clinical Infectious Diseases*, vol. 42, no. 10, pp. 1488–1495, 2006.

[19] Y. Sun, Y. Peng, Y. Chen, and A. J. Shukla, "Application of artificial neural networks in the design of controlled release drug delivery systems," *Advanced Drug Delivery Reviews*, vol. 55, no. 9, pp. 1201–1215, 2003.

[20] E. J. Matthews, N. L. Kruhlak, R. D. Benz, and J. F. Contrera, "Assessment of the health effects of chemicals in humans: I. QSAR estimation of the maximum recommended therapeutic dose (MRTD) and no effect level (NOEL) of organic chemicals based on clinical trial data," *Current Drug Discovery Technologies*, vol. 1, no. 1, pp. 61–76, 2004.

[21] J. F. Blake, "Chemoinformatics—predicting the physicochemical properties of "drug-like" molecules," *Current Opinion in Biotechnology*, vol. 11, no. 1, pp. 104–107, 2000.

[22] D. Butina, M. D. Segall, and K. Frankcombe, "Predicting ADME properties in silico: methods and models," *Drug Discovery Today*, vol. 7, no. 11, pp. S83–S88, 2002.

[23] S. Agatonovic-Kustrin and R. Beresford, "Basic concepts of artificial neural network (ANN) modeling and its application in pharmaceutical research," *Journal of Pharmaceutical and Biomedical Analysis*, vol. 22, no. 5, pp. 717–727, 2000.

[24] I. Solomon, N. Maharshak, G. Chechik et al., "Applying an artificial neural network to warfarin maintenance dose prediction," *Israel Medical Association Journal*, vol. 6, no. 12, pp. 732–735, 2004.

[25] B. W. Corrigan, P. R. Mayo, and F. Jamali, "Application of a neural network for gentamicin concentration prediction in a general hospital population," *Therapeutic Drug Monitoring*, vol. 19, no. 1, pp. 25–28, 1997.

[26] C. W. Lim, S. Fujiwara, F. Yamashita, and M. Hashida, "Prediction of human skin permeability using a combination of molecular orbital calculations and artificial neural network," *Biological and Pharmaceutical Bulletin*, vol. 25, no. 3, pp. 361–366, 2002.

[27] S. Drăghici and R. B. Potter, "Predicting HIV drug resistance with neural networks," *Bioinformatics*, vol. 19, no. 1, pp. 98–107, 2003.

[28] I. V. Tetko, "The WWW as a tool to obtain molecular parameters," *Mini Reviews in Medicinal Chemistry*, vol. 3, no. 8, pp. 809–820, 2003.

[29] I. V. Tetko, V. Y. Tanchuk, and A. E. P. Villa, "Prediction of n-octanol/water partition coefficients from PHYSPROP database using artificial neural networks and E-state indices," *Journal of Chemical Information and Computer Sciences*, vol. 41, no. 3–6, pp. 1407–1421, 2001.

[30] A. Arnot, W. Meylan, J. Tunkel et al., "A quantitative structure-activity relationship for predicting metabolic biotransformation rates for organic chemicals in fish," *Environmental Toxicology and Chemistry*, vol. 28, no. 6, pp. 1168–1177, 2009.

[31] A. Arnot and F. A. P. C. Gobas, "A review of bioconcentration factor (BCF) and bioaccumulation factor (BAF) assessments for organic chemicals in fish," *Environmental Reviews*, vol. 14, no. 4, pp. 257–297, 2006.

[32] C. Cobelli, E. R. Carson, L. Finkelstein, and M. S. Leaning, "Validation of simple and complex models in physiology and medicine," *The American Journal of Physiology*, vol. 246, no. 2, pp. R259–266, 1984.

[33] R. Mannhold, G. I. Poda, C. Ostermann, and I. V. Tetko, "Calculation of molecular lipophilicity: state-of-the-art and

comparison of logP methods on more than 96,000 compounds," *Journal of Pharmaceutical Sciences*, vol. 98, no. 3, pp. 861–893, 2009.

[34] M. Yazdanian, S. L. Glynn, J. L. Wright, and A. Hawi, "Correlating partitioning and Caco-2 cell permeability of structurally diverse small molecular weight compounds," *Pharmaceutical Research*, vol. 15, no. 9, pp. 1490–1494, 1998.

[35] R. G. Jain, E. S. Furfine, L. Pedneault, A. J. White, and J. M. Lenhard, "Metabolic complications associated with antiretroviral therapy," *Antiviral Research*, vol. 51, no. 3, pp. 151–177, 2001.

[36] S. K. Gan, K. Samaras, A. Carr, and D. Chisholm, "Antiretroviral therapy, insulin resistance and lipodystrophy," *Diabetes, Obesity and Metabolism*, vol. 3, no. 2, pp. 67–71, 2001.

[37] M. J. Glesby, "Toxicities and adverse findings associated with protease inhibitors," in *Protease Inhibitors in AIDS Therapy*, R. C. Ogden and C. W. Flexner, Eds., pp. 237–256, Marcel Dekker, Inc., New York, NY, USA, 2001.

[38] P. A. Pham and C. Flexner, "Emerging antiretroviral drug interactions," *Journal of Antimicrobial Chemotherapy*, vol. 66, no. 2, pp. 235–239, 2011.

[39] D. Wang, B. Larder, A. Revell et al., "A comparison of three computational modelling methods for the prediction of virological response to combination HIV therapy," *Artificial Intelligence in Medicine*, vol. 47, no. 1, pp. 63–74, 2009.

[40] O. Krakovska and L. M. Wahl, "Optimal drug treatment regimens for HIV depend on adherence," *Journal of Theoretical Biology*, vol. 246, no. 3, pp. 499–509, 2007.

[41] S. Hongzong, Y. Shuping, Z. Kejun, F. Aiping, D. Yun-Bo, and H. Zhide, "Quantitative structure activity relationship study on EC50 of anti-HIV drugs," *Chemometrics and Intelligent Laboratory Systems*, vol. 90, no. 1, pp. 15–24, 2008.

[42] B. Testa, P. Crivori, M. Reist, and P. A. Carrupt, "The influence of lipophilicity on the pharmacokinetic behavior of drugs: concepts and examples," *Perspectives in Drug Discovery and Design*, vol. 19, pp. 179–211, 2000.

[43] J. W. Nichols, M. Bonnell, S. D. Dimitrov, B. I. Escher, X. Han, and N. I. Kramer, "Bioaccumulation assessment using predictive approaches," *Integrated Environmental Assessment and Management*, vol. 5, no. 4, pp. 577–597, 2009.

[44] C. A. Lipinski, F. Lombardo, B. W. Dominy, and P. J. Feeney, "Experimental and computational approaches to estimate solubility and permeability in drug discovery and development settings," *Advanced Drug Delivery Reviews*, vol. 23, no. 1–3, pp. 3–25, 1997.

[45] W. B. Neely, D. R. Branson, and G. E. Blau, "Partition coefficient to measure bioconcentration potential of organic chemicals in fish," *Environmental Science and Technology*, vol. 8, no. 13, pp. 1113–1115, 1974.

[46] S. Dimitrov, T. Pavlov, D. Nedelcheva et al., "A kinetic model for predicting biodegradation," *SAR and QSAR in Environmental Research*, vol. 18, no. 5-6, pp. 443–457, 2007.

[47] S. D. Dimitrov, N. C. Dimitrova, J. D. Walker, G. D. Veith, and O. G. Mekenyan, "Predicting BCFs of highly hydrophobic chemicals: effects of molecular size," *Pure and Applied Chemistry*, vol. 74, no. 10, pp. 1823–1830, 2002.

[48] P. Howard, W. Meylan, D. Aronson et al., "A new biodegradation prediction model specific to petroleum hydrocarbons," *Environmental Toxicology and Chemistry*, vol. 24, no. 8, pp. 1847–1860, 2005.

Hindawi Publishing Corporation
Computational and Mathematical Methods in Medicine
Volume 2012, Article ID 605861, 8 pages
doi:10.1155/2012/605861

Research Article

Mathematical Model of the Impact of a Nonantibiotic Treatment for *Clostridium difficile* on the Endemic Prevalence of Vancomycin-Resistant Enterococci in a Hospital Setting

Daniel T. Grima,[1] Glenn F. Webb,[2] and Erika M. C. D'Agata[3]

[1] *Cornerstone Research Group Inc., 204-3228 South Service Road, Burlington, ON, L7N 3H8, Canada L7N 3H8*
[2] *Mathematics Department, Vanderbilt University, Nashville, TN, 37240, USA*
[3] *Division of Infectious Disease, Beth Israel Deaconess Medical Center, Harvard Medical School, Lowry Building Suite 6A, 100 Francis Street, Boston, MA, 02215, USA*

Correspondence should be addressed to Daniel T. Grima, dgrima@cornerstone-research.com

Received 23 June 2011; Accepted 4 October 2011

Academic Editor: Philip Crooke

Introduction. *Clostridium difficile*-associated disease (CDAD) is treated using antibiotics, which often leads to the emergence of antibiotic-resistant bacteria such as vancomycin-resistant enterococci (VRE). This study estimated the impact of a non antibiotic treatment for CDAD on VRE prevalence. *Methods*. A previously published model describing the impact of in-hospital antibiotic use on VRE prevalence was adapted to include CDAD treatment. Simulations compared the prevalence of VRE when nonantibiotic versus antibiotic therapy was used. *Results*. Nonantibiotic treatment in 50% of CDAD patients resulted in an 18% relative reduction in the prevalence of VRE colonization compared with antibiotic use only. Sensitivity analysis found the model to be most sensitive to rates of antibiotic initiation and discontinuation, prevalence of VRE in admitted patients, length of stay of colonized patients, probability of CDAD acquisition, and hand-washing compliance. *Conclusion*. Nonantibiotic treatment of patients hospitalized with CDAD may significantly reduce the incidence of VRE colonization.

1. Introduction

The bacterium *Clostridium difficile* is the most common cause of hospital-acquired diarrhea, accounting for up to 25% of all cases of antibiotic-associated diarrhea [1, 2]. Rates of colonization of inpatients with *C. difficile* may be as high as 50% for patients hospitalized for more than four weeks [3]. The incidence of *C. difficile*-associated disease (CDAD) has been growing on the basis of data from the National Nosocomial Infections Surveillance system [3]. Importantly, outbreaks of severe CDAD cases have occurred in several hospitals because of the emergence of a new *C. difficile* strain with increased virulence and antibiotic resistance [4, 5]. This more virulent bacterial strain results in more admissions to the intensive care unit, colectomies, and death than other strains [4, 5]. A recent study reported that in the United States, the incidence of adult CDAD hospitalizations doubled from 5.5 cases per 10,000 population in 2000 to 11.2 per 10,000 cases in 2005, and the age-adjusted CDAD-related case-fatality rate rose from 1.2% in 2000 to 2.2% in 2004 [6].

Current treatment of CDAD involves antibiotic therapy with either metronidazole or vancomycin. However, there has been a growing interest in the development of nonantibiotic therapies for CDAD and other nosocomial infections in order to reduce antibiotic use in hospitals, where the goal is to limit the emergence and spread of antibiotic-resistant bacteria such as vancomycin-resistant enterococci (VRE) [7]. The use of such antibiotics can eradicate antibiotic-susceptible bacterial strains in the gastrointestinal flora, thereby allowing the overgrowth of subpopulations of antibiotic-resistant bacteria [8, 9]. In the case of *C. difficile* treatment, both metronidazole and vancomycin are associated with the promotion of VRE. This overgrowth is evidenced by the cocolonization of *C.*

difficile and VRE that occurs in 20% to 34% of patients, which may reflect *C. difficile*-directed antibiotic exposure as well as other common risk factors for these pathogens [10–12].

It has been suggested that nonantibiotic treatment of CDAD may offer an opportunity to reduce antibiotic use in hospitals and could ultimately decrease the prevalence and burden of VRE. For example, although ultimately unsuccessful, the enterotoxin-binding polymer tolevamer (Genzyme, Inc.) was investigated for the treatment of CDAD in 2008 [13, 14]. More recently, a number of small studies have reported on the successful use of fecal donor instillation therapy (FDIT) for the treatment of patients with CDAD [15–17]. Used for decades in some hospitals, only recently has the effectiveness of this therapy been documented in the literature. In a retrospective study of 40 patients with recurrent CDAD, 83% of patients were successfully treated with FDIT, having met the study's endpoint of no further hospital contact due to CDAD symptoms within 80 days of therapy. While in the study's protocol patients were treated with metronidazole or vancomycin until reduction of symptoms, all antimicrobial therapy was discontinued on the evening prior to donor stool transplantation [18].

The objective of this study was to estimate the potential impact of a nonantibiotic treatment for CDAD on the prevalence of VRE within a hospital setting. A mathematical model was used to estimate and compare the prevalence of VRE with current antibiotic therapies for CDAD versus nonantibiotic therapies such as FDIT.

2. Methods

The current model (Appendix) extends a previously published model by D'Agata and colleagues (2005) that described the impact of antibiotic use on VRE prevalence within a hospital setting [19]. The model considers the admission of patients with and without VRE to a hospital and their consequent risks of CDAD and VRE acquisition. Since VRE is predominantly spread from patient-to-patient via the contaminated hands or clothes of health care workers (HCWs), the complex interactions between patients and HCWs were also incorporated into the model. The model describes the transmission dynamics of VRE in a 400-bed hospital. The original model compartmentalized patients into those receiving (right side of Figure 1) and not receiving (left side of Figure 1) antibiotics, and those who were VRE-colonized (bottom boxes in Figure 1) and those who were not (top boxes in Figure 1). The original model was then extended to include CDAD status. Each of the four original boxes was divided into an outer and inner box, and CDAD positive (CDAD+) patients were included in the inner boxes 3, 4, 5, and 6. These boxes included CDAD patients who were not receiving antibiotics and were either uncolonized (Box 3) or colonized (Box 5) with VRE as well as individuals who were receiving antibiotics and were either uncolonized (Box 4) or colonized (Box 6) with VRE.

All model parameter values are provided in Table 1. Except where noted below, the same values from D'Agata and colleagues' model were used. These values were originally obtained from pharmacy records and an observational HCW study at Beth Israel Deaconess Medical Center [19]. The spread of VRE between patients and associated movement between compartments occurred because of HCWs whose hands were contaminated with VRE after contact with a colonized patient (Figure 2). The interaction between patients and HCWs included the number of contacts with a patient during routine patient care and compliance with hand hygiene (Table 1). The latter was an important inclusion, since hand hygiene will remove VRE from HCWs' hands and thereby prevent transmission of VRE to patients. It was assumed that patients who were colonized with VRE were on contact precautions and therefore less likely to contaminate HCWs. The implementation of these precautions is standard practice in hospital settings and requires HCWs to don gloves and gowns prior to entering the room of a VRE-colonized patient in order to prevent HCW contamination [20].

The movement between compartments was also influenced by the proportion of patients who were started on antibiotics or in whom antibiotics were discontinued. It was assumed that patients receiving antibiotics were more likely to contaminate an HCW, since studies have documented that antibiotic exposure results in increased VRE stool densities and a greater likelihood of skin contamination (Table 1) [9]. Although contamination of HCWs' clothes and inanimate surfaces contribute to VRE dissemination, these factors were omitted in order to simplify the model [21].

The probability of colonization per contact between uncolonized CDAD patients on antibiotics and contaminated HCW (0.16) was based on an assumption that contact precautions for CDAD+ patients would decrease the probability of contamination by 60% compared to patients without CDAD [22]. These values were obtained from studies focusing on *Acinetobacter* spp. The daily probability of patients on antibiotics to transit to CDAD+ (15/14 = 1.07%) was based on an overall risk of CDAD infection for antibiotic-treated patients of 15% and an average length of stay of 14 days, as per the original model [19]. The daily probability of CDAD resolution of 27.03% = 100 ($3 \times 9 + 10 \times 0.1$) was based on the assumption that 90% of CDAD cases resolve within 3 days and 10% require 10 days [23].

The model was run until it reached a steady state, and the total numbers of patients in each state was compared in two scenarios: (1) all patients received antibiotics for treatment of CDAD in hospital and (2) a subgroup of CDAD patients received a nonantibiotic treatment for CDAD with equal efficacy to antibiotic therapy. First, to simulate current care for CDAD with antibiotic therapy and the lack of a nonantibiotic treatment option, the transition probabilities for entry into boxes 3 and 5 were set to zero. Second, to simulate the impact of avoiding antibiotic exposure with the use of a nonantibiotic therapy for CDAD, 50% of patients acquiring CDAD were assumed to discontinue antibiotics and move to boxes 3 and 5.

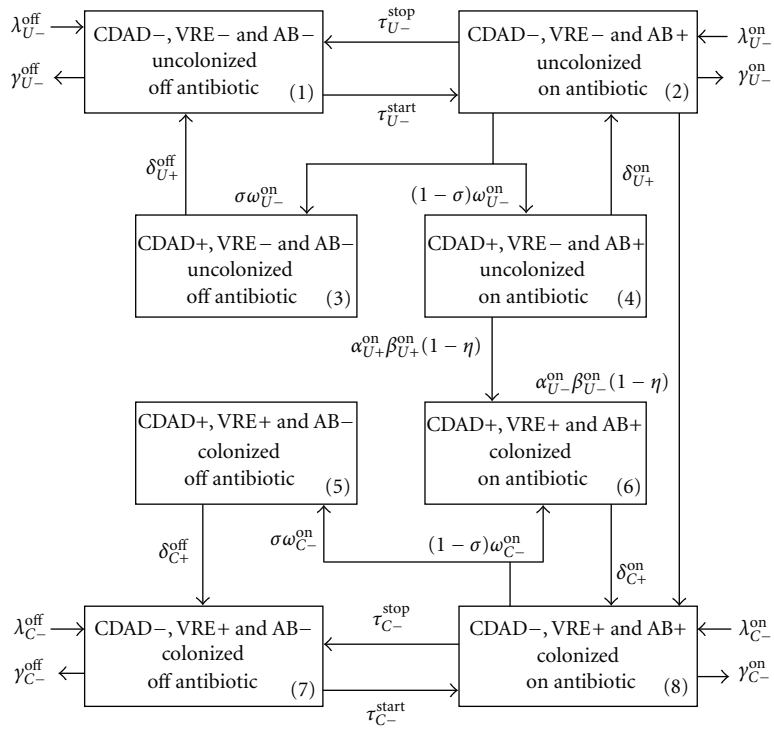

Figure 1: Schematic diagram of the patient compartments. CDAD = *clostridium difficile*-associated disease; CDAD+ = *clostridium difficile*-associated disease positive; CDAD− = *clostridium difficile*-associated disease negative; VRE = vancomycin-resistant enterococci; VRE+ = vancomycin-resistant enterococci colonized; VRE− = vancomycin-resistant enterococci not colonized; AB− = off antibiotics; AB+ = on antibiotics; λ_{U-}^{off} = CDAD−, uncolonized, off antibiotic: admission rate; γ_{U-}^{off} = CDAD−, uncolonized, off antibiotic: average length of stay; λ_{U-}^{on} = CDAD−, uncolonized, on antibiotic: admission rate; γ_{U-}^{on} = CDAD−, uncolonized, on antibiotic: average length of stay; τ_{U-}^{stop} = CDAD−, uncolonized, on antibiotic: stop antibiotic; τ_{U-}^{start} = CDAD−, uncolonized, off antibiotic: start antibiotic; δ_{U+}^{off} = CDAD+, uncolonized, off antibiotic: transit to CDAD−; σ = fraction of AB patients that transit to CDAD+ and stop AB; ω_{U-}^{on} = CDAD−, uncolonized, on antibiotic: transit to CDAD+; δ_{U+}^{on} = CDAD+, uncolonized, on antibiotic: transit to CDAD−; α_{U+}^{on} = average number of contacts between uncolonized CDAD− patients on antibiotic and HCW; β_{U+}^{on} = probability of colonization per contact between uncolonized CDAD+ patient on antibiotic and contaminated HCW; α_{U-}^{on} = average number of contacts between uncolonized CDAD+ patients on antibiotic and HCW; β_{U-}^{on} = probability of colonization per contact between uncolonized CDAD− patient on antibiotic and contaminated HCW; η = hand washing compliance factor between 0 and 1; δ_{C+}^{off} = CDAD+, colonized, off antibiotic: transit to CDAD−; ω_{C-}^{on} = CDAD−, colonized, on antibiotic: transit to CDAD+; δ_{C+}^{on} = CDAD+, colonized, on antibiotic: transit to CDAD−; λ_{C-}^{off} = CDAD−, colonized, off antibiotic: admission rate; τ_{C-}^{stop} = CDAD−, colonized, on antibiotic: stop antibiotic; λ_{C-}^{on} = CDAD−, colonized, on antibiotic: admission rate; τ_{C-}^{start} = CDAD−, colonized, off antibiotic: start antibiotic; γ_{C-}^{on} = CDAD−, colonized, on antibiotic: average length of stay; γ_{C-}^{off} = CDAD−, colonized, off antibiotic: average length of stay.

3. Sensitivity Analyses

Univariate sensitivity analyses were conducted for percent of CDAD+ patients that stop antibiotics and start a nonantibiotic treatment, number of colonized patients admitted per day, length of stay of colonized patients, percentage of handwashing compliance, percentage of uncolonized patients on antibiotics that become CDAD+, and time to symptoms resolution of colonized CDAD+ patients on antibiotics.

4. Results

The distributions of patients in each steady state under both scenarios are summarized in Table 2. Under the first scenario, where antibiotics were used for all CDAD+ patients (σ = 0.0), of the approximately 400 patients in the steady state, 60 (15.0%) were colonized with VRE, 194 (48.5%) were on antibiotics, and 6 (1.5%) were CDAD+, all of whom were on antibiotics (Table 2). Under the second scenario, where 50% of CDAD+ patients discontinued antibiotics in favor of a nonantibiotic treatment (σ = 0.5), VRE colonization was reduced. In this scenario, the total number of patients on antibiotics declined to 185 (46.3%) and the number of CDAD+ patients receiving antibiotics declined to 3 (0.75%). The total number of patients who were VRE-colonized at any given time declined from 60 to 49 (from 15.0% down to 12.25%), an absolute decline of 2.75% and a relative decline of 18%. Assuming a 400-bed hospital and 25 patients per bed a year, this outcome translates into 275 avoided cases of VRE colonization per year.

Results of the sensitivity analyses are presented in Figure 2. In all analyses, the nonantibiotic use scenario was associated with a lower prevalence of VRE colonization. In the nonantibiotic scenario, the percentage of VRE-colonized

Table 1: Parameters used in modeling the effect of antibiotic versus nonantibiotic treatment of CDAD on VRE colonization.

Parameter	Patients	Value
Np	number of patients in the hospital	400
ρ	ratio of patients to HCW	4
$\lambda_{U-}^{\text{off}}$	CDAD−, uncolonized, off antibiotic: admission rate	50.1 per day
γ_{U-}^{off}	CDAD−, uncolonized, off antibiotic: average length of stay	5 days
λ_{U-}^{on}	CDAD−, uncolonized, on antibiotic: admission rate	2.505 per day
γ_{U-}^{on}	CDAD−, uncolonized, on antibiotic: average length of stay	14 days
$\lambda_{C-}^{\text{off}}$	CDAD−, colonized, off antibiotic: admission rate	0.334 per day
γ_{C-}^{off}	CDAD−, colonized, off antibiotic: average length of stay	28 days
λ_{C-}^{on}	CDAD−, colonized, on antibiotic: admission rate	0.501 per day
γ_{C-}^{on}	CDAD−, colonized, on antibiotic: average length of stay	28 days
τ_{U-}^{stop}	CDAD−, uncolonized, on antibiotic: stop antibiotic	15% per day
τ_{U-}^{start}	CDAD−, uncolonized, off antibiotic: start antibiotic	15% per day
τ_{C-}^{stop}	CDAD−, colonized, on antibiotic: stop antibiotic	4% per day
τ_{C-}^{start}	CDAD−, colonized, off antibiotic: start antibiotic	16% per day
σ	fraction of CDAD+, on antibiotic: stop antibiotic	0.5
α_{U+}^{on}	average number of contacts between uncolonized CDAD− patients on antibiotic and HCW	8 per day
α_{U-}^{on}	average number of contacts between uncolonized CDAD+ patients on antibiotic and HCW	8 per day
β_{U+}^{on}	probability of colonization per contact between uncolonized CDAD+ patient on antibiotic and contaminated HCW	0.024
β_{U-}^{on}	probability of colonization per contact between uncolonized CDAD− patient on antibiotic and contaminated HCW	0.06
ω_{U-}^{on}	CDAD−, uncolonized, on antibiotic: transit to CDAD+	1.07% per day
ω_{C-}^{on}	CDAD−, colonized, on antibiotic: transit to CDAD+	1.07% per day
δ_{C+}^{on}	CDAD+, colonized, on antibiotic: transit to CDAD−	27% per day
δ_{C+}^{off}	CDAD+, colonized, off antibiotic: transit to CDAD−	27% per day
δ_{U+}^{on}	CDAD+, uncolonized, on antibiotic: transit to CDAD−	27% per day
δ_{U+}^{off}	CDAD+, uncolonized, off antibiotic: transit to CDAD−	27% per day
σ	fraction of AB patients that transit to CDAD+ and stop AB	0.0 or 0.5
Parameter	Health care workers	Value
α_{C+}	average number of contacts between HCW and colonized CDAD+ patients	10 per day
α_{C-}	average number of contacts between HCW and colonized CDAD+ patients	10 per day
κ_{-}^{on}	probability of contamination per contact between uncontaminated HCW and colonized CDAD− patient on antibiotic	0.4
κ_{-}^{off}	probability of contamination per contact between uncontaminated HCW and colonized CDAD− patient off antibiotic	0.4
κ_{+}^{on}	probability of contamination per contact between uncontaminated HCW and colonized CDAD+ patient on antibiotic	0.16
κ_{+}^{off}	probability of contamination per contact between uncontaminated HCW and colonized CDAD+ patient off antibiotic	0.16
μ	average duration of HCW contamination	48 minutes
η	hand-washing compliance factor between 0 and 1	0.6

CDAD = *clostridium difficile*-associated disease; VRE = vancomycin-resistant enterococci; HCW = health care worker; CDAD+ = *clostridium difficile*-associated disease positive; CDAD− = *clostridium difficile*-associated disease negative; AB = antibiotics.

patients decreased notably if the percentage of CDAD+ patients that stop antibiotics and start a nonantibiotic regiment increased (Figure 2(a)), the hand-washing compliance percentage increased (Figure 2(d)), or the percentage of uncolonized patients on antibiotics that become CDAD+ increased (Figure 2(e)). With both antibiotic and nonantibiotic therapies, the percentage of VRE-colonized patients increased notably when the number of colonized patients admitted per day increased (Figure 2(b)) or the length of stay of colonized patients increased (Figure 2(c)).

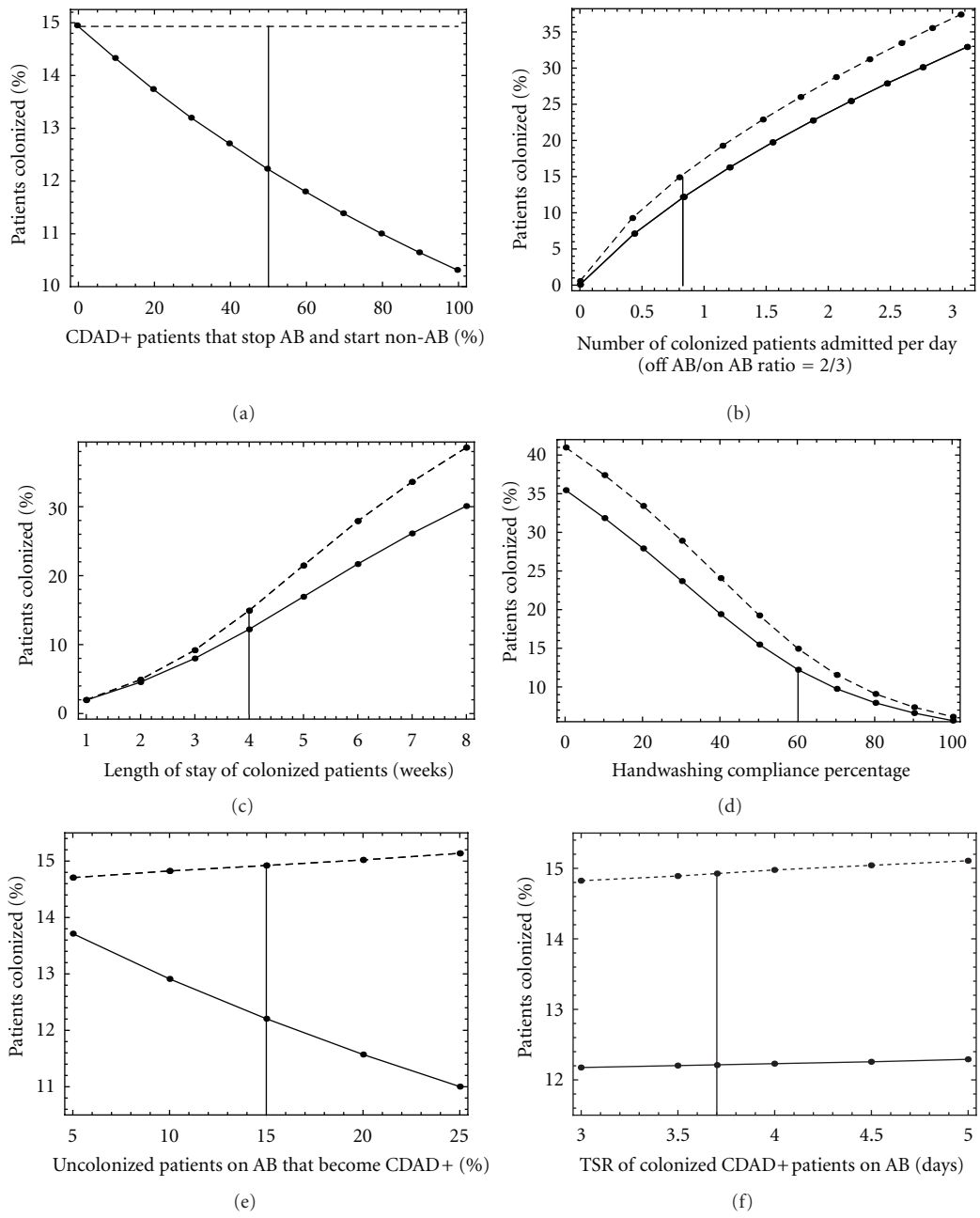

Figure 2: Sensitivity analyses of the model parameters. Dashed lines: Scenario 1 (use of AB only); Solid lines: Scenario 2 (use of non-antimicrobial); Vertical line: baseline values; (a) Percentage of CDAD+ patients that stop AB and start non-AB (baseline = 50%, $\sigma = 0.5$); (b) Number of colonized patients admitted per day in the ratio $\lambda_{C-}^{\text{off}}/\lambda_{C-}^{\text{on}} = 2/3$ (baseline $\lambda_{C-}^{\text{off}} = 0.33$, $\lambda_{C-}^{\text{on}} = 0.5$); (c) Length of stay of colonized patients in weeks (baseline = 4 weeks, $= \gamma_{C-}^{\text{off}}/\gamma_{C-}^{\text{on}} = 1/28$); (d) Hand-washing compliance percentage (baseline = 60%, $\eta = 0.6$); (e) Percentage of uncolonized and colonized patients on AB (held equal) that become CDAD+ (baseline = 15%, $\omega_{U-}^{\text{on}} = \omega_{C-}^{\text{on}} = -\log(0.9893)$); (f) Time to symptoms resolution (TSR) of colonized CDAD+ patients on AB in days (baseline = 3.7 days, $\delta_{C+}^{\text{on}} = -\log(0.73)$); AB = antibiotic; CDAD = *clostridium difficile*-associated disease; non-AB = nonantibiotic; $\lambda_{C-}^{\text{off}}$ = CDAD−, colonized, off antibiotic: admission rate; γ_{C-}^{on} = CDAD−, colonized, on antibiotic: average length of stay; ω_{U-}^{on} = CDAD−, uncolonized, on antibiotic: transit to CDAD+; ω_{C-}^{on} = CDAD−, colonized, on antibiotic: transit to CDAD+; γ_{C-}^{off} = CDAD−, colonized, off antibiotic: average length of stay; λ_{C-}^{on} = CDAD−, colonized, on antibiotic: admission rate.

5. Discussion

The association between antibiotic use in hospitals and the colonization of patients with antibiotic-resistant bacteria such as VRE is well documented [24]. This finding has spurred research into nonantibiotic options for the treatment of nosocomial infections such as CDAD. For example, the anionic polymer tolevamer (Genzyme, Inc.) was developed

Table 2: Distribution of patients and health care workers with or without VRE colonization on the basis of antibiotic versus nonantibiotic treatment of CDAD.

Patient colonization/HCW contamination status	AB status	Model with AB only	Model with AB and non-AB	Change with non-AB	Difference with non-AB
Patient Steady State Values					
uncolonized CDAD− patient	off	195.176	202.555	increases	7.390
uncolonized CDAD− patient	on	140.383	143.553	increases	3.170
colonized CDAD− patient	off	10.7197	9.0598	decreases	−1.6599
colonized CDAD− patient	on	47.3343	38.4389	decreases	−8.8954
uncolonized CDAD+ patient	on	4.7467	2.4307	decreases	−2.3160
colonized CDAD+ patient	on	1.6721	0.6798	decreases	−0.9923
uncolonized CDAD+ patient	off	0.0	2.4535	increases	2.4535
colonized CDAD+ patient	off	0.0	0.6570	increases	0.6570
Patient Totals at Steady State					
total patients		400.03	399.828		
Total VRE-colonized patients		59.7361	48.83555	decreases	−10.8905
total CDAD+ patients		6.4188	6.2210	decreases	−0.1978
total CDAD+ patients on AB		6.4188	3.1105	decreases	−3.3083
total patients on AB		194.136	185.102	decreases	−9.034
Percentage of Patients Colonized at Steady State					
% of all patients colonized		14.930%	12.214%	decreases	−2.716%
% CDAD− patients colonized		14.749%	12.068%	increases	−2.681%
% CDAD+ patients colonized		26.050%	21.488%	decreases	−4.562%
HCW Steady State Values					
uncontaminated HCW		95.3347	96.1513	increases	0.8166
contaminated HCW		4.6653	3.8487	decreases	−0.8166

CDAD = *Clostridium difficile*-associated disease; VRE = vancomycin-resistant enterococci; HCW = health care worker; CDAD+ = *Clostridium difficile*-associated disease positive; CDAD− = *clostridium difficile*-associated disease negative; AB = antibiotic.

to neutralize clostridial toxins without adversely affecting the normal flora of the gut [13, 14]. Results from a phase III trial revealed that the recurrence rate of CDAD was reduced significantly when compared with vancomycin and metronidazole; however, the study failed to meet its primary endpoint due to the high dropout rate associated with tolevamer [25]. As the development of the therapy was subsequently halted, its impact on the prevalence of VRE is unknown.

More recent publications have reported on the safety and effectiveness of FDIT for the treatment of CDAD. This therapy involves the introduction of a stool transplant into the duodenum or colon via a gastroscope or colonoscope, respectively, to repopulate the microflora of the bowel [15, 16]. Although used for decades, particularly in Scandinavian countries, the clinical data describing FDIT are limited; still, available reports suggest that the treatment is safe and effective even in patients with refractory CDAD [15–17]. A recent review of 16 publications concluded that 91% of all reported patients with recurrent *C. difficile* infection who were treated with FDIT were cured after one or more infusions [26]. The impact of FDIT on the prevalence of VRE, however, remains uncertain.

The availability of a nonantibiotic treatment for CDAD raises interesting questions regarding its possible impact on the prevalence of VRE compared with conventional antibiotic therapy. Our study adapted an existing model of VRE prevalence within a hospital setting to study the possible effect of the introduction of a nonantibiotic treatment for CDAD. The study found that treatment of 50% of patients with CDAD with a nonantibiotic regimen resulted in an approximately 2.75% absolute reduction (18% relative reduction) in VRE-colonized patients compared with a scenario, whereby all CDAD patients received antibiotics.

This reduction in VRE prevalence represents a meaningful impact within a hospital, given the costs associated with the management of VRE-colonized patients and potential clinical impact of VRE infections. For a 400-bed hospital, the analysis estimated a reduction of 275 cases of VRE colonization. On the basis of an average cost of contact precautions of USD $2,694.01 (CDN $3,191.83 at exchange of 0.844034), this would result in cost savings of approximately USD $740,800 a year [27]. A small reduction in VRE prevalence may also have a substantial impact on the clinical outcome and costs of VRE infections. VRE infection has been observed to occur in as many as 11.1% of VRE-colonized patients [12]. The cost to treat a patient with a VRE infection has been reported as approximately USD $13,000 [28]. The mortality rate for a VRE infection has been estimated as 39% to 49% [29]. On the basis of the current model, an 18% reduction in VRE prevalence could avert as many as 30.5 cases of VRE

infection for a 400-bed hospital. This reduction in VRE infections could lead to a cost savings of USD $396,500 per year and could prevent up to 15 VRE-associated deaths annually.

Note that the current study excludes other types of antibiotic-resistant bacteria such as methicillin-resistant *Staphylococcus aureus*, which would also be affected by reduced use of antibiotics within a hospital. As such, it is likely that the study underestimates the extent of the impact of a nonantibiotic treatment for CDAD.

The study shares limitations that are common to all mathematical models in that it requires the use of data from multiple sources to model processes that have not been fully observed. The validity of such a model comes from the use of realistic assumptions and clinical review. In this case, the study was derived from a published model that was based on patterns of VRE transmission that have been widely studied and baseline parameters that were obtained from actual hospital data [19]. Given the variability that may exist for some of the model parameters, extensive sensitivity analyses were conducted. These sensitivity analyses revealed that the following variables had the most influence on the prevalence of VRE: the rate of antibiotic initiation or discontinuation in CDAD negative and positive patients, the length of stay of VRE-colonized patients, hand-washing compliance, and the number of VRE-colonized patients admitted per day. All of these variables would be expected to differ among hospitals given local infection control policies and the endemic rates of VRE colonization in the community.

6. Conclusions

Use of a nonantibiotic treatment in hospital patients with CDAD may significantly reduce the colonization of patients with VRE and the associated burden of disease.

Appendix

The CDAD epidemic within the hospital setting is described mathematically by a system of nonlinear ordinary differential equations. The populations under consideration are as follows: uncolonized CDAD− patients off antibiotics (P^{off}_{U-}), uncolonized CDAD− patients on antibiotics (P^{on}_{U-}), colonized CDAD− patients off antibiotics (P^{off}_{C-}), colonized CDAD− patients on antibiotics (P^{on}_{C-}), uncolonized CDAD$^+$ patients off antibiotics (P^{off}_{U+}), uncolonized CDAD$^+$ patients on antibiotics (P^{on}_{U+}), colonized CDAD$^+$ patients off antibiotics (P^{off}_{C+}), colonized CDAD$^+$ patients on antibiotics (P^{on}_{C+}), uncontaminated health care workers (H_U), and contaminated health care workers (H_C). Each population is a function of time (t) in days, and each population has initial conditions prescribed at time 0. The rates of change of these populations are governed by

$$
\begin{aligned}
\frac{dP^{\text{off}}_{U-}}{dt} &= \lambda^{\text{off}}_{U-} - \tau^{\text{start}}_{U-}P^{\text{off}}_{U-} + \tau^{\text{stop}}_{U-}P^{\text{on}}_{U-} - \gamma^{\text{off}}_{U-}P^{\text{off}}_{U-} + \delta^{\text{off}}_{U+}P^{\text{off}}_{U+},\\
\frac{dP^{\text{on}}_{U-}}{dt} &= \lambda^{\text{on}}_{U-} - \tau^{\text{stop}}_{U-}P^{\text{on}}_{U-} + \tau^{\text{start}}_{U-}P^{\text{off}}_{U-} - \omega^{\text{on}}_{U-}P^{\text{on}}_{U-}\\
&\quad - \alpha^{\text{on}}_{U-}\beta^{\text{on}}_{U-}(1-\eta)\frac{H_C}{Nh}P^{\text{on}}_{U-} + \delta^{\text{on}}_{U+}P^{\text{on}}_{U+} - \gamma^{\text{on}}_{U-}P^{\text{on}}_{U-},\\
\frac{dP^{\text{off}}_{U+}}{dt} &= \sigma\omega^{\text{on}}_{U-}P^{\text{on}}_{U-} - \delta^{\text{off}}_{U+}P^{\text{off}}_{U+},\\
\frac{dP^{\text{on}}_{U+}}{dt} &= (1-\sigma)\omega^{\text{on}}_{U-}P^{\text{on}}_{U-} - \delta^{\text{on}}_{U+}P^{\text{on}}_{U+}\\
&\quad - \alpha^{\text{on}}_{U+}\beta^{\text{on}}_{U+}(1-\eta)\frac{H_C}{Nh}P^{\text{on}}_{U+},\\
\frac{dP^{\text{off}}_{C+}}{dt} &= \sigma\omega^{\text{on}}_{C-}P^{\text{on}}_{C-} - \delta^{\text{off}}_{C+}P^{\text{off}}_{C+},\\
\frac{dP^{\text{on}}_{C+}}{dt} &= (1-\sigma)\omega^{\text{on}}_{C-}P^{\text{on}}_{C-} - \delta^{\text{on}}_{C+}P^{\text{on}}_{C+}\\
&\quad + \alpha^{\text{on}}_{U+}\beta^{\text{on}}_{U+}(1-\eta)\frac{H_C}{Nh}P^{\text{on}}_{U+},\\
\frac{dP^{\text{off}}_{C-}}{dt} &= \lambda^{\text{off}}_{C-} - \tau^{\text{start}}_{C-}P^{\text{off}}_{C-} + \tau^{\text{stop}}_{C-}P^{\text{on}}_{C-}\\
&\quad - \gamma^{\text{off}}_{C-}P^{\text{off}}_{C-} + \delta^{\text{off}}_{C+}P^{\text{off}}_{C+},\\
\frac{dP^{\text{on}}_{C-}}{dt} &= \lambda^{\text{on}}_{C-} - \tau^{\text{stop}}_{C-}P^{\text{on}}_{C-} + \tau^{\text{start}}_{C-}P^{\text{off}}_{C-} - \omega^{\text{on}}_{C-}P^{\text{on}}_{C-}\\
&\quad + \alpha^{\text{on}}_{U-}\beta^{\text{on}}_{U-}(1-\eta)\frac{H_C}{Nh}P^{\text{on}}_{U-} + \delta^{\text{on}}_{C+}P^{\text{on}}_{C+} - \gamma^{\text{on}}_{C-}P^{\text{on}}_{C-},\\
\frac{dH_U}{dt} &= -\left[\alpha_{C-}\kappa^{\text{off}}_{-}\left(\frac{P^{\text{off}}_{C-}}{Np}\right) + \alpha_{C-}\kappa^{\text{on}}_{-}\left(\frac{P^{\text{on}}_{C-}}{Np}\right)\right.\\
&\quad \left. + \alpha_{C+}\kappa^{\text{on}}_{+}\left(\frac{P^{\text{on}}_{C+}}{Np}\right) + \alpha_{C+}\kappa^{\text{off}}_{+}\left(\frac{P^{\text{off}}_{C+}}{Np}\right)\right]\\
&\quad \times \rho H_U + \mu H_C,\\
\frac{dH_C}{dt} &= \left[\alpha_{C-}\kappa^{\text{off}}_{-}\left(\frac{P^{\text{off}}_{C-}}{Np}\right) + \alpha_{C-}\kappa^{\text{on}}_{-}\left(\frac{P^{\text{on}}_{C-}}{Np}\right)\right.\\
&\quad \left. + \alpha_{C+}\kappa^{\text{on}}_{+}\left(\frac{P^{\text{on}}_{C+}}{Np}\right) + \alpha_{C+}\kappa^{\text{off}}_{+}\left(\frac{P^{\text{off}}_{C+}}{Np}\right)\right]\\
&\quad \times \rho H_U - \mu H_C.
\end{aligned}
\tag{A.1}
$$

Conflict of Interests

D. T. Grima and E. M. C. D'Agata have been consultants for and received research funding from Genzyme Corporation.

Funding

This work is financially supported by Genzyme Corporation.

Acknowledgment

The authors would like to acknowledge the contributions of Parisa Airia during the preparation of the paper.

References

[1] F. Barbut, G. Corthier, Y. Charpak et al., "Prevalence and pathogenicity of *Clostridium difficile* in hospitalized patients: a French multicenter study," *Archives of Internal Medicine*, vol. 156, no. 13, pp. 1449–1454, 1996.

[2] J. G. Bartlett, "*Clostridium difficile*: history of its role as an enteric pathogen and the current state of knowledge about the

organism," *Clinical Infectious Diseases*, vol. 18, supplement 4, pp. S265–S272, 1994.

[3] L. K. Archibald, S. N. Banerjee, and W. R. Jarvis, "Secular trends in hospital-acquired *Clostridium difficile* disease in the United States, 1987–2001," *Journal of Infectious Diseases*, vol. 189, no. 9, pp. 1585–1589, 2004.

[4] V. G. Loo, L. Poirier, M. A. Miller et al., "A predominantly clonal multi-institutional outbreak of *Clostridium difficile*—associated diarrhea with high morbidity and mortality," *The New England Journal of Medicine*, vol. 353, no. 23, pp. 2442–2449, 2005.

[5] L. C. McDonald, G. E. Killgore, A. Thompson et al., "An epidemic, toxin gene-variant strain of *Clostridium difficile*," *The New England Journal of Medicine*, vol. 353, no. 23, pp. 2433–2441, 2005.

[6] M. D. Zilberberg, A. F. Shorr, and M. H. Kollef, "Increase in adult *Clostridium difficile*-related hospitalizations and case-fatality rate, United States, 2000–2005," *Emerging Infectious Diseases*, vol. 14, no. 6, pp. 929–931, 2008.

[7] W. N. Al-Nassir, A. K. Sethi, Y. Li, M. J. Pultz, M. M. Riggs, and C. J. Donskey, "Both oral metronidazole and oral vancomycin promote persistent overgrowth of vancomycin-resistant enterococci during treatment of *Clostridium difficile*-associated disease," *Antimicrobial Agents and Chemotherapy*, vol. 52, no. 7, pp. 2403–2406, 2008.

[8] E. J. Vollaard and H. A. L. Clasener, "Colonization resistance," *Antimicrobial Agents and Chemotherapy*, vol. 38, no. 3, pp. 409–414, 1994.

[9] E. M. C. D'Agata, S. Gautam, W. K. Green, and Y. W. Tang, "High rate of false-negative results of the rectal swab culture method in detection of gastrointestinal colonization with vancomycin-resistant enterococci," *Clinical Infectious Diseases*, vol. 34, no. 2, pp. 167–172, 2002.

[10] R. D. Poduval, R. P. Kamath, M. Corpuz, E. P. Norkus, and C. S. Pitchumoni, "*Clostridium difficile* and vancomycin-resistant *Enterococcus*: the new nosocomial alliance," *The American Journal of Gastroenterology*, vol. 95, no. 12, pp. 3513–3515, 2000.

[11] C. J. Donskey, A. J. Ray, C. K. Hoyen et al., "Colonization and infection with multiple nosocomial pathogens among patients colonized with vancomycin-resistant *Enterococcus*," *Infection Control and Hospital Epidemiology*, vol. 24, no. 4, pp. 242–245, 2003.

[12] A. L. Leber, J. F. Hindler, E. O. Kato, D. A. Bruckner, and D. A. Pegues, "Laboratory-based surveillance for vancomycin-resistant enterococci: utility of screening stool specimens submitted for *Clostridium difficile* toxin assay," *Infection Control and Hospital Epidemiology*, vol. 22, no. 3, pp. 160–164, 2001.

[13] N. Scheinfeld and K. Biggers, "Tolevamer, an orally administered, toxin-binding polymer for *Clostridium difficile*-associated diarrhea," *Current Opinion in Investigational Drugs*, vol. 9, no. 8, pp. 913–924, 2008.

[14] P. L. Hinkson, C. Dinardo, D. DeCiero, J. D. Klinger, and R. H. Barker, "Tolevamer, an anionic polymer, neutralizes toxins produced by the BI/027 strains of *Clostridium difficile*," *Antimicrobial Agents and Chemotherapy*, vol. 52, no. 6, pp. 2190–2195, 2008.

[15] K. Garborg, B. Waagsbø, A. Stallemo, J. Matre, and A. Sundøy, "Results of faecal donor instillation therapy for recurrent *Clostridium difficile*-associated diarrhoea," *Scandinavian Journal of Infectious Diseases*, vol. 42, no. 11-12, pp. 857–861, 2010.

[16] S. S. Yoon and L. J. Brandt, "Treatment of refractory/recurrent C. difficile-associated disease by donated stool transplanted via colonoscopy: a case series of 12 patients," *Journal of Clinical Gastroenterology*, vol. 44, no. 8, pp. 562–566, 2010.

[17] A. A. MacConnachie, R. Fox, D. R. Kennedy, and R. A. Seaton, "Faecal transplant for recurrent *Clostridium difficile*-associated diarrhoea: a UK case series," *QJMed*, vol. 102, no. 11, pp. 781–784, 2009.

[18] "A overview of the current status of FDIT," *Scientific American, November 2011*, http://www.scientificamerican.com/article.cfm?id=swapping-erms&page=3#comments.

[19] E. M. C. D'Agata, G. Webb, and M. Horn, "A mathematical model quantifying the impact of antibiotic exposure and other interventions on the endemic prevalence of vancomycin-resistant enterococci," *Journal of Infectious Diseases*, vol. 192, no. 11, pp. 2004–2011, 2005.

[20] C. A. Muto, J. A. Jernigan, B. E. Ostrowsky et al., "SHEA guideline for preventing nosocomial transmission of multidrug-resistant strains of *Staphylococcus aureus* and *Enterococcus*," *Infection Control and Hospital Epidemiology*, vol. 24, no. 9, pp. 362–386, 2003.

[21] E. S. McBryde and D. L. S. McElwain, "A mathematical model investigating the impact of an environmental reservoir on the prevalence and control of vancomycin-resistant enterococci," *Journal of Infectious Diseases*, vol. 193, no. 10, pp. 1473–1474, 2006.

[22] H. Gbaguidi-Haore, S. Legast, M. Thouverez, X. Bertrand, and D. Talon, "Ecological study of the effectiveness of isolation precautions in the management of hospitalized patients colonized or infected with *Acinetobacter baumannii*," *Infection Control and Hospital Epidemiology*, vol. 29, no. 12, pp. 1118–1123, 2008.

[23] W. N. Al-Nassir, A. K. Sethi, M. M. Nerandzic, G. S. Bobulsky, R. L. P. Jump, and C. J. Donskey, "Comparison of clinical and microbiological response to treatment of *Clostridium difficile*-associated disease with metronidazole and vancomycin," *Clinical Infectious Diseases*, vol. 47, no. 1, pp. 56–62, 2008.

[24] D. N. Gerding, "Is there a relationship between vancomycin-resistant enterococcal infection and *Clostridium difficile* infection?" *Clinical Infectious Diseases*, vol. 25, supplement, pp. S206–S210, 1997.

[25] A study to assess the safety, tolerability, effectiveness and absorption of Exodif tablets in *Clostridium difficile*-associated diarrhea. Trial identifier: NCT00466635, 2011, http://www.clinicaltrials.gov/.

[26] E. van Nood, P. Speelman, E. J. Kuijper, and J. J. Keller, "Struggling with recurrent *Clostridium difficile* infections: is donor faeces the solution?" *Euro Surveillance*, vol. 14, no. 34, Article ID 19316, 2009.

[27] L. O. Conterno, J. Shymanski, K. Ramotar, B. Toye, R. Zvonar, and V. Roth, "Impact and cost of infection control measures to reduce nosocomial transmission of extended-spectrum β-lactamase-producing organisms in a non-outbreak setting," *Journal of Hospital Infection*, vol. 65, no. 4, pp. 354–360, 2007.

[28] Y. Carmeli, G. Eliopoulos, E. Mozaffari, and M. Samore, "Health and economic outcomes of vancomycin-resistant enterococci," *Archives of Internal Medicine*, vol. 162, no. 19, pp. 2223–2228, 2002.

[29] C. D. Salgado and B. M. Farr, "Outcomes associated with vancomycin-resistant enterococci: a meta-analysis," *Infection Control and Hospital Epidemiology*, vol. 24, no. 9, pp. 690–698, 2003.